11-3-2016 12:00 AM

The geometry and density of B-emission star disks from statistical analysis and numerical simulations

Isabelle H. Cyr, *The University of Western Ontario*

Supervisor: Dr. Carol E. Jones, *The University of Western Ontario*

A thesis submitted in partial fulfillment of the requirements for the Doctor of Philosophy degree in Astronomy

Thesis advisor: Professor Carol E. Jones Isabelle H. Cyr

Abstract

This thesis is divided into 3 investigations. First we present a novel method to estimate the opening angles of Be star disks from interferometric axis ratio measurements, using Bayesian statistics and Monte Carlo techniques. A large set of theoretical axis ratios generated from disk models were compared to observational samples to determine which distribution best reproduces the observations. We find that the observed axis ratio distributions in the K-, H-, and N-band can best be explained by the presence of thin disks while measurements over the Hα line point toward slightly thicker disks.

Second, using a smoothed particle hydrodynamics (SPH) code, we studied the density structure of Be star disks in binary systems for a range of misalignment angles and disk viscosity. The truncation, warping, and density structure in the inner and outer parts of the disk are investigated. We find that these parameters affect both the truncation radius and the density of the outer disc, while the inner disk remains mostly unaffected. The scale height of our disks are also compared to analytical values. We find that the analytic values reproduces the scale height fairly well but underestimates the scale height in regions where density enhancements develop.

Finally the shape and density structure of these enhancements were also investigated. We find that larger misalignment angles and viscosity values result in more tightly wound spiral arms with shallower density profiles. The orbital phase was shown to have very little effect on the structure of the spiral density enhancements.

Keywords: Astrophysics, Be star, circumstellar disk, hydrodynamics, density structure, axis ratio, binary

The following authors contributed to Chapter 2: I. H. Cyr, C. E. Jones, C. Tycner.

The premise of using Bayesian statistics and Monte Carlo techniques to deproject axis ratios obtained from interferometric measurements found in the literature was put forward by CEJ. IHC acquired the axis ratio data from the literature, developed the disk models and statistical procedures, wrote and ran the simulations, drafted the manuscript, and made the figures and tables. CT provided unpublished interferometric axis ratio measurements as well as information concerning interferometric apparatus and measurements. CEJ provided indispensable feedback and guidance on The final draft was edited by IHC and CEJ, with CT providing useful comments on the manuscript.

The following authors contributed to Chapter 3: I. H. Cyr, C. E. Jones, D. Panoglou, A. C. Carciofi, A.T. Okazaki.

ACC first put forward the idea of using a SPH code to study the density structure of Be star disks in misaligned binary systems. ATO wrote the SPH code and provided indispensable information about the theory behind it. ATO and DP provided instructions on the operation of the code. The literature search was done by IHC, with the help of CEJ and ACC. IHC ran the simulations, performed the analysis, generated the figures and tables, and wrote the manuscript. CEJ and AAC provided guidance and feedback on the interpretation of the results. The final version was edited by IHC with the help of CEJ. DP, AAC, and ATO provided useful comments and suggestions to improve the manuscript.

The following authors contributed to Chapter 4: I. H. Cyr, C. E. Jones, D. Panoglou, A. C. Carciofi

The premise of investigating the structure of spiral density enhancements of Be star disks in binary systems was proposed by IHC and CEJ. IHC preformed the analysis, generated the figures and tables, and wrote the text. CEJ helped with the literature search and provided substantial and regular feedback during the writing of this Chapter.

Cette thèse est dédiée à mes parents, Jacques et Michèle, pour tous leurs supports, encouragements, et amours. Je n'aurais pas pu finir cette thèse sans eux. Je vous aime beaucoup.

Acknowledgments

First and foremost, I would like to thank my parents, Jacques Cyr and Michèle Ouellette, for all their support and encouragements. This thesis would not have happened without them. I would also like to extended my thanks to my thesis advisor, Dr Carol Jones, for her expertise, guidance, and patience throughout the years.

Last but not least, I extend my sincerest gratitude to all the friends that came and went through these difficult years. They provided me with much needed distractions, laughs, and support.

Contents

Listing of tables

Listing of figures

1

Introduction

On August 23rd, 1866, the director of the observatory of the *Romano Collegio* in Italy, Padre Angelo Secchi, reported seeing "une ligne lumineuse [...] plus brillante que tout le reste du spectre" in the spectra of γ Cas (Secchi, 1867). This was the first emission line B-type star, also known as Be stars, ever detected.

What are Be stars? Jaschek et al. (1981), broadly defined Be stars as "a non-supergiant B-type star whose spectrum has, or had at some time, one or more hydrogen lines in emission." Although a useful definition, it also includes such objects as pre-main sequence Herbig Ae/Be and mass transferring Algol systems, which are different than the slightly evolved main sequence Be stars. As a means of excluding these other types of stars, the term "classical" Be stars is often used. As this paper deals exclusively with "classical" Be stars, they will simply be referred to as Be stars.

Be stars are composed of two main parts; the central star and the circumstellar gas. The central star is typically a B-type star, but some late O-type and early A-type have shown similar features as Be-stars. It is estimated that Be stars represent 15 to 20% of all B-type stars (Zorec et al., 1997), this fraction being higher for earlier types, peaking for B2 spectral types (Jaschek et al., 1987). As a group, their masses typically range from 3 to 15 $M_{\odot}$, their radii

from 3 to 8 $R_\odot$, and their luminosities from 10^2 up to 10^4 $L_\odot$ (Cox, 2000). As for their evolutionary status, they are either main sequence stars (luminosity class V) or slightly evolved stars (IV-III). They are also known to be fast rotators. Their rotation is estimated to be approximately between 70% and 80% of their critical velocity (Porter et al., 2003).

Be stars are surrounded by a dense, geometrically thin, gaseous equatorial disk. The presence of these disks is what distinguishes Be stars from normal B-type stars and is the source of distinctive features, such as emission lines and IR excess. These disks however are not always present. In some Be stars, they have been observed to completely dissipate, only to reform years or even decades later.

There are still many questions to be answered about Be stars. Are Be stars born fast rotators, is this a stage in their evolution, or have they been somehow spun-up? What mechanisms are involved in the formation and dissipation of the disk? What are their precise rotation rates and what role does rotation play in the formation of these disks? Answering these questions will not only help us understand Be stars, but may also provide answers for other fields of research. Be stars offer a unique opportunity for studying stellar mass loss and disk physics, and may help us understand the interplay between stellar rotation and evolution, which is still a great uncertainty in our understanding of massive stars.

1.1 Observational properties of Be stars

One if the few ways astronomers can obtain information about objects and phenomena outside our Solar System is by studying electromagnetic radiation through the use of telescopes. Over the years, technology has allowed us to expand the range of our observations beyond the limited visual range of our eyes. Many techniques, such as polarimetry, photometry, interferometry, and spectroscopy, have also been developed to get the most information possible out of the observations we receive. In this section, we will discuss the observational properties typically observed in Be stars.

1.1.1 Optical range

The defining feature of Be stars is the presence of hydrogen emission lines observed in their spectra at some point in time (Jaschek et al., 1981). The most common emission lines are those from the Balmer series, the strongest being Hα followed by Hβ, Hγ, and so on (Jaschek et al., 1987). Stronger emission lines are associated with emitting regions that extend up to larger radii then in the disk. This implies that high order Balmer lines are restricted to smaller portions of the disk than low order lines such as Hα. The presence of higher order Balmer emission lines has been found to be related to the spectral type of the star. Jaschek et al. (1980) showed that early type stars have a tendency to have more higher order Balmer emission lines in their spectra than later types (Figure 1.1). Similarly, Kogure et al. (2007) showed that the Hα line strength (measured in terms of equivalent width) is also related to spectral type. The width of the line is typically stronger for B2-type stars and decreases for later types, as shown in Figure 1.2.

Although the most prominent, the Balmer lines are not the only emission lines observed in the visible range of Be stars' spectra. FeII emission lines, especially those in the red portion of the visible spectrum, are observed in Be stars for spectral types ranging between B0 and B5 (Jaschek et al., 1987). The intensity of these lines seems to be correlated with the intensity of the Balmer lines. Neutral helium lines are also observed in early Be stars, but less frequently. The most common helium line is λ5876 (Jaschek et al., 1987). Emission lines of SiII and MgII are also sometimes present (Porter et al., 2003).

The shape of the emission lines differs from one star to the next. They can be classified by three types: singly peaked lines, doubly peaked lines, and shell lines. Singly peaked lines are somewhat rare as they are associated with stars observed near pole-on. Doubly peaked lines, on the other hand, are common. They are characterized by two distinct peaks in the emission profile, one blue-shifted (V) and one red-shifted (R). For many Be stars, the peaks are observed to be equal in strength. However, about one-third of Be stars (Hanuschik et al., 1996) experience a cyclical variation in the height ratio of the two peaks (V/R).

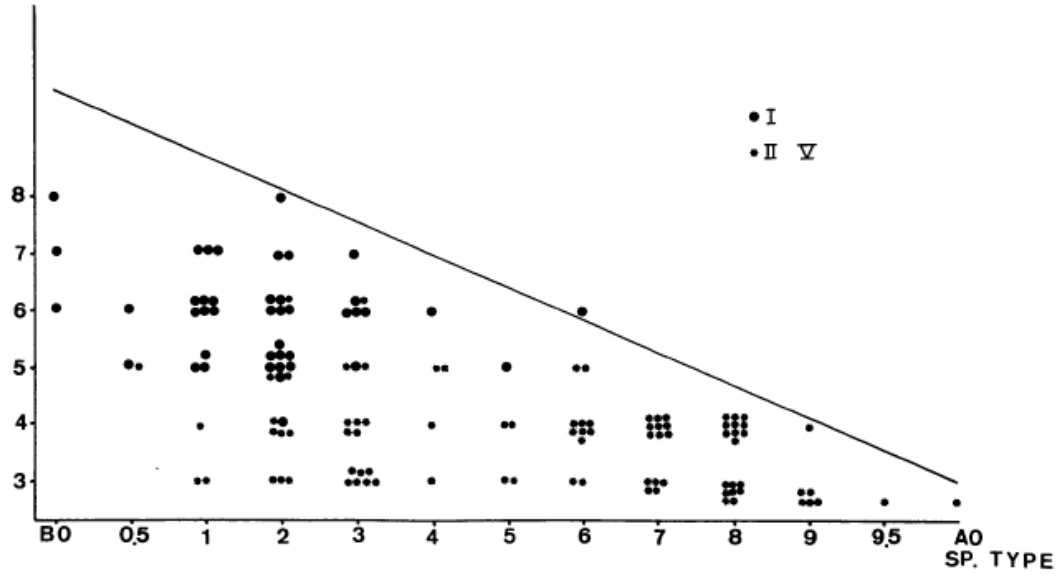

Figure 1.1: Quantum number of the highest Balmer emission line detected as a function of the spectral type of the Be star. The different symbols represent different groupings of Be stars. Figure reproduced from Jaschek et al. (1980).

This phenomenon, known as V/R variation, will be discussed further in Section 1.1.5. The shell emission lines are similar to the doubly peaked lines, but with a stronger central absorption that reaches below the continuum. Stars that exhibit these features are often referred to as Be-shell stars.

Struve (1931) was the first to propose that the difference in the profile of the emission lines is due to the different angles at which the stars are observed, as depicted in Figure 1.3. Since then, it has been a common practice to use the shape of the emission lines to estimate the inclination angle of the star with respect to its rotational axis, although this practice as been criticized in recent years. Quirrenbach et al. (1997) warns that "a shell star classification is insufficient to conclude that a star is seen edge-on", a warning echoed by Miroshnichenko et al. (2001). More recently, Silaj et al. (2010) showed that the shape of the emission lines depends on the gas density and level populations of the disk as well as the inclination.

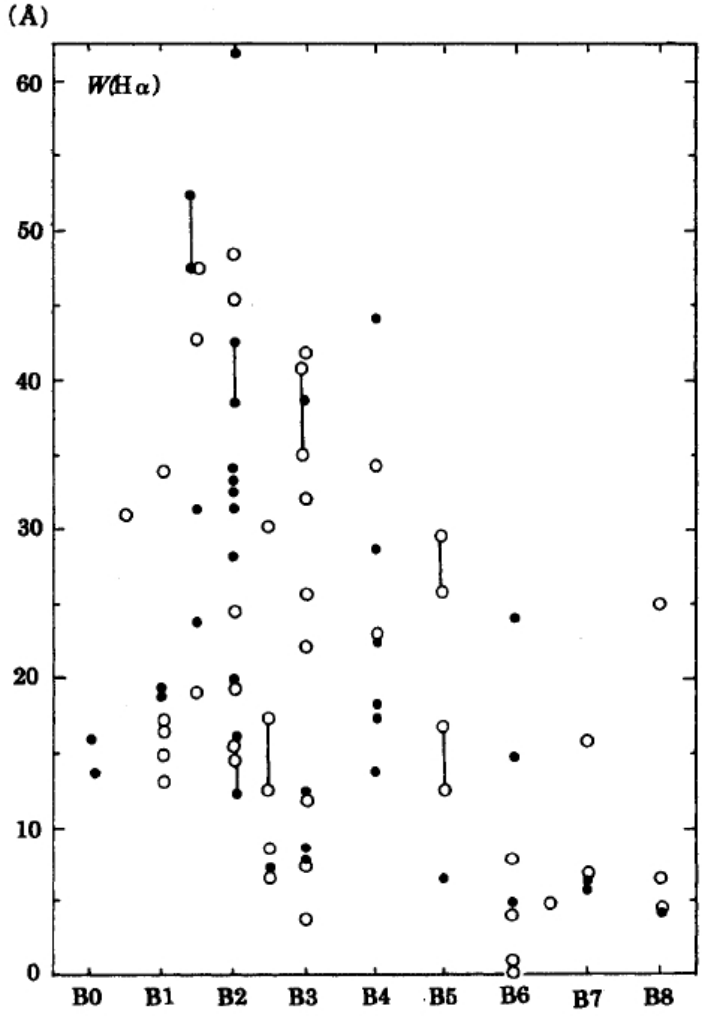

Figure 1.2: Graph of the equivalent width of the Hα emission line from Be stars as a function of stellar type. Filled circles represent data taken by Mennickent et al. (1994), and empty circles by Slettebak et al. (1992). The lines represent data from the same star taken at different epochs. Figure reproduced from Kogure et al. (2007).

1.1.2 Infrared and radio

Emission lines are also seen in the near infrared, the most prominent of which are in the Paschen series. This type of emission line appears mostly in early-type Be stars which have strong Balmer emission lines (Jaschek et al., 1987). Some Be stars however will show deep absorption lines instead of emission lines

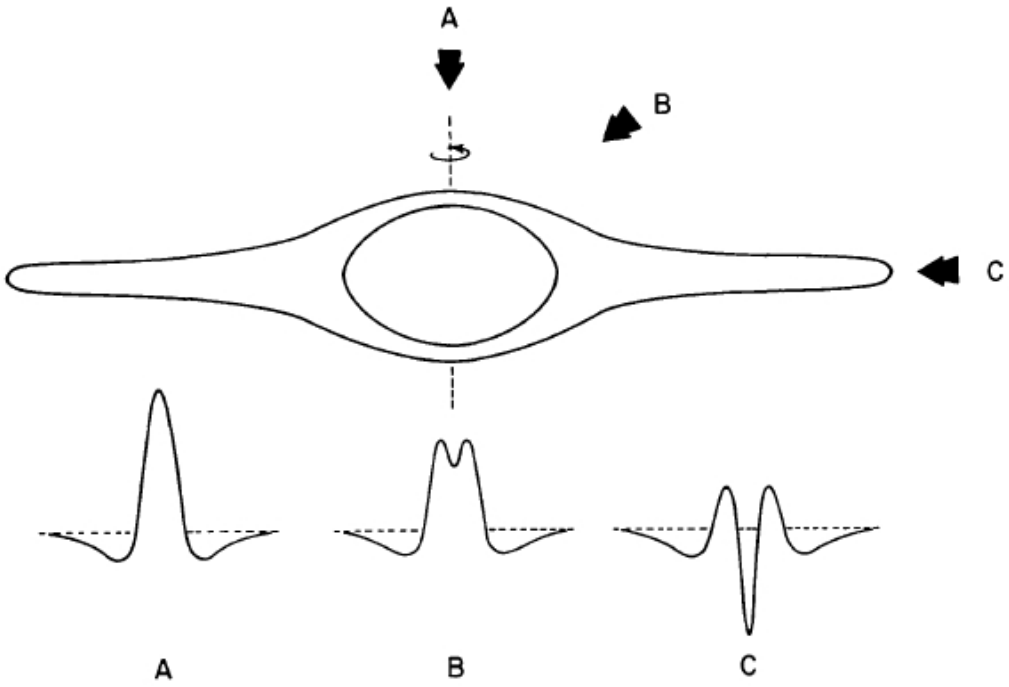

Figure 1.3: Illustration of the rotation model proposed by Struve, reproduced from Slettebak (1979). When the star is seen pole-on (point A) the emission line profile is singly peaked. When viewed at an angle (point B), the profile appears doubly peaked. Finally, when viewed edge-on (point C), the emission line resemble those of Be-shell stars.

in this series.

Andrillat et al. (1990a) has determined that the Paschen emission lines come from the inner regions of the disk and have an emission outer radius of about four stellar radii. This region is much smaller than the emitting region of the Balmer lines. Paschen emission lines are therefore useful for probing the conditions of the disk near the star. Other lines detected in the near infrared include lines from OI, CaII, FeII and NI (Andrillat et al., 1990b).

Hydrogen recombination lines have also been seen in the mid-infrared for transitions between upper levels ranging from 7 to 31 and lower levels ranging from 6 to 10 (Rinehart et al., 1999).

Be stars also show excess emission in the infrared. This excess can vary from almost non-existent to significantly large. Figure 1.4, reproduced from Wa-

ters (1986), shows the IR excess of four Be stars. Woolf et al. (1970) first attributed the excess to free-free emission from the same ionized envelope that produces the Balmer emission lines, but could not rule out the possibility of it being caused by the re-radiation of energy from a circumstellar dust cloud. However, based on photometry measurements ranging from 2.3 μm to 19.5 μm, Gehrz et al. (1974) demonstrated that the IR excess comes from the free-free emission inside gaseous stellar envelopes of temperature greater than 10000 K, and ruled out the dust cloud model. Far-infrared observations performed by the IRAS satellite later supported this explanation (Cote et al., 1987). Gehrz et al. were also able to estimate the extent of the emitting region to approximately four stellar radii, matching the estimated emitting region of the Paschen lines mentioned above. The slope of the energy distribution curve (as seen in Figure 1.4) is dependent on the density distribution in the disk (Waters, 1986).

Because both the Balmer emission lines and the infrared excesses originate in the disk, many authors have tried to find a relationship between the two. Dachs et al. (1982) studied the relation between Hα equivalent width and the (J-M) colour excess of southern early-type Be stars. Their result shows that a correlation between the two does indeed exist, but with a fair amount of scatter. More recent observations performed by van Kerkwijk et al. (1995) showed the same correlation, but again with significant scatter. A similar correlation between the IR excess luminosity and the Hα emission luminosity was found by Ashok et al. (1984).

Free-free emission can by seen in the far-IR through to the radio. Observations performed by IRAS (Waters et al., 1991) showed a steepening of the continuum energy distribution as it transitions from far-IR to radio. The turnover wavelength was also seen to vary greatly from one star to the next. Waters et al. (1994) suggested that the steepening indicates structural changes in the disk far away from the central star.

1.1.3 Ultraviolet and X-ray

Be stars and normal B-type stars have very similar features in the ultraviolet range. Ultraviolet absorption lines in both types of stars come from two distinct

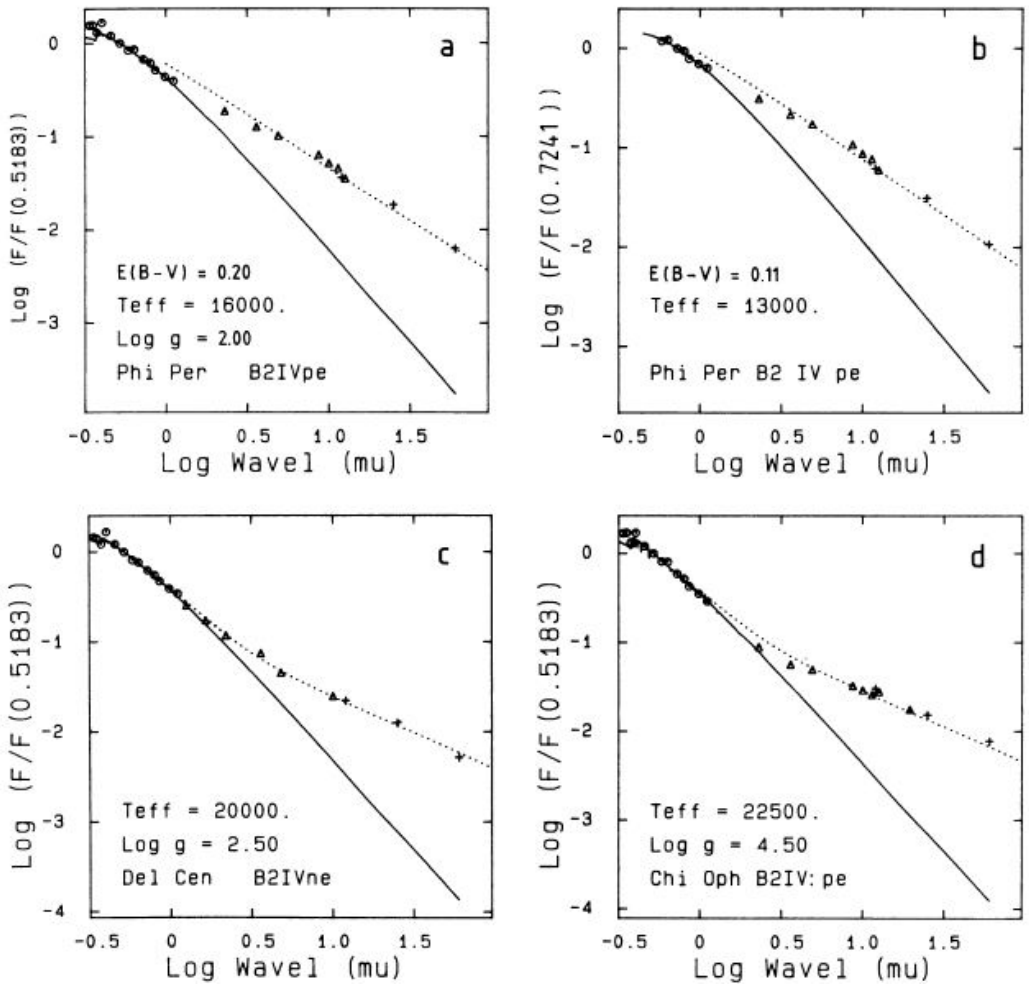

Figure 1.4: Infrared energy distributions ϕ Per (a and b) , δ Cen (c), and χ Oph (d). Black dots represent the actual measurements (different symbols denote data from different authors), solid lines are the expected distribution using Kurucz (1979) model, and dotted lines are the total contribution from the star and the disk. Figure reproduced from Waters (1986).

regions: the photosphere and the stellar wind. The intensity of these photospheric lines has been used for spectral classification of B-type stars (Henize et al., 1975; Rountree et al., 1991, to name a few). No significant difference seems to exist between the UV photospheric lines of Be stars and non-emission B-type stars (Slettebak, 1994, Figure 1.5).

Absorption lines due to stellar winds are common in massive stars and are characterized by high excitation energy, typically higher than photospheric lines, along with large terminal velocities (Kogure et al., 2007). These features indicate that the stellar wind is a low density gas with relatively high temperature. It is now widely accepted that this wind, originating from higher latitudes on the stellar surface, is unrelated to the cooler, denser, equatorial disk of gas responsible for the emission lines in the optical and IR.

Stellar winds are also a source of X-ray emission. The luminosity of this X-ray emission (L_X) can range from 10^{28} erg s^{-1} in late B-type stars up to 10^{36} erg s^{-1} in early-types (Kogure et al., 2007). Cohen (2000) compared the X-ray emission of Be stars to those of non-emission B-type stars and concluded that Be star X-ray activity may be modestly stronger, but overall, it is qualitatively not that different from the activity of normal B-type stars.

The most widely accepted mechanism for X-ray emission is shock heating caused by an instability in the winds (Lucy, 1982; Lucy et al., 1980). Other mechanisms have also been suggested, such as inverse-Compton emission and coronal heating (Cassinelli et al., 1994).

X-ray emission in Be stars can also be caused by the presence of a compact companion star. These systems are referred to as Be/X-ray binaries. Binary Be stars will be discussed later in Chapters 3 and 4.

1.1.4 Polarimetry

Another important feature of Be star spectra is the presence of linearly polarized light. The first to detect linear polarization in a Be star was Behr (1959). Since then, numerous groups have studied the polarization in both the continuum and the emission lines. The percentage of polarized light in Be stars is typically small, usually less then 2% (Porter et al., 2003).

The linear polarization observed in Be stars is attributed to the scattering of starlight by free electrons (Thomson scattering) in the flat, inner region of the circumstellar envelope. Although the scattering cross section is wavelength independent, the linear polarization spectra observed for Be stars shows a clear wavelength dependence. This dependency is caused by the absorption of light,

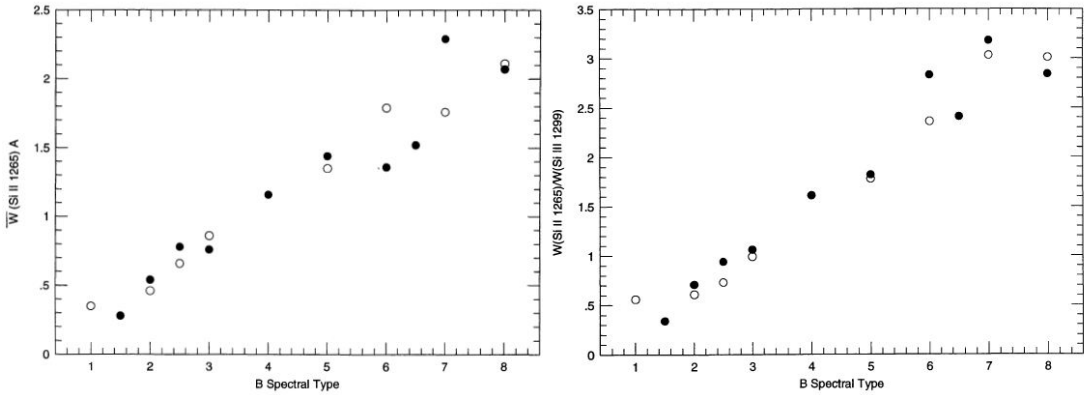

Figure 1.5: Relation between ultraviolet absorption lines and spectral type. Equivalent widths of SiII λ1265 (left) and relative intensity of SiII λ1265/SiIII λ1299 (right). Filled circles represent Be stars while open circles represents normal B-type stars. All lines are photospheric in origin. Figures reproduced from Slettebak (1994).

both polarized and unpolarized, by the neutral hydrogen in the disk, and the subsequent re-emission of unpolarized light, which dilutes the overall polarization level (Coyne et al., 1969). Figure 1.6 illustrates a model fit to the observed linear polarization spectrum of ζ Tau (Wood et al., 1997). The computational model calculates the percentage of polarized light from multiple photon scattering in a disk-shaped envelope that includes sources of continuous hydrogen opacity. As the figure shows, the model fits the Balmer and Paschen jumps quite well, but diverges significantly from the measurements in the UV region. This suggests the existence of an additional depolarization mechanism not considered by Wood et al., such as the existence of many metal lines.

Depolarization can also be seen in the Balmer emission lines. Poeckert et al. (1977) showed that for γ Cas, the depolarization in the Hα line can reach 0.2%, while Wood et al. (1997) observed a depolarization reaching 0.5% for ζ Tau (as can be seen in Figure 1.6).

Like most features of Be stars, the linear polarization signature varies with time. A notable example of this is the Be star π Aqr. McDavid (1999) found that the polarization level of this star, known to be the highest of any Be star, went from $\sim$2% in 1987 to almost non-existent in late 1990s. This drastic change in polarization, although not yet well understood, is believed to be related to

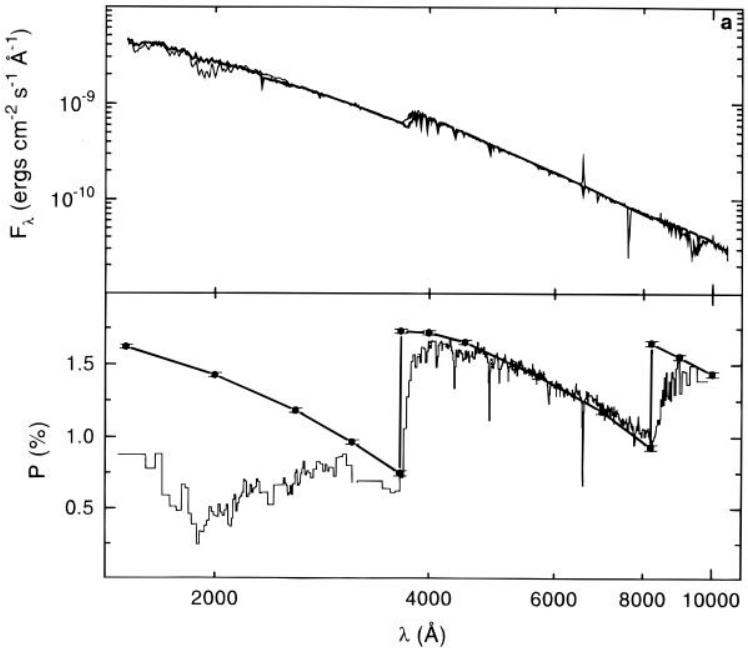

Figure 1.6: Thin disk model fit (thick lines) to observations of ζ Tau (thin lines). Top panel shows the spectra of the star while the bottom one shows its linear polarization. Figure reproduced from Wood et al. (1997).

dynamical changes in the structure of its circumstellar envelope. Kunjaya et al. (1995) also observed polarization variation in the Be star X Per. They noticed that the decrease in linear polarization in the optical continuum corresponded to a decrease in the visual magnitude and a reduction in the strength of Hα emission line. They attributed these variations to a decrease in the electron density in the envelope.

Many authors have found relationships between the level of polarization and other Be star features. Ghosh et al. (1999) looked at 29 Be stars and found that stars with weaker/stronger Hα emission also have low/high levels of polarization in the B-band. These observations are consistent with a models of circumstellar disks with sufficient optical thickness to produce the observed levels of electron scattering.

Cote et al. (1987) found that the polarization is also related to the far-IR ex-

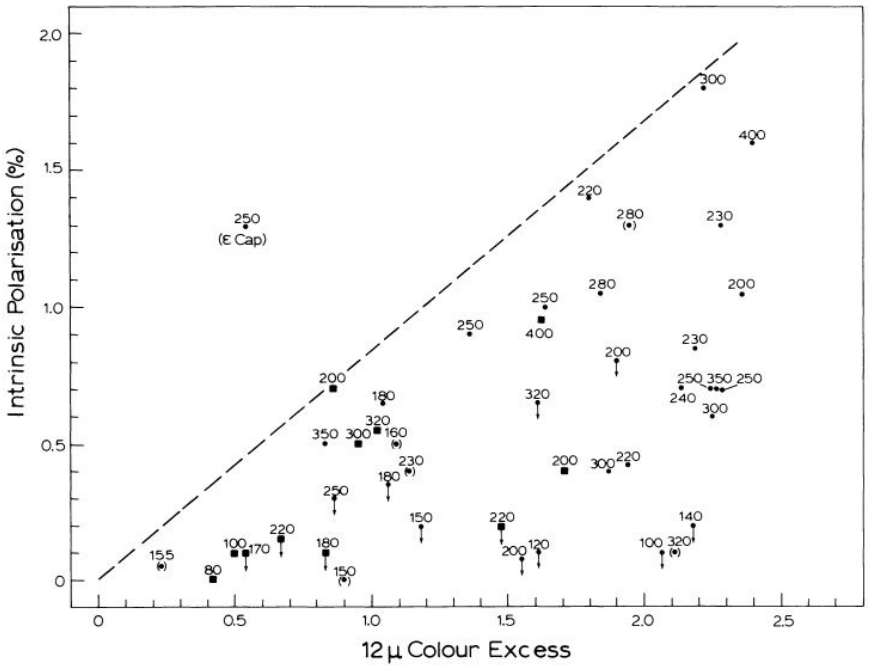

Figure 1.7: Plot of the intrinsic polarization at $\lambda = 4250$ Å as a function of colour excess at 12 μm. Early type Be stars are represented by circles while squares represent late types. Symbols in parenthesis represent uncertain measurements. Values represent the projected velocity. Figure reproduced from Cote et al. (1987).

cess. When plotting the intrinsic linear polarization as a function of the colour excess at 12μm, they observed that almost all stars are distributed below the boundary line (Figure 1.7). This boundary gives an estimate of the upper limit of the polarization, and is given by

$$P_{max} = 0.83[(V-12) - (V-12)_0], \tag{1.1}$$

where $(V-12)$ and $(V-12)_0$ are, respectively, the observed and intrinsic V-12 colour indexes. This plot is commonly referred to as the "triangle diagram".

Measurements of polarization can help estimate the orientation of Be stars. Brown et al. (1977) showed that, in the case of an single-scattering axisymmet-

ric envelope, the level of polarization is given by

$$P \propto \sin^2 i, \tag{1.2}$$

such that polarization levels are higher when the star is observed edge-on and absent when observed pole-on. Therefore, the inclination angle could be estimated from the ratio of intrinsic to maximum polarization. However, Quirrenbach et al. (1997) warns about the the limitation of this approach, as Be stars have variable intrinsic polarization and their disks are most likely optically thick to electron scattering, increasing the probability of multiple scattering. When including optical depth and multiple scattering to the calculations (Bjorkman et al., 1994; Hillier, 1994; Waters et al., 1992), it was shown that the maximum polarization is expected to occur at inclination angles of $i = 70°$.

1.1.5 Variability

Features of Be stars are rarely seen to be stable for extended periods of time. These variations are divided into three categories based on their timescales; short-term, mid-term, and long-term variations. Short-term variations commonly exhibit changes on timescales ranging from minutes to days, while mid-term and long-term variations occur over timescales ranging from years to decades, respectively.

Short-term variability

Short-term variation is seen in most early type Be stars, although they are sometimes also seen in later types. Surveys performed by Cuypers et al. (1989) and Balona et al. (1992) suggest that approximately 90% of Be stars of type B5 and earlier exhibit short-term variations while these variations are only significantly present in about 30% of the later types. The short timescale, as well as the spectral lines in which these variations are seen, seem to indicate that their formation region is either the photosphere or the immediate circumstellar environment near the star (Porter et al., 2003). Short-term variations are due to three main processes; pulsations, rotational modulation, and transient features.

Line profile variations (LPV) are typically attributed to non-radial pulsations (NRP). Other mechanisms have been suggested to explain LPVs, such as stellar spots (Balona, 1990) and corotating clouds (Balona, 1995), but current evidence gives support to NRP (see Porter et al., 2003 and Rivinius et al., 2013 for a review). Rivinius et al. (2003) showed that LPVs can be explained by NRPs in about 80% of early-type stars. NRPs are usually observed from dips and bumps traveling through line profiles. The typical variations in local effective temperature of the star due to these oscillations can range from 2000K to 3000K (Kogure et al., 2007). Evidence of pulsation has also been found in the UV (Smith, 2001).

Rotational modulations are variations in the spectrum whose cyclical period corresponds to one full stellar rotation. They were first thought to be caused by ordinary starspots, but further investigation by Balona (1995) showed that the required starspots would be too big and too cool to be consistent with observations. It has also been suggested that the circumstellar envelope might be the source of these modulations, but no numerical simulations have yet been able to reproduce the observed variations.

Spectral variations on timescales shorter than those mentioned above have been observed, and are typically referred to as transient features. One such feature reported in several stars is blueshifted absorption forming in less than 10 minutes (Peters, 1986), and lasting for about an hour (Penrod, 1986). Penrod (1986) presumed that these features arose from localized shocks and mass ejections associated with non-radial oscillations.

Mid-term variability

One type of mid-term variation is seen in the profiles of doubly peaked emission lines. As discussed in Section 1.1.1, doubly peaked emission line profiles are common in Be stars. About one-third of these stars exhibit cyclical variation in the height difference between the violet (V) and red (R) peaks, referred to as the V/R variation. The timescale for these variations is on the order of years (Hanuschik et al., 1996), which is much longer than the rotation period of the Hα emitting region in the circumstellar disk.

The currently accepted explanation for these variations is the presence of one-armed density waves in the disk, precessing around the star (Okazaki, 1991, 1996). When this region of high density is on the approach, its extra emission will be blue shifted, enhancing the V peak, while when the wave is receding, the R peak will be enhanced. Theoretical work from Kato (1983) first showed that one-armed density waves are possible in near-Keplerian thin disks, suggesting the applicability of this model to Be stars. Years later, Okazaki (1991) developed this density wave theory to explain the V/R variation of the emission line profiles. For his model, Okazaki assumed an isothermal, axisymmetric, Keplerian disk, in which he added a perturbation of the form $\exp[i(\omega t - m\phi)]$, where ϕ is the phase, ω the angular frequency, and m the oscillation mode, which is set to 1 for a one-armed oscillation. Computing the profiles of Hα emission lines using this model, Okazaki (1996) was able to reproduce V/R variation with an oscillation period in the range of years to decades, which agrees with observations. Although Okazaki's model predicted a retrograde precession of the density wave around the star, further work by Papaloizou et al. (1992) found instead that a prograde wave precession should be observed due to the flattening of the rapidly rotating central star. Observational evidence for a prograde precession was first seen by Telting et al. (1994), and later confirmed by interferometric measurements (Berio et al., 1999; Vakili et al., 1998).

This one-armed density wave model has been shown on many occasions to be in agreement with observations. Hanuschik et al. (1995) were successfully able to reproduce the quasi-cyclic V/R variation observed in the Be star δ Cen. More recently, Carciofi et al. (2009) used the one-armed model and successfully reproduced photometric, polarimetric, spectroscopic and interferometric observations of ζ Tau, a Be star known for its stable V/R cycle. The successful modeling of the V/R variation through the one-armed density wave model seems to confirm the validity of current conceptions about equatorial disks, and may help further our understanding of its dynamics and structure.

Long-term variability

One of the biggest changes observed in Be stars is the disappearance and reappearance of Be star features, or in other words, the change from a Be star phase to a normal B-type star phase and vice-versa. This change is associated with the dissipation and subsequent reformation of the equatorial disk. This variation usually takes place on timescales on the order of decades. A good example is δ Sco. Prior to 1990, δ Sco showed no evidence of emission. Although weak Hα emission was detected in 1990, the system entered a strong Hα emission and enhanced mass loss phase beginning in 2000 (Fabregat et al., 2000a; Miroshnichenko et al., 2001).

1.2 Properties of the Star

This section explores the evolutionary status, and details about stellar rotation, magnetic and binary properties of Be stars. As some of these features are not yet fully understood, a review of past work is presented.

1.2.1 Evolution

There has been a great deal of debate on whether the Be star phenomenon is a normal phase in the evolution of B-type stars or whether some stars are predisposed from birth to become Be stars.

Stellar clusters are useful testbeds to investigate the evolutionary trends of Be stars, as they provide a mostly homogeneous sample of stars all formed at around the same time. Mermilliod (1982) observed that clusters with main-sequence turn-offs in the range of O9 to B3 have a larger fraction of Be stars than older clusters. Grebel (1997) observed two young open clusters and found them to be richer in Be star compared to the surrounding field, which consists mostly of older stars. Similar results for the Magellanic clouds were presented by Keller et al. (2000). These results are often quoted as evidence of an evolutionary trend of Be stars. However, these results might also reflect the fact that a higher fraction of Be star are early B-types. In a study of open clusters, Fabregat et al. (2000b) found a lack of Be stars in clusters younger than 10 My,

even though they have a complete unevolved B main sequence. Be stars were observed in older clusters, with a higher abundance in clusters of ages between 13 and 25 My. From these results they concluded that the Be star phenomenon occurs in the latter half of B star's main sequence lifetime and proposed that this phenomenon arises from changes within the star, occurring approximately half-way in their main sequence life. However, in a study of Galactic field Be stars, Zorec et al. (1997) found they are present equally in luminosity classes from V to III, which provides evidence of an evolutionary trend.

In another avenue of study, Oudmaijer et al. (2010) studied the binary properties of Be and normal B-type star and found no significant differences in their mass ratios, flux differences, and binary separations, concluding that the initial conditions, and therefore the star formation mechanism, of both types of stars must be similar.

1.2.2 Rotation

Be stars are known to be fast rotators, typically faster than their normal B-type counterparts. In fact, Be stars as a group are considered to have the fastest rotation velocities of all non-degenerate stars. Photospheric rotation of a star is measured by looking at the broadening of its photospheric absorption lines. Other processes, such as thermal and collisional broadening, can affect the width of the lines, but rotational broadening dominates for stars with rotational velocities greater then a few tens of km s^{-1}. However, because the rotation axis of stars are usually inclined with respect to the line of sight, only the projection of the rotational velocities in the plane of the sky ($v \sin i$) can be measured. Therefore, it requires reliable estimates of the inclination angle of the stars in order to derive their actual rotational velocities. In the absence of reliable values of inclination angle, many authors have turned to statistical analysis in order study to the rotational properties of Be stars (Cranmer, 2005; Fukuda, 1982; Slettebak, 1982; Yudin, 2001).

The knowledge of how fast Be stars are rotating is crucial to understanding the mechanism which creates the circumstellar disk. Struve (1931) speculated that Be stars rotate near their break-up (critical) velocity which he proposed

as being the mechanism responsible for ejecting mass into the disk. Slettebak (1982) however found that Be stars do not rotate at critical velocities. Furthermore, Porter (1996) found that the distribution of rotational velocities peaks around 70% of critical velocity, while Chauville et al. (2001) estimated the average velocity to be 80% of critical. Although these rotational velocities are high, they are not high enough to produce mass loss in Be stars from rotation alone.

Collins et al. (1995) have proposed that measurements of $v \sin i$ are underestimated in rapidly rotating stars due to the effect of gravity darkening. As a star rotates rapidly, the poles get compressed and the star takes the shape of an oblate spheroid. Calculations by von Zeipel (1924) showed that this change in geometry causes the poles to get hotter and brighter while the equator becomes cooler and dimmer. In such a case, the highly broadened lines of the equatorial region are overshadowed by the more weakly broadened lines of the poles, causing the overall shape of the observed lines to be narrower, leading to an underestimation of the projected rotational velocity of the star. Townsend et al. (2004), after correcting for gravity darkening, estimates that the majority of Be stars could be rotating at about 95% of their critical velocity. The distortion of the star also reduces the effective gravity at the equator. According to Townsend et al., the higher rotational velocity and lower effective gravity, combined with known processes, such as pulsation and gas pressure, could provide enough velocity and energy to eject stellar mass from the equator into the circumstellar environment.

It is clear that more research into the rotation velocities of Be stars is required in order to better understand the Be phenomenon. If their rotation is indeed close to critical, this would naturally explain how the material is ejected into the disk. If, on the other hand, it turns out that Be stars rotate slower than critical, other mechanisms must be considered to explain the creation of the disk. More details about possible mechanisms are presented in Section 1.5.

1.2.3 Magnetism

Recently, the topic of magnetic fields in Be stars has been getting some attention. This interest stems from the possibility that magnetic fields may explain

some physical processes seen in these stars, such as mass and angular momentum transfer from the star to the circumstellar disk.

The possible role of magnetic fields in the formation of the disk around Be stars has been discussed often (Friend et al., 1984; Ignace et al., 1996; Poe et al., 1986). One model suggested by Cassinelli et al. (2002) is the magnetically torqued disk model, where the magnetic field of the star causes the equatorial gas to be spun up and injected into the circumstellar medium. They calculated that, for a B2 V star, the minimum magnetic field required produce a sufficient amount of torque is about 300 G. However, Maheswaran (2003) calculated that a field of only 10 G is required to sustain such a disk.

Classical Be stars have never been observed to have significant magnetic fields. Neiner et al. (2003) claimed to have observed a field of 530 ± 230 G for ω Ori, however this claim was firmly rejected by the MiMeS collaboration (Grunhut et al., 2011; Rivinius, 2012). In a survey of five Be stars, Yudin et al. (2007) detected no field greater than 100 G. A later survey (Yudin et al., 2009) found fields of 150 G in several Be stars, but Silvester et al. (2009), who observed many of the same stars, found no evidence of magnetic fields, and believes that the Yudin et al. data was not analyzed properly. More recently, Wade et al. (2012) found that, out of the 58 Be stars studied, none exhibited evidence of a magnetic field greater than 100 G. This work also refuted earlier claims by Neiner.

1.2.4 Binaries

The study of Be stars in binary systems can help us understand more about the Be phenomenon. In confirmed binaries, the presence of a companion adds certain constraints to theoretical models, for example, better estimates of stellar mass. Also, the presence of a companion may help explain star-to-disk mass transfer through tidal forces or may be responsible for the spinning up of the Be star. It has been suggested by Kriz et al. (1975) that a large portion, if not all, Be stars are interacting binaries. However, recent estimates have shown that only about 30% of Be stars are part of a binary system, which is approximately the same fraction as normal B-type stars (Oudmaijer et al., 2010).

Some binary Be stars, such as o And (Hill et al., 1988) and 66 Oph (Štefl et al., 2004), are in wide systems. In these systems, the distance of the companion is such that it is very unlikely that it has any influence on the formation of the disk. In close systems however, the companion might be close enough to help lift material off of the star and into the disk. It has been suggested that the reduced gravity along the line connecting the two binary components might be enough for the rotation of the equatorial material to become supercritical locally, causing it to be ejected into the disk. However, this would require the rotation of the star to be very close to critical ($\sim$99%), which is, by itself, fast enough for mass transfer to occur without the presence of a companion (Owocki, 2003; Struve, 1931). Although the formation of the disk might not be attributed to a binary companion, the rapid rotation of the star might be. It is known from observations that binary processes can create rapid rotation in massive stars through mass transfer. Pols et al. (1991) describe a process in which Be stars can be spun-up by the transfer of mass and angular momentum from an evolved companion star.

It is also possible that many Be stars are in binary systems with evolved stars such as black holes, white dwarfs, or neutron stars, however observations can only unambiguously confirm systems with the latter. These binaries are known as Be X-ray binaries as they show enhanced emission in the X-ray by at least a factor of 10 (Porter et al., 2003). Negueruela et al. (2001) explains these enhancements as caused by either the periastron passage of the compact companion (Type I outburst) or by "catastrophic perturbations" of circumstellar disk (Type II outburst). These types of systems are useful to study because 1) the Be star remains mostly unaffected by the presence of a companion and 2) the companion imposes constraints on model parameters, such as disk truncation, which can be used as probes. Okazaki et al. (2002) confirmed through smoothed-particle hydrodynamic simulations the disk truncation process in these types of systems. The truncation of the disk, as well other characteristics of Be star disks in binary systems will be studied in Chapters 3 and 4.

1.3 The Disk

The gas surrounding Be stars can be separated into two components: 1) a hot, diffuse, radially driven wind coming from the pole of the star, and 2) a cooler, denser, slowly outward flowing gaseous equatorial disk. As discussed in Section 1.1.3, polar winds in Be stars are practically indistinguishable from those seen in normal B-type stars. The distinguishing features of Be stars, discussed in previous sections, must therefore originate in the equatorial disk surrounding the star.

1.3.1 Geometry and orientation

Struve (1931) was the first to propose that the circumstellar envelope was concentrated around the equator of a Be star, in the shape of a disk. Although other authors have proposed different configurations, such as a spherically distributed envelope, the equatorial disk model is the most commonly accepted.

A useful tool for studying the geometric shape of the circumstellar environment is interferometry. Dougherty et al. (1992) were the first to resolve the envelope of a Be star using interferometric measurements. Their study of the Be star ψ Per at radio wavelengths confirmed the non-spherical distribution of the thermally radiating gas. Further confirmation later came from optical interferometric measurements performed by Quirrenbach et al. (1994), Stee (1995), and Quirrenbach et al. (1997).

The thickness of the equatorial disk is often defined in terms of the opening angle as depicted in Figure 1.8. Several studies attempted to estimate the distribution of opening angles. By comparing the ratio of Be-shell stars to all Be stars, Porter (1996) estimated the opening angles of 5°. However, using a similar method, Hanuschik et al. (1996) estimated an opening half angle of 13°. From spectroscopic and interferometric measurements, Quirrenbach et al. (1997) estimated the upper limit angle for ζ Tau to be 20°, which is in disagreement with Wood et al. (1997) estimate of 2.5° for the same star. Hanuschik et al. also found that the opening half-angle seems to increase as a function of distance. Because different types of measurements probe different parts of the disk, this

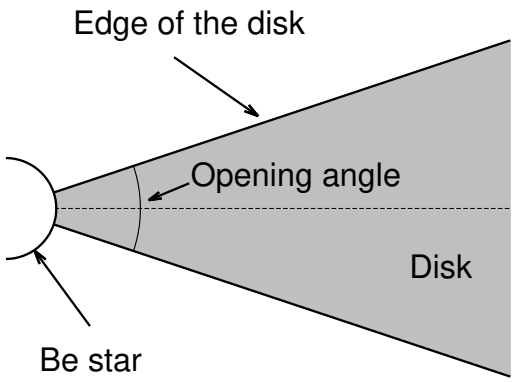

Figure 1.8: Cross-sectional view of a simplified disk model

could explain the discrepancies among opening angle measurements. Collectively, these results suggest that the disk is geometrically thin (small opening angle). See Chapter 2 for a statistical analysis of the projected size of Be star disks using interferometric measurements from the literature.

Interferometry can also be used to estimate the orientation of the star in the plane of the sky. As mentioned above, the circumstellar disk is typically regarded as geometrically thin. Using an infinitesimally thin disk approximation, a lower limit can be set on the inclination angle i of the star using the relation

$$i_{min} \leq \arccos r, \tag{1.3}$$

where r is the measurement of the projected axis ratio (ratio of minor over major axis) of the equatorial disk. This is also discussed in detail in Chapter 2.

Quirrenbach et al. (1997) showed that the polarization level can also be used as an independent estimate of inclination. They compared the polarization level relation shown in equation 1.2 with the ratio of measured to maximum polarization of six stars, calculated using the triangle diagram relation (equation 1.1,

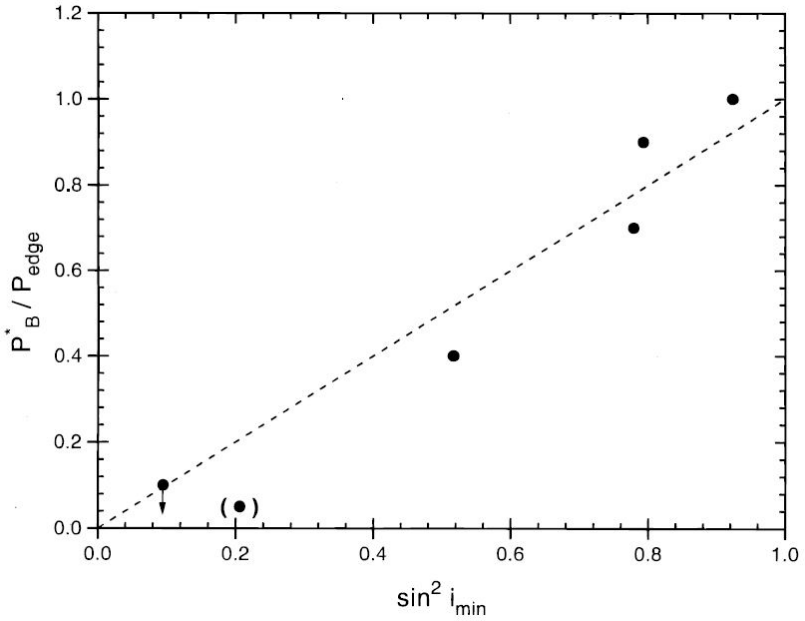

Figure 1.9: Correlation between interferometric and polarimetric estimators of inclination angle. The dashed line shows the expected correlation for an optically thin, single scattering, axisymmetric envelope and the dots represents the measurements. Figures reproduced from Quirrenbach et al. (1997).

Section 1.1.4) as a function of $\sin^2 i_{min}$, obtained through interferometric measurements (Figure 1.9). They found a relatively good agreement between the two estimates of inclination angle.

Quirrenbach et al. (1997) also compared the position angle of the minor axis obtained from interferometry with the position angle for linear polarization for several Be stars. If the envelope is indeed a thin disk, the line going through the projected minor axis should correspond to the position angle of the rotation axis of the star. They found a reasonably good agreement between the two angles, confirming the prediction of Brown et al. (1977) that the polarimetric position angle for an electron scattering axisymmetric disk should be perpendicular to the plane of the disk.

1.3.2 Density and temperature structure

As discussed in Section 1.1.2, the IR excess of Be stars arises from free-free and free-bound emission from the disk. Using this emission, Waters (1986) determined that the density distribution of the disk can be modeled using the following power law:

$$\rho(r) = \rho_0 (r/R)^{-n} \tag{1.4}$$

where R is the radius of the star, r is the distance for the rotation axis, ρ_0 is the density at the inner edge of the disk, and n is the power-law index. With further observations in the IR continuum, Waters et al. (1987) was able to constrain the value of n between 2.0 and 3.5. Both lower and higher values of n have been used to successfully model IR observations. Radio continuum studies performed by Dougherty et al. (1991) derived a higher value of the power-law index ($n > 4.0$), which could be an indication of flaring of the disk, truncation, or cooling of the gas at large radii (Porter et al., 2003). A summary of the values of n determined for Be star disks can also be found in Rivinius et al. (2013).

The temperature structure has been more difficult to determine from the IR continuum than the density structure (Waters, 1986). In the past, many authors have assumed an isothermal (or quasi-isothermal) disk model. However, in recent years, theoretical models have been able to predict the temperature structure of such disks (Carciofi et al., 2006; Millar et al., 1998; Sigut et al., 2007). These models show that the disks are nearly isothermal for low densities. As the density rises, the disk gas deviates significantly from the isothermal temperature, especially in the dense, equatorial regions where the gas temperature decreases considerably due to increases in disk opacity which blocks a large portion of the stellar radiation (Sigut et al., 2009).

1.3.3 Dynamics

A knowledge of the dynamics, as well as the density profile, is necessary in order to properly model the emission line profiles (Section 1.1.1).

The dynamics of the disk are related to the mechanism responsible for the formation of the disk. It is therefore important to determine the disk dynamics

from observations in order to understand how these disks are created. The two most common choices of disk kinematics are an angular momentum conserving (AMC) disk with a radiatively driven outflow ($v_\phi \propto r^{-1}$) and a Keplerian disk ($v_\phi \propto r^{-1/2}$) with almost no outflow ($v_r \approx 0$).

Using a rotational velocity model of $v \propto r^{-j}$, Hummel et al. (2000) showed that, for the optically thick line of Hα, the best fitting parameter for the power law is closer to $j = 0.5$ than $j = 1$, pointing toward a Keplerian disk. More recently, Meilland et al. (2007b), in an interferometric study of α Arae, were the first to obtain direct evidence of Keplerian rotation of the disk. Other works by Delaa et al. (2011), Oudmaijer et al. (2011), Stee et al. (2012), and Wheelwright et al. (2012) also confirm the presence of Keplerian or near-Keplerian rotation in Be star disks. The disks of some stars, for example κ CMa (Meilland et al., 2007a) and ψ Per (Delaa et al., 2011), however have been found to be rotating at sub-Keplerian speeds. Stee (2011) suggests that the departure from Keplerian rotation might be linked to perturbation by a close companion and/or a "one-armed" density oscillation.

Furthermore, in their study of optically thin shell lines of Fe II, Hanuschik (2000) found no evidence of radial motion, pointing therefore toward a rotation-dominated disk with little to no radial motion.

1.4 Disk formation mechanisms

How disks around Be stars are formed, maintained, and dissipated is one of the biggest remaining questions in this field of research. Two mechanisms are required to create equatorial disks; one responsible for placing material around the star and one responsible for the growth and sustainability of the disk.

1.4.1 Mass transfer mechanisms

In astrophysics, disks are commonly seen in accretion systems, where the disk is due to infalling material transported inward towards the star. These disks are typically seen in close binaries with mass exchange or in protostellar nebulae. However, not all Be stars are found in close binary systems (Section 1.2.4)

and they are far too evolved to have a protostellar disk. Moreover the disk has been seen to dissipate and reform on timescales of decades (Section 1.1.5). This means that the source of the material must be the star itself. But how is mass transfered from the star to the disk?

As previously mentioned, the first proposed model for mass ejection was made by Struve (1931). He suggested that Be stars rotate at, or near, critical velocities, and that matter near the equator is ejected due to this rapid rotation. However, as discussed in Section 1.2.2, it is unknown whether Be stars do in fact rotate at or near critical velocities, and even if their velocities are close to critical, further mechanisms are required to give the material enough velocity to escape the star.

Many mechanisms have been proposed. Kroll et al. (1997) showed, using smoothed particle hydrodynamics simulations, that material can be launched due to stellar surface explosions. Although the material is ejected indiscriminately in every direction, a sort of "Keplerian natural selection" is thought to occur, where only material launched in the direction of the rotation will have enough speed to get in orbit while the rest falls back onto the star. However, in their simulations, Kroll et al. gave the exploding material a velocity of 100-200 km s^{-1} without considering what mechanism propels the gas. According to Owocki (2006), such a surface flare would require gas temperature of the order of 10^6 K, which is much higher than observed, and would be accompanied with soft X-ray emissions, which are not observed. Another proposed mechanism for mass ejection is non-radial pulsations (NRP). Rivinius (1998) was the first to suggest that, in a least one Be star (μ Cen), outbursts responsible for mass transfer coincided with multiperiodic beating of non-radial pulsations. Many Be stars are now known to exhibit NRP. However, the velocity given to the material by NRP will be near, or slightly exceed, the sound speed at the surface of the star, which means that for a typical Be star ($c_s^2 \approx 25$ km s^{-1}, $V_{crit} \approx 500$ km s^{-1}) the star must be rotating at around 95% of its critical velocity in order for mass ejection to occur.

Some proposed models offer an explanation for both the mass transfer and growth mechanisms. One such model, proposed by Bjorkman et al. (1993), is

the wind-compressed disk (WCD) model. In this model, the radiation-driven wind observed in massive stars is deflected toward the equator due to the fast rotation of the star. With fast enough rotation, the wind streamlines from both hemispheres could cross the equatorial plane, colliding with each other and resulting in the formation of the disk. Initial numerical work by Owocki et al. (1994) seemed to confirm the viability of the model. However, some of its predictions were found to be inconsistent with observations. One of the major problems with the WCD model is that a wind-enhanced disk is likely to be angular momentum-conserving, while all observations point toward a Keplerian disk (Section 1.2.2). The model also fails to produce IR excess, which is inconsistent with observations (Porter, 1997). Work by Cranmer et al. (1995) showed that nonradial components of the line-driving force will also arise. Although weaker than the radial component, they are directed both away from the equator and in a retrograde azimuthal direction, weakening the equatorial bound wind. When gravity darkening is taken into account, polar enhanced winds instead of equator enhanced winds are generated (Owocki et al., 1996; Petrenz et al., 2000). These facts resulted in the dismissal of the WCD model. Recently, the WCD model was revived with the addition of magnetic fields (Cassinelli et al., 2000). However, not only do Be stars lack a strong, global magnetic fields (Section 1.2.3), but numerical magnetohydrodynamical simulations failed to produce the conditions necessary for the formation of a disk (Owocki et al., 2003).

1.4.2 Viscous disks model

Currently the most accepted model to explain the growth of Be star disks is the viscous decretion disk. The viscous disk model was first proposed by Pringle (1981) to explain the inward flow of material in accretion disk systems. Lee et al. (1991), followed by Porter (1999) and Okazaki (2001) later modified standard α-prescription theory to include the outward flow of material to produce Be stars. The model proposes that material from the equatorial region of the stellar atmosphere is injected, by some unknown mechanism, at Keplerian orbital velocity into the base of the disk. As material continues to be supplied by

the star, it interacts with itself as a viscous fluid, causing parts of the gas to slow down, settling into orbits closer to the star, while other parts will be spun up and will move to orbits at greater distance from the star. Angular momentum will therefore be carried outward, away from the star. For the disk to be maintained, continuous injection of angular momentum to the inner part of the disk is required.

Different approaches to solve the viscous disk problem as well as deeper analyses have been presented by various authors. For example, Carciofi et al. (2008) looked at the solution for a non-isothermal disk, while Okazaki (2007), Jones et al. (2008), and Haubois et al. (2011) described the solution for a system with a varying mass transfer rate. In this section we will outline one possible derivation of the solution for a isothermal viscous disk with constant mass transfer rate, similar to the solution presented in Carciofi et al. (2008)

Lets consider the hydrostatic structure of the disk. The case of an inviscid disk (no viscosity) is first described. In the steady-state case, the continuity and momentum equations (Navier Stokes fluids equation) in cylindrical coordinates (r,ϕ,z) can be written as:

$$\frac{1}{r}\frac{\partial(r\rho v_r)}{\partial r} + \frac{1}{r}\frac{\partial(\rho v_\phi)}{\partial \phi} + \frac{\partial(\rho v_z)}{\partial z} = 0, \tag{1.5}$$

$$v_r\frac{\partial v_r}{\partial r} + \frac{v_\phi}{r}\frac{\partial v_r}{\partial \phi} + v_z\frac{\partial v_r}{\partial z} - \frac{v_\phi^2}{r} = -\frac{1}{\rho}\frac{\partial P}{\partial r} + f_r, \tag{1.6}$$

$$v_r\frac{\partial v_\phi}{\partial r} + \frac{v_\phi}{r}\frac{\partial v_\phi}{\partial \phi} + v_z\frac{\partial v_\phi}{\partial z} + \frac{v_\phi v_r}{r} = -\frac{1}{\rho r}\frac{\partial P}{\partial \phi} + f_\phi, \tag{1.7}$$

$$v_r\frac{\partial v_z}{\partial r} + \frac{v_\phi}{r}\frac{\partial v_z}{\partial \phi} + v_z\frac{\partial v_z}{\partial z} = -\frac{1}{\rho}\frac{\partial P}{\partial z} + f_z, \tag{1.8}$$

where P is the gas pressure, ρ is the density of the gas and f_r, f_ϕ, and f_z are the components of the external force per mass element (acceleration) acting on the gas. Let us assume that the disk is in circular motion, i.e. $v_r = v_z = 0$ and $v_\phi \neq 0$. Under these conditions, only the r- and z-momentum equation

(equations 1.6 and 1.8 respectively) are non-trivial.

$$\frac{1}{\rho}\frac{\partial P}{\partial r} = \frac{v_\phi^2}{r} + f_r \tag{1.9}$$

$$\frac{1}{\rho}\frac{\partial P}{\partial z} = f_z \tag{1.10}$$

Furthermore, we will assume that the only external force is the gravity of the central star*. Therefore,

$$f_r = -\frac{GMr}{(r^2+z^2)^{3/2}} = \frac{V_{crit}^2 Rr}{(r^2+z^2)^{3/2}}, \tag{1.11}$$

and

$$f_z = -\frac{GMz}{(r^2+z^2)^{3/2}} = \frac{V_{crit}^2 Rz}{(r^2+z^2)^{3/2}}, \tag{1.12}$$

where R is the radius of the central star and V_{crit} is the critical velocity at the surface of the star ($V_{crit}^2 = GM/R$). Using the limit for a thin disk ($z \ll r$), these equations become

$$f_r = \frac{V_{crit}^2 R}{r^2}, \tag{1.13}$$

$$f_z = \frac{V_{crit}^2 Rz}{r^3}. \tag{1.14}$$

The pressure is specified using the equation of state for an isothermal gas $P = c_s^2\rho$, where c_s is the sound speed in the gas. As mentioned in Section 1.3.2, the disk is unlikely to be isothermal. However, this will give us a reasonable approximation of the solution. We note that, as $c_s^2 \ll V_{crit}^2$†, the left side term of equation 1.9 is negligible when solving for v_ϕ. Adding the pressure term and

*We are assuming that self-gravity of the disk is negligible compared to the gravitational pull of the star.

†Sound speed in these disks is estimated around 10 km s^{-1} while the critical velocity of Be stars reach several 100 km s^{-1}.

equations 1.13 and 1.14 to equations 1.9 and 1.10, we get

$$v_\phi = V_{crit}(R/r)^{1/2}, \tag{1.15}$$

$$\frac{\partial \ln(c_s^2 \rho)}{\partial z} = -\frac{V_{crit}^2 R z}{r^3}. \tag{1.16}$$

Equation 1.15 tells us that the disk rotates at Keplerian orbital speed, which is expected for a rotationally supported disk, while equation 1.16 expresses the vertical structure of the disk. Solving equation 1.16 for ρ gives

$$\rho(r, z) = \rho_0(r) \exp[-0.5(z/H)^2], \tag{1.17}$$

where ρ_0 is the density of the disk at the mid-plane ($z = 0$) and H is the scale height, given by

$$H(r) = c_s r / v_\phi. \tag{1.18}$$

Because the azimuthal velocity is proportional to $r^{-0.5}$, the scale height must therefore grow with distance as $H \propto r^{1.5}$.

To get a better idea of the radial structure of the disk, it is useful to look at the disk surface density $\Sigma(r)$. This surface density is defined as

$$\Sigma(r) = \int_{-\infty}^{\infty} \rho(r, z) dz. \tag{1.19}$$

Substituting equation 1.17 and integrating gives

$$\Sigma(r) = \sqrt{2\pi} \rho_0(r) H(r). \tag{1.20}$$

Therefore, the density function can be rewritten as

$$\rho(r, z) = \frac{\Sigma(r)}{\sqrt{2\pi} H(r)} \exp[-0.5(z/H)^2]. \tag{1.21}$$

From this last equation, it is clear that $\Sigma(r)$ is required to interpret the radial density structure. But because the we start with a non-viscous Keplerian disk,

the amount a material at any given radius is completely arbitrary. The inclusion of viscosity gives a mechanism (viscous diffusion) for material to be transported to various radii.

The viscous diffusion timescale is defined as $\tau_{diff} = r^2/\nu$, where ν is the kinematic viscosity. However, Shakura et al. (1973) noted that the diffusion timescale for molecular viscosity is far too long to grow the disk. They proposed instead that the viscosity comes from eddies and turbulence in the gas and used a parameterized kinematic viscosity

$$\nu = \alpha c_s H, \tag{1.22}$$

where the parameter α describes the ratio of the product of the eddy's speed and size to the product of the sound speed and scaleheight of the disk. With this parametrization, the diffusion timescale becomes

$$\tau_{diff} = \frac{V_{crit}}{\alpha c_s^2}\sqrt{rR} \tag{1.23}$$

$$\tau_{diff} \approx 20\text{yr}\left(\frac{0.01}{\alpha}\right)\sqrt{\frac{r}{R}}. \tag{1.24}$$

The typical timescale for the formation of disks around Be stars is on the order a few years, which would imply that α is expected to be of the order of 0.1 (Wisniewski et al., 2010).

When adding viscosity, we introduce a radial flow to the system, which implies that $v_r \neq 0$. We can, however, still consider the disk to be axisymmetric with a hydrostatic vertical structure ($v_z = 0$). It's important to note that, unless the mass transfer rate from the star to the disk is unrealistically large, the radial flow velocity will be much smaller then the sound speed ($v_r \ll c_s$). In the first order approximation, both the r- and z-momentum equations do not change. Therefore our density structure (equation 1.21) stays the same and we still have Keplerian orbital motion (equation 1.15). However, this radial velocity will affect the continuity and ϕ-momentum equations (1.5 and 1.7, respectively).

The continuity equation is reduced to

$$\frac{1}{r}\frac{\partial(r\rho v_r)}{\partial r} = 0. \tag{1.25}$$

Multiplying by r and integrating by ϕ and z gives us the continuity equation in terms of surface density

$$\frac{\partial(2\pi r\Sigma v_r)}{\partial r} = 0. \tag{1.26}$$

The term in parenthesis is equivalent to the mass "decretion" rate, i.e. the rate at which the mass is transfered to greater radii, for an axisymmetric disk of surface density $\Sigma(r)$ ($\dot{M} \equiv 2\pi r v_r \Sigma$). Equation 1.26 tells us that the mass loss rate is independent of the distance from the star, which is expected given our steady state assumption. As the system is axisymmetric and v_r and Σ are independent of z, $\dot{M}$ must be a constant. We can therefore write the outflow speed (radial velocity) as

$$v_r = \frac{\dot{M}}{2\pi r\Sigma}. \tag{1.27}$$

Now let's turn our attention to the ϕ-momentum. Because viscosity exerts a torque on the disk, an extra force related to the viscous shear stress must be added to the ϕ-momentum equation (Carciofi, 2011),

$$\begin{aligned} v_r\frac{\partial v_\phi}{\partial r} + \frac{v_\phi v_r}{r} &= \frac{1}{\rho r^2}\frac{\partial}{\partial r}\left(\nu\rho r^3\frac{\partial(v_\phi/r)}{\partial x}\right) \\ &= \frac{1}{\rho r^2}\frac{\partial}{\partial r}\left(-\frac{3}{2}r^2\alpha\rho c_s^2\right). \end{aligned} \tag{1.28}$$

Multiplying both sides by ρr^2, integrating over ϕ and z, and using the relation for radial velocity (equation 1.27), we obtain

$$\dot{M}\frac{\partial}{\partial r}\left(v_\phi r\right) = \frac{\partial}{\partial r}\left(-3\pi\alpha r^2 c_s^2\Sigma\right) = \frac{\partial\Upsilon}{\partial r}. \tag{1.29}$$

This equation expresses the fact that the change in the mass-specific angular momentum flux ($v_\phi r$) is given by the gradient of the viscous torque (Υ). Because $\dot{M}$ is constant, we can integrate equation 1.29 over r to get an expression

for the torque. The result is

$$\Upsilon(r) = \dot{M} V_{crit} \sqrt{Rr} + C, \tag{1.30}$$

where C is the integration constant. We can now isolate the surface density Σ by using the relation $\Upsilon = -3\pi\alpha r^2 c_s^2 \Sigma$ from equation 1.29 into equation 1.30,

$$\Sigma(r) = -\frac{\dot{M}}{3\pi\alpha c_s^2}\left(\frac{GM}{r^3}\right)^{1/2} + \frac{C'}{r^2}. \tag{1.31}$$

Finally, rearranging the constant C', taking into account that everything except r is constant, we get

$$\Sigma(r) = \frac{\dot{M}}{3\pi\alpha c_s^2}\left(\frac{GM}{r^3}\right)^{1/2}\left[\left(\frac{R_0}{r}\right)^{1/2} - 1\right], \tag{1.32}$$

where R_0 is a constant related to the physical size of the disk.

This last equation describes the surface density as a function of distance from the star for unbound isothermal disk. For the surface density to be fully determined, three parameters, the viscosity parameter α, the "decretion" mass rate $\dot{M}$, and disk size/age through the constant R_0, must be specified. However, for sufficiently old disks ($R \ll R_0$), the surface density structure of the inner part can be reduced to a simple power law with radius, $\Sigma(r) \propto r^{-2}$. Plugging this equation for surface density in equation 1.21, the density structure can also be expressed as a power law, $\rho \propto r^{-3.5}$, which is consistent with the findings of Waters et al. (1987), (section 1.3.2).

In a recent study, Carciofi et al. (2012) observed the Be star 28 CMa, which has recently underwent a long period of low activity, during which the disk dissipated. By modelling the rate of decline of the V-band excess using time-dependent models of dissipating viscous disks, they were able to determine, for the first time, a viscosity parameter of $\alpha = 1.0 \pm 0.2$. This result implies that the disk dissipates 10 times faster than the $\alpha = 0.1$ proposed by Wisniewski et al. (2010).

1.5 Modelling disk structure and observables

The use of numerical codes in order to model the circumstellar environment of Be star is common practice. These codes can predict observations, such as Hα emission line profiles or polarization spectra, to help better understand the processes involved in the disks.

There are two main types of numerical codes typically used in the modelling of Be stars. The first type is non-local thermodynamic equilibrium (non-LTE) code which numerically solves the radiative transfer equations. An example of this type of code is BEDISK, developed by Sigut et al. (2007). This code formally solves the radiative transfer equations by following the paths of photons from the surface of the star to the disk. One significant advantage of this code is that it assumes a solar composition for the disk instead of pure hydrogen envelope, and allows user-defined set of atomic models. However, the computational complexities that are involved with solving the radiative transfer equations makes the use of assumptions necessary, such as the axisymmetry of the disk and the assumption of a spherical nonrotating central star.

The second type of codes are non-LTE Monte Carlo (MC) simulations; an example of which is the code HDUST developed by Carciofi et al. (2006). In this code, the radiative transfer problem is solved by simulating the random propagation of photon packets through the envelope. MC simulations have the advantage of being easier to implement than traditional radiative transfer methods. Although the latter is much more efficient computationally when it comes to simple configurations, like plane-parallel or spherical geometries, MC method is frequently the only alternative for dealing with more complex situations, such as three-dimensional geometries, binary systems, and complicated density distributions.

Although both methods differ in their approaches, they simultaneously solve coupled problems of radiative transfer, and radiative and statistical equilibrium, and have been successful in modelling observations. BEDISK was used to reproduced the disk properties of γ Cas (Sigut et al., 2007), the Hα profile and IR excess of χ Oph (Tycner et al., 2008) and o Aqr (Sigut et al., 2015), and the

Hα profiles of κ Dra, β Psc, and ν Cyg, as well as constraining the properties of their disks (Jones et al., 2008), while HDUST was used by Carciofi et al. (2009) to replicated the disk properties of ζ Tau and by Silaj et al. (2016) to replicate the V/R cycle of 48 Lib.

These codes, however, have limitations. The geometry of the disks must be be specified by the user, which often implies that estimations and/or approximations are made. For example, BEDISK assumes axisymmetry of the disk. As seen in Sections 1.1.5 and 1.2.2, quasi-cyclic variations in the V/R ratios of emission line profiles observed in some Be stars indicates the presence of a one-armed density waves propagating inside the disk. In order to model these variations, non-axisymmetric disks must be considered, which means solving the time evolution of hydrodynamic equations.

One type of code design for these kind of problems is the smoothed particle hydrodynamic (SPH) code. The techniques used in these codes were first proposed by Lucy (1977) for hydrodynamic simulations of non-axisymmetric astrophysical problems. One version of this code, designed by Bate (1995), and used by Okazaki et al. (2002), is well suited to study the evolution in time of asymmetric disks. This code will be described in greater length in Chapter 3. Although this type of code provides no direct observational predictions about the disk, as it does not solve the radiative transfer equations, it does predict the density and dynamical structure of the disk which serve to give more reliable observational predictions when combined with a radiative transfer code.

1.6 Thesis statement

In this work, we study the geometry and density structure of Be star disks using various analytical methods. In Chapter 2, a statistical analysis of interferometric measurements reported in the literature is used to study the radial extent and opening angles of Be star disks over a range of wavelengths. In Chapter 3, we extend our work on the geometry of Be star disks by studying the temporal evolution of the density structure of disks formed in aligned and misaligned binary systems, using the viscous disk model and an SPH code (as described

above). In Chapter 4, we probes, in greater detail, the density enhancements that develop in these types of binary systems. Our goal in this work is to expand our understanding of the structure and dynamics of Be star disks. Although these structures cannot be directly observed, the information gathered can help us build more reliable theoretical disk models, which in turn can be used to produce more accurate predictions of the observables.

References

Andrillat, A., Jaschek, M., and Jaschek, C. (1990a). A&AS 84, pp. 11–28.

Andrillat, Y., Jaschek, M., and Jaschek, C. (1990b). A&AS 85, pp. 855–863.

Ashok, N. M., Bhatt, H. C., Kulkarni, P. V., et al. (1984). MNRAS 211, pp. 471–484.

Balona, L. A. (1990). MNRAS 245, pp. 92–100.

– (1995). MNRAS 277, p. 1547.

Balona, L. A., Cuypers, J., and Marang, F. (1992). A&AS 92, pp. 533–563.

Bate, M. (1995). PhD thesis. PhD thesis, Univ. Cambridge, (1995).

Behr, A. (1959). *Veroeffentlichungen der Universitaets-Sternwarte zu Goettingen* 7, pp. 175–180.

Berio, P., Stee, P., Vakili, F., et al. (1999). A&A 345, pp. 203–210.

Bjorkman, J. E. and Cassinelli, J. P. (1993). ApJ 409, pp. 429–449. DOI: 10.1086/172676.

Bjorkman, J. E. and Bjorkman, K. S. (1994). ApJ 436, pp. 818–830. DOI: 10.1086/174958.

Brown, J. C. and McLean, I. S. (1977). A&A 57, p. 141.

Carciofi, A. C. (2011). *IAU Symposium*. Ed. by C. Neiner, G. Wade, G. Meynet, et al. Vol. 272. IAU Symposium, pp. 325–336. DOI: 10.1017/S1743921311010738.

Carciofi, A. C. and Bjorkman, J. E. (2006). ApJ 639, pp. 1081–1094. DOI: 10.1086/499483.

– (2008). ApJ 684, pp. 1374–1383. DOI: 10.1086/589875.

Carciofi, A. C., Okazaki, A. T., Le Bouquin, J.-B., et al. (2009). A&A 504, pp. 915–927. DOI: 10.1051/0004-6361/200810962.

Carciofi, A. C., Bjorkman, J. E., Otero, S. A., et al. (2012). ApJ 744, L15, p. L15. DOI: 10.1088/2041-8205/744/1/L15.

Cassinelli, J. P., Cohen, D. H., Macfarlane, J. J., et al. (1994). ApJ 421, pp. 705–717. DOI: 10.1086/173683.

Cassinelli, J. P. and MacGregor, K. B. (2000). *IAU Colloq. 175: The Be Phenomenon in Early-Type Stars*. Ed. by M. A. Smith, H. F. Henrichs, and J. Fabregat. Vol. 214. Astronomical Society of the Pacific Conference Series, p. 337.

Cassinelli, J. P., Brown, J. C., Maheswaran, M., et al. (2002). ApJ 578, pp. 951–966. DOI: 10.1086/342654.

Chauville, J., Zorec, J., Ballereau, D., et al. (2001). A&A 378, pp. 861–882. DOI: 10.1051/0004-6361:20011202.

Cohen, D. H. (2000). *IAU Colloq. 175: The Be Phenomenon in Early-Type Stars*. Ed. by M. A. Smith, H. F. Henrichs, and J. Fabregat. Vol. 214. Astronomical Society of the Pacific Conference Series, p. 156.

Collins II, G. W. and Truax, R. J. (1995). ApJ 439, pp. 860–874. DOI: 10.1086/175225.

Cote, J. and Waters, L. B. F. M. (1987). A&A 176, pp. 93–106.

Cox, A. N. (2000).

Coyne, G. V. and Kruszewski, A. (1969). AJ 74, pp. 528–532. DOI: 10.1086/110830.

Cranmer, S. R. (2005). ApJ 634, pp. 585–601. DOI: 10.1086/491696.

Cranmer, S. R. and Owocki, S. P. (1995). ApJ 440, pp. 308–321. DOI: 10.1086/175272.

Cuypers, J., Balona, L. A., and Marang, F. (1989). A&AS 81, pp. 151–186.

Dachs, J. and Wamsteker, W. (1982). A&A 107, pp. 240–246.

Delaa, O., Stee, P., Meilland, A., et al. (2011). A&A 529, A87, A87. DOI: 10.1051/0004-6361/201015639.

Dougherty, S. M., Taylor, A. R., and Waters, L. B. F. M. (1991). A&A 248, pp. 175–178.

Dougherty, S. M. and Taylor, A. R. (1992). Nature 359, pp. 808–810. DOI: 10.1038/359808a0.

Fabregat, J., Reig, P., and Otero, S. (2000a). IAU Circ. 7461, p. 1.

Fabregat, J. and Torrejón, J. M. (2000b). A&A 357, pp. 451–459.

Friend, D. B. and MacGregor, K. B. (1984). ApJ 282, pp. 591–602. DOI: 10.1086/162238.

Fukuda, I. (1982). PASP 94, pp. 271–284. DOI: 10.1086/130977.

Gehrz, R. D., Hackwell, J. A., and Jones, T. W. (1974). ApJ 191, pp. 675–684. DOI: 10.1086/153008.

Ghosh, K., Iyengar, K. V. K., Ramsey, B. D., et al. (1999). AJ 118, pp. 1061–1072. DOI: 10.1086/300953.

Grebel, E. K. (1997). A&A 317, pp. 448–458.

Grunhut, J. H., Wade, G. A., and the MiMeS Collaboration (2011). *ArXiv e-prints*.

Hanuschik, R. W. (2000). *IAU Colloq. 175: The Be Phenomenon in Early-Type Stars*. Ed. by M. A. Smith, H. F. Henrichs, and J. Fabregat. Vol. 214. Astronomical Society of the Pacific Conference Series, p. 518.

Hanuschik, R. W., Hummel, W., Dietle, O., et al. (1995). A&A 300, p. 163.

Hanuschik, R. W., Hummel, W., Sutorius, E., et al. (1996). A&AS 116, pp. 309–358.

Haubois, X., Carciofi, A. C., Okazaki, A. T., et al. (2011). *IAU Symposium*. Ed. by C. Neiner, G. Wade, G. Meynet, et al. Vol. 272. IAU Symposium, pp. 396–397. DOI: 10.1017/S1743921311010891.

Henize, K. G., Wray, J. D., Parsons, S. B., et al. (1975). ApJ 199, pp. L119–L121. DOI: 10.1086/181862.

Hill, G. M., Walker, G. A. H., Dinshaw, N., et al. (1988). PASP 100, pp. 243–250. DOI: 10.1086/132161.

Hillier, D. J. (1994). A&A 289, pp. 492–504.

Hummel, W. and Vrancken, M. (2000). A&A 359, pp. 1075–1084.

Ignace, R., Cassinelli, J. P., and Bjorkman, J. E. (1996). ApJ 459, p. 671. DOI: 10.1086/176932.

Jaschek, C. and Jaschek, M. (1987). Cambridge: University Press, 1987.

Jaschek, M., Jaschek, C., Hubert-Delplace, A.-M., et al. (1980). A&AS 42, pp. 103–114.

Jaschek, M., Slettebak, A., and Jaschek, C. (1981).

Jones, C. E., Tycner, C., Sigut, T. A. A., et al. (2008). ApJ 687, pp. 598–607. DOI: 10.1086/591726.

Kato, S. (1983). PASJ 35, pp. 249–261.

Keller, S. C., Bessell, M. S., and Da Costa, G. S. (2000). *IAU Colloq. 175: The Be Phenomenon in Early-Type Stars*. Ed. by M. A. Smith, H. F. Henrichs, and J. Fabregat. Vol. 214. Astronomical Society of the Pacific Conference Series, p. 75.

Kogure, T. and Leung, K.-C. (2007). New York ; London : Springer, c2007.

Kriz, S. and Harmanec, P. (1975). *Bulletin of the Astronomical Institutes of Czechoslovakia* 26, pp. 65–81.

Kroll, P. and Hanuschik, R. W. (1997). *IAU Colloq. 163: Accretion Phenomena and Related Outflows*. Ed. by D. T. Wickramasinghe, G. V. Bicknell, and L. Ferrario. Vol. 121. Astronomical Society of the Pacific Conference Series, p. 494.

Kunjaya, C. and Hirata, R. (1995). PASJ 47, pp. 589–604.

Kurucz, R. L. (1979). ApJS 40, pp. 1–340. DOI: 10.1086/190589.

Lee, U., Osaki, Y., and Saio, H. (1991). MNRAS 250, pp. 432–437.

Lucy, L. B. (1977). AJ 82, pp. 1013–1024. DOI: 10.1086/112164.

– (1982). ApJ 255, pp. 286–292. DOI: 10.1086/159827.

Lucy, L. B. and White, R. L. (1980). ApJ 241, pp. 300–305. DOI: 10.1086/158342.

Maheswaran, M. (2003). ApJ 592, pp. 1156–1172. DOI: 10.1086/375797.

McDavid, D. (1999). PASP 111, pp. 494–509. DOI: 10.1086/316349.

Meilland, A., Millour, F., Stee, P., et al. (2007a). A&A 464, pp. 73–79. DOI: 10.1051/0004-6361:20065410.

Meilland, A., Stee, P., Vannier, M., et al. (2007b). A&A 464, pp. 59–71. DOI: 10.1051/0004-6361:20064848.

Mennickent, R. E., Vogt, N., Barrera, L. H., et al. (1994). A&AS 106, pp. 427–439.

Mermilliod, J. C. (1982). A&A 109, p. 48.

Millar, C. E. and Marlborough, J. M. (1998). ApJ 494, p. 715. DOI: 10.1086/305229.

Miroshnichenko, A. S., Fabregat, J., Bjorkman, K. S., et al. (2001). A&A 377, pp. 485–495. DOI: 10.1051/0004-6361:20010911.

Negueruela, I., Okazaki, A. T., Fabregat, J., et al. (2001). A&A 369, pp. 117–131. DOI: 10.1051/0004-6361:20010077.

Neiner, C., Hubert, A.-M., Frémat, Y., et al. (2003). A&A 409, pp. 275–286. DOI: 10.1051/0004-6361:20031086.

Okazaki, A. T. (1991). PASJ 43, pp. 75–94.

– (1996). PASJ 48, pp. 305–315.

– (2001). PASJ 53, pp. 119–125.

– (2007). *Active OB-Stars: Laboratories for Stellare and Circumstellar Physics*. Ed. by A. T. Okazaki, S. P. Owocki, and S. Stefl. Vol. 361. Astronomical Society of the Pacific Conference Series, p. 230.

Okazaki, A. T., Bate, M. R., Ogilvie, G. I., et al. (2002). MNRAS 337, pp. 967–980. DOI: 10.1046/j.1365-8711.2002.05960.x.

Oudmaijer, R. D. and Parr, A. M. (2010). MNRAS 405, pp. 2439–2446. DOI: 10.1111/j.1365-2966.2010.16609.x.

Oudmaijer, R. D., Wheelwright, H. E., Carciofi, A. C., et al. (2011). *IAU Symposium*. Ed. by C. Neiner, G. Wade, G. Meynet, et al. Vol. 272. IAU Symposium, pp. 418–419. DOI: 10.1017/S1743921311011008.

Owocki, S. (2006). *Stars with the B[e] Phenomenon*. Ed. by M. Kraus and A. S. Miroshnichenko. Vol. 355. Astronomical Society of the Pacific Conference Series, p. 219.

Owocki, S. and Ud-Doula, A. (2003). *Magnetic Fields in O, B and A Stars: Origin and Connection to Pulsation, Rotation and Mass Loss*. Ed. by L. A. Balona, H. F. Henrichs, and R. Medupe. Vol. 305. Astronomical Society of the Pacific Conference Series, p. 350.

Owocki, S. P. (2003). *A Massive Star Odyssey: From Main Sequence to Supernova*. Ed. by K. van der Hucht, A. Herrero, and C. Esteban. Vol. 212. IAU Symposium, p. 281.

Owocki, S. P., Cranmer, S. R., and Blondin, J. M. (1994). ApJ 424, pp. 887–904. DOI: 10.1086/173938.

Owocki, S. P., Cranmer, S. R., and Gayley, K. G. (1996). ApJ 472, p. L115. DOI: 10.1086/310372.

Papaloizou, J. C., Savonije, G. J., and Henrichs, H. F. (1992). A&A 265, pp. L45–L48.

Penrod, G. D. (1986). PASP 98, p. 35. DOI: 10.1086/131715.

Peters, G. J. (1986). ApJ 301, pp. L61–L65. DOI: 10.1086/184624.

Petrenz, P. and Puls, J. (2000). A&A 358, pp. 956–992.

Poe, C. H. and Friend, D. B. (1986). ApJ 311, pp. 317–325. DOI: 10.1086/164773.

Poeckert, R. and Marlborough, J. M. (1977). ApJ 218, pp. 220–226. DOI: 10.1086/155673.

Pols, O. R., Cote, J., Waters, L. B. F. M., et al. (1991). A&A 241, pp. 419–438.

Porter, J. M. (1996). MNRAS 280, pp. L31–L35.

– (1997). A&A 324, pp. 597–605.

– (1999). A&A 348, pp. 512–518.

Porter, J. M. and Rivinius, T. (2003). PASP 115, pp. 1153–1170. DOI: 10.1086/378307.

Pringle, J. E. (1981). ARA&A 19, pp. 137–162. DOI: 10.1146/annurev.aa.19.090181.001033.

Quirrenbach, A., Buscher, D. F., Mozurkewich, D., et al. (1994). A&A 283, pp. L13–L16.

Quirrenbach, A., Bjorkman, K. S., Bjorkman, J. E., et al. (1997). ApJ 479, p. 477. DOI: 10.1086/303854.

Rinehart, S. A., Houck, J. R., and Smith, J. D. (1999). AJ 118, pp. 2974–2987. DOI: 10.1086/301119.

Rivinius, T. (1998). PhD thesis. PhD Thesis, Landessternwarte Heidelberg/Königstuhl (1998).

– (2012). *ArXiv e-prints*.

Rivinius, T., Baade, D., and Štefl, S. (2003). A&A 411, pp. 229–247. DOI: 10.1051/0004-6361:20031285.

Rivinius, T., Carciofi, A. C., and Martayan, C. (2013). A&A Rev. 21, 69, p. 69. DOI: 10.1007/s00159-013-0069-0.

Rountree, J. and Sonneborn, G. (1991). ApJ 369, pp. 515–528. DOI: 10.1086/169781.

Secchi, A. (1867). *Astronomische Nachrichten* 68, p. 63.

Shakura, N. I. and Sunyaev, R. A. (1973). A&A 24, pp. 337–355.

Sigut, T. A. A. and Jones, C. E. (2007). ApJ 668, pp. 481–491. DOI: 10.1086/521209.

Sigut, T. A. A., McGill, M. A., and Jones, C. E. (2009). ApJ 699, pp. 1973–1981. DOI: 10.1088/0004-637X/699/2/1973.

Sigut, T. A. A., Tycner, C., Jansen, B., et al. (2015). ApJ 814, 159, p. 159. DOI: 10.1088/0004-637X/814/2/159.

Silaj, J., Jones, C. E., Tycner, C., et al. (2010). ApJS 187, pp. 228–250. DOI: 10.1088/0067-0049/187/1/228.

Silaj, J., Jones, C. E., Carciofi, A. C., et al. (2016). ApJ 826, 81, p. 81. DOI: 10.3847/0004-637X/826/1/81.

Silvester, J., Neiner, C., Henrichs, H. F., et al. (2009). *IAU Symposium*. Vol. 259. IAU Symposium, pp. 391–392. DOI: 10.1017/S1743921309030816.

Slettebak, A. (1979). Space Sci. Rev. 23, pp. 541–580. DOI: 10.1007/BF00212356.

– (1982). ApJS 50, pp. 55–83. DOI: 10.1086/190820.

– (1994). ApJS 94, pp. 163–182. DOI: 10.1086/192077.

Slettebak, A., Collins II, G. W., and Truax, R. (1992). ApJS 81, pp. 335–376. DOI: 10.1086/191696.

Smith, M. A. (2001). ApJ 562, pp. 998–1011. DOI: 10.1086/323846.

Stee, P. (1995). Ap&SS 224, pp. 561–562. DOI: 10.1007/BF00667955.

– (2011). *IAU Symposium*. Ed. by C. Neiner, G. Wade, G. Meynet, et al. Vol. 272. IAU Symposium, pp. 313–324. DOI: 10.1017/S1743921311010726.

Stee, P., Delaa, O., Monnier, J. D., et al. (2012). A&A 545, A59, A59. DOI: 10.1051/0004-6361/201219234.

Struve, O. (1931). ApJ 73, p. 94. DOI: 10.1086/143298.

Telting, J. H., Heemskerk, M. H. M., Henrichs, H. F., et al. (1994). A&A 288, pp. 558–560.

Townsend, R. H. D., Owocki, S. P., and Howarth, I. D. (2004). MNRAS 350, pp. 189–195. DOI: 10.1111/j.1365-2966.2004.07627.x.

Tycner, C., Jones, C. E., Sigut, T. A. A., et al. (2008). ApJ 689, pp. 461–470. DOI: 10.1086/592097.

Štefl, S., Hadrava, P., Baade, D., et al. (2004). *Stellar Rotation*. Ed. by A. Maeder and P. Eenens. Vol. 215. IAU Symposium, p. 166.

Vakili, F., Mourard, D., Stee, P., et al. (1998). A&A 335, pp. 261–265.

van Kerkwijk, M. H., Waters, L. B. F. M., and Marlborough, J. M. (1995). A&A 300, p. 259.

von Zeipel, H. (1924). MNRAS 84, p. 702.

Wade, G. A., Grunhut, J. H., and the MiMeS Collaboration (2012). *ArXiv e-prints*.

Waters, L. B. F., Marlborough, J. M., van der Veen, W. E. C., et al. (1991). A&A 244, pp. 120–130.

Waters, L. B. F. M. (1986). A&A 162, pp. 121–139.

Waters, L. B. F. M., Cote, J., and Lamers, H. J. G. L. M. (1987). A&A 185, pp. 206–224.

Waters, L. B. F. M. and Marlborough, J. M. (1992). A&A 256, pp. 195–204.

– (1994). *Pulsation; Rotation; and Mass Loss in Early-Type Stars*. Ed. by L. A. Balona, H. F. Henrichs, and J. M. Le Contel. Vol. 162. IAU Symposium, p. 399.

Wheelwright, H. E., Bjorkman, J. E., Oudmaijer, R. D., et al. (2012). MNRAS 423, pp. L11–L15. DOI: 10.1111/j.1745-3933.2012.01241.x.

Wisniewski, J. P., Draper, Z. H., Bjorkman, K. S., et al. (2010). ApJ 709, pp. 1306–1320. DOI: 10.1088/0004-637X/709/2/1306.

Wood, K., Bjorkman, K. S., and Bjorkman, J. E. (1997). ApJ 477, p. 926. DOI: 10.1086/303747.

Woolf, N. J., Stein, W. A., and Strittmatter, P. A. (1970). A&A 9, p. 252.

Yudin, R., Hubrig, S., Pogodin, M., et al. (2009). *IAU Symposium*. Vol. 259. IAU Symposium, pp. 397–398. DOI: 10.1017/S1743921309030841.

Yudin, R. V. (2001). A&A 368, pp. 912–931. DOI: 10.1051/0004-6361:20000577.

Yudin, R. V., Hubrig, S., Schöller, M., et al. (2007). *Active OB-Stars: Laboratories for Stellare and Circumstellar Physics*. Ed. by A. T. Okazaki, S. P. Owocki, and S. Stefl. Vol. 361. Astronomical Society of the Pacific Conference Series, p. 536.

Zorec, J. and Briot, D. (1997). A&A 318, pp. 443–460.

2

Statistical Analysis of Be Star Axis Ratios

2.1 Introduction

Classical Be stars are fast rotating, non-supergiant B-type stars surrounded by a thin gaseous Keplerian disk. The majority of the distinctive spectral features of Be stars (such as Balmer emission lines, infrared excess, polarization) originates from this circumstellar envelope. It is now widely accepted that the disk does not form from infalling material, as is the case in accretion systems, but rather from outflowing material from the central star itself, in what is sometime referred to as a "decretion" system.

The structure of these circumstellar envelopes has been the subject of many studies. Behr (1959) was the first to measure linear polarization in a Be star, which gave the first evidence that the envelope might have a preferred orientation as opposed to a purely spherical shape. Later studies performed by Dougherty et al. (1992), Quirrenbach et al. (1994), Stee (1995), and Quirrenbach et al. (1997), to name a few, confirmed that the envelope was not spherical, but disk

shaped. It is now widely accepted that the gas envelopes around Be stars are in the shape of a thin disk. However, the question remains, exactly how thin are these disks?

The thickness of the equatorial disk is often defined in terms of the opening angle. Several studies attempted to estimate the opening angles of Be star disks. By comparing the ratio of Be-shell stars to all Be stars, Porter (1996) estimated the opening angles of 5°. However, using a similar method, Hanuschik et al. (1996) estimated an opening half-angle of 13°. From spectroscopic and interferometric measurements, Quirrenbach et al. (1997) estimated the upper limit of the opening half-angle for ζ Tau to be 20°, whereas Wood et al. (1997) estimated 2.5° for the same star.

In recent years, many groups have used optical interferometry to study the shape and extent of Be star disks. One common measurement is the projected axis ratio of the disk, that is the ratio of the shortest to the longest axis as projected in the plane of the sky (i.e. the minor to major axis ratio).

Measurements of axis ratios have been widely used, and still are, to investigate the geometry and extent of elliptical galaxies (Lambas et al., 1992; Sandage et al., 1970), globular clusters (Fall et al., 1983) as well as molecular cloud cores and bok globules (Jones et al., 2001, 2002; Ryden, 1996). Only recently has the number of available measurements of Be star disk ratios been large enough to attempt such a study for these objects.

In this work, a new method of deprojecting the true shape distribution of Be star disks using observed axis ratios is presented. We accomplish this by constructing a set of simulated observations, using disk models and various shape distributions, which we compare to actual observations using Bayesian statistics.

2.2 Observational data

Interferometric instruments allow us to observe objects at a much smaller angular scale than conventional telescopes. Interferometry is therefore the perfect tool to study the shape and extent of Be star disk. The current generation of interferometric instruments typically have an angular resolution of the order

of milliarcsecond (Gies et al., 2007; Tycner, 2011). Despite this, the number of projected axis ratio measurements are still limited to Be stars within a few hundred parsecs of the Earth.

It's important to note that interferometry does not measure axis ratios directly, as it is not possible to directly image the disks, but instead measures the visibility of the star/disk system for a given baseline. These measurements provide information on the projected extent of the disk along the axis parallel to the baseline used. Once enough measurements are acquired, models of the expected visibility curve for the Be star system are then applied to the observations and their parameters are adjusted until a best fit is found. Typical free parameters of these models include angular size of the major and minor axis, from which the axis ratio can be calculated. More details on the methodology and models used can be found in the papers referred to at the bottom of Table 2.1.

All axis ratio measurements used in this work were obtained through interferometric measurements and were gathered from the literature. Measurements were selected following certain criteria. Only measurements within certain wavelength regimes were considered, namely the K-band, H-band, N-band, and at the Hα emission line. We also rejected axis ratios that were used as a fixed parameter within the model fitting, as those values were assumed prior to the measurements as opposed to deduced from them. Finally, we rejected measurements with very high level of uncertainties (typically those around or greater than 1.0).*

Table 2.1 shows the resulting compilation of observed axis ratios. These ratios are ordered by the HR number of their corresponding star. Also provided in Table 2.1 are the common name for each star, the wavelength regime of the observation, and the reference for each observation. Note that some author(s) used two or more different models in order to fit the same measurements, resulting in two or more ratio values for the same star. In those cases, all ratio values were included, unless these models were explicitly rejected by the author(s) of that particular study.

*Section 2.3.4 discusses how the uncertainty is used to weight each measurement.

Table 2.1: Observed apparent axis ratios from literature.

HR Number	Star Name	Wavelength regime	Ratio
HR 193	o Cas	K-band	0.58 ± 0.10[1]
HR 264	γ Cas	Hα line	0.70 ± 0.02[2]
			0.77 ± 0.02[2]
			0.79 ± 0.03[3]
			0.58 ± 0.03[4]
		H-band	0.75 ± 0.05[5]
		K-band	0.59 ± 0.04[6]
			0.72 ± 0.04[1]
HR 496	ϕ Per	Hα line	0.46 ± 0.04[2]
			0.47 ± 0.05[2]
			0.27 ± 0.01[4]
HR 936	β Per	K-band	0.75 ± 0.04[7]
HR 1087	ψ Per	Hα line	0.35 ± 0.03[8]
			0.47 ± 0.11[2]
			0.54 ± 0.07[2]
			0.33 ± 0.01[9]
		K-band	0.25 ± 0.56[1]
HR 1165	η Tau	Hα line	0.95 ± 0.22[2]
			0.98 ± 0.06[2]
			0.75 ± 0.05[3]
HR 1180	28 Tau	K-band	0.74 ± 0.10[7]

Table 2.1 – Continued

HR Number	Star Name	Wavelength regime	Ratio
HR 1273	48 Per	Hα line	0.76 ± 0.08[8]
			0.86 ± 0.18[2]
			0.89 ± 0.13[2]
			0.71 ± 0.03[9]
HR 1910	ζ Tau	Hα line	0.30 ± 0.03[10]
			0.28 ± 0.02[2]
			0.30 ± 0.02[2]
			0.31 ± 0.07[11]
		H-band	0.24 ± 0.14[12]
		K-band	0.09 ± 0.22[6]
			0.15 ± 0.03[1]
HR 2845	β CMi	Hα line	0.69 ± 0.15[3]
		H-band	0.76 ± 0.10[13]
HR 4830	BZ Cru	K-band	0.62 ± 0.01[14]
		H-band	0.64 ± 0.02[14]
HR 5938	4 Her	K-band	0.27 ± 0.08[1]
HR 5941	48 Lib	H-band	0.60 ± 0.11[15]
HR 5953	δ Sco	H-band	0.77 ± 0.21[16]
HR 6510	α Ara	K-band	0.37 ± 0.12[17]
		N-band	0.38 ± 0.18[17]
			0.42 ± 0.17[17]
HR 6779	o Her	K-band	0.44 ± 0.28[1]
HR 7106	β Lyr	K-band	0.60 ± 0.05[7]
HR 7763	P Cyg	K-band	0.85 ± 0.02[7]

Table 2.1 – Continued

HR Number	Star Name	Wavelength regime	Ratio
HR 8146	υ Cyg	K-band	0.26 ± 0.13[1]
			0.42 ± 0.30[7]
HR 8402	o Aqr	K-band	0.25 ± 0.06[1]
HR 8773	β Psc	K-band	0.70 ± 0.15[1]

References: 1. Touhami et al. (2013); 2. Quirrenbach et al. (1997); 3. Tycner et al. (2005); 4. Tycner et al. (2006); 5. Smith et al. (2012); 6. Gies et al. (2007); 7. Grzenia et al. (2013); 8. Delaa et al. (2011); 9. Grzenia et al. (2013); 10. Quirrenbach (1994); 11. Tycner et al. (2004); 12. Schaefer et al. (2010); 13. Kraus et al. (2012); 14. Stee et al. (2013); 15. Stee et al. (2012); 16. Millan-Gabet et al. (2010); 17. Meilland et al. (2009)

2.3 Theory

2.3.1 Viscous Disk Models

At present, the viscous decretion disk model is the most widely accepted model to explain Be star disk growth. It was first proposed by Shakura et al. (1973) as a way to explain the inward flow of material in accretion disk systems, such as forming stars and black holes. The model was later modified (Lee et al., 1991; Okazaki, 2001; Porter, 1999) using the standard α-prescription theory to include systems with outward flow of material, such as Be stars. The model proposes that material from the equatorial region of the stellar atmosphere is injected at Keplerian orbital velocity into the base of the disk by some yet unknown mechanism. If the material is steadily supplied by the star, it will start interacting

with itself through a process referred to as viscosity, causing parts of the gas to slow down and settle into orbits close to the star, and other parts to spun up and move to greater radial distance from the star. Angular momentum will therefore be transferred from the star and carried outward into the disk.

Further understanding of this model requires solving the hydrodynamic equations. We will not go through the derivations in this work, however, different approaches to solve these equations as well as their interpretations have been presented by various authors. Carciofi et al. (2008) looked at the solution for a non-isothermal disk, while Okazaki (2007) and Haubois et al. (2011) described the solution for a system with a varying mass transfer rate. For this discussion, we will look at the results presented in Carciofi (2011). Starting with some basic assumptions (no self gravity in the disk, slow radial velocity component, and a vertical structure in hydrostatic equilibrium), the following density structure equation is obtained:

$$\rho(r, z) = \rho_0 r^{-n} \exp[-0.5(z/H)^2], \tag{2.1}$$

where ρ_0 is the density at the base of the disk, r and z are the radial distance and height above the disk, respectively (both are expressed in stellar radii), n is the power law describing how the density falls off, and H is the scale height of the disk. The scale height $H(r)$ depends on the sound speed inside the disk (c_s) and the Keplerian velocity at the equator of the star ($V_{\rm Kep}$):

$$H(r) = \frac{c_s}{V_{\rm Kep}} r^{3/2}. \tag{2.2}$$

Using these equations, Carciofi (2011) derives a value of 3.5 for n in the case of an isothermal disk. However, values ranging from 2 to 5 have been found for IR observations (Waters et al., 1987), interferometric measurements (Jones et al., 2008; Tycner et al., 2008), and from the Hα line profile modelling (Silaj et al., 2010). As an example, Figure 2.1 shows the density structure of a disk with $\rho_0 = 10^{-10}$ g cm^{-3} and $n = 3.5$, based on Equations (2.1) and (2.2).

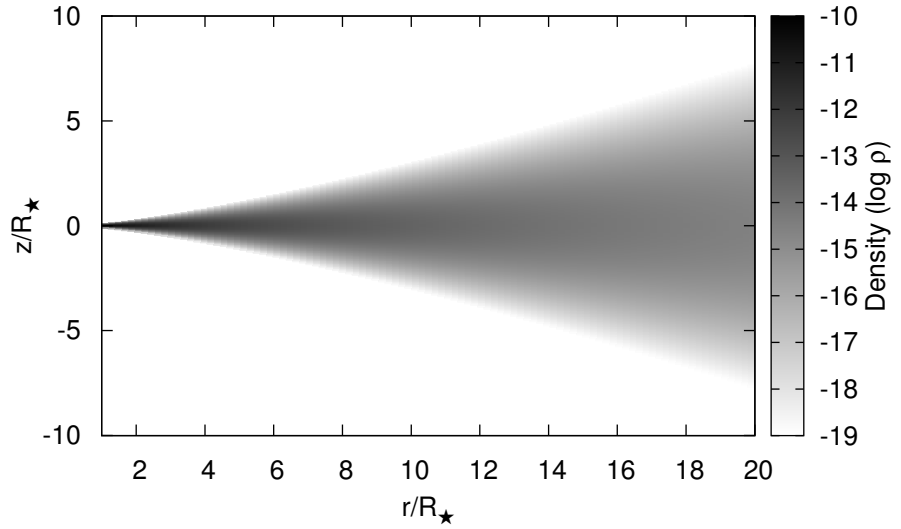

Figure 2.1: Density structure of a typical Be star disk with a base density of $\rho_0 = 10^{-10}$ g cm^{-3} and a fall off power law of $n = 3.5$, following Equation (2.1). The radial (r) and vertical (z) positions are expressed in units of stellar radii ($R_\star$) while the grayscale is in units of log(ρ).

2.3.2 Geometry of Disk Models

Two basic disk shapes are used as models to describe the disks of Be stars in this investigation. For simplicity, both models assume no irregularities in the disk, meaning that we have an azimuthal symmetry (axisymmetric disks) and a symmetry above and below the plane of the disk (longitudinal symmetry).

The first model consists very simply of a disk whose scale height increases linearly with radius, leading to a wedge geometry when seen as a cross-section, similar to the one proposed by Waters (1986). The disk is truncated at a certain radius R greater than the stellar radius $R_\star$, and the rate of vertical increase is defined by the opening half-angle parameter (α) which is tied to the shape of the disk. For simplicity, it is also assumed the disk is completely opaque inside the wedge. Figure 2.2 shows a cross-section of this model.

The projected axis ratio (q) for this model is a function of two parameters; α and the inclination angle i. Considering this wedge shape disk model truncated at R, with an opening half-angle α and is observed at i. To the observer, the projected length of the axis perpendicular to the plane of the inclination (per-

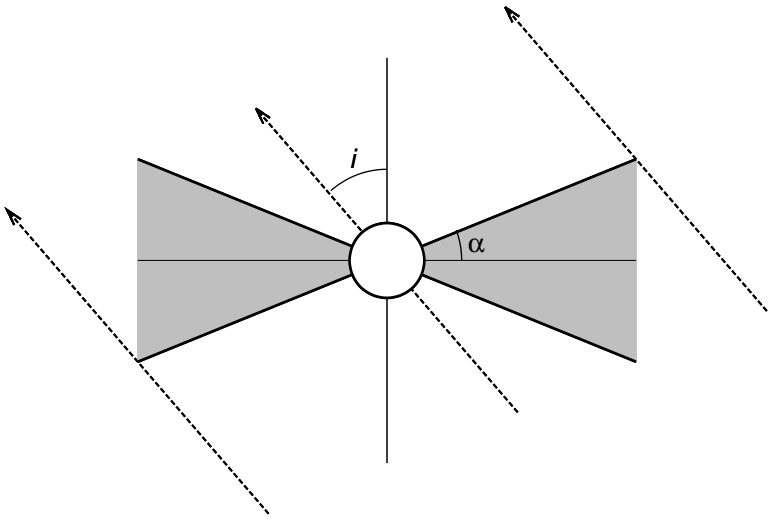

Figure 2.2: Cross-sectional view of the wedge shape disk model. The grey area represents the material of the disk. The dashed arrows point toward the line of sight of the observer.

pendicular to the page in Figure 2.2) will not be affected by the inclination, and will simply be the length of the equatorial disk,[b]

$$L_1 = 2R. \tag{2.3}$$

The projected length of the axis in the plane of the inclination (the cross-section depicted in Figure 2.2), however, will be the most affected by the inclination angle. As Figure 2.2 shows, the projected length of this axis is along the plane of the sky between the lower edge of the disk facing toward the observer and the upper edge of the disk, facing away from the observer. Its measured length, for inclinations between $i = 0°$ and $i = 90°$, is given by

$$L_2 = 2R\frac{\cos(i-\alpha)}{\cos(\alpha)}. \tag{2.4}$$

The ratio of L_1 and L_2 two is therefore our theoretical projected axis ratio and

[b]This is of course not the angular dimension, as we did not scale for distance. However, for the purpose of this work, we are only interested in the ratio of the axes.

is given by

$$q'(i,\alpha) = \frac{\cos(i-\alpha)}{\cos(\alpha)}. \tag{2.5}$$

Note that the dependence on the R is gone, leaving only α and i as variables. To ensure that the ratio is always between 0 and 1 (minor axis over major axis) the equation

$$q(i,\alpha) = 1 - |1 - q'(i,\alpha)| \tag{2.6}$$

is used.

One advantage of this model is that our axis ratio calculations depend only on these two parameters. However, the shape of this model is very simplistic, and does not take into account the density and thermal structure nor the optical thickness of the disk, all of which play a role in the emission processes.

For the second model, we chose a shape that is more related to the density structure of Be star disk, as predicted by the viscous disk model. As mentioned above, the emission is related to disk density. We therefore decided to base our model on the shape of the equidensity (ED) regions of the disk; that is, the shape of the regions where the density is equal to a specified value. Once again, we did not take into account the thermal structure, assuming therefore that we have an isothermal disk. By keeping ρ constant, Equation (2.1) becomes an implicit function of r and z:

$$\wp = r^{-n} \exp\left[-\frac{1}{2}\left(\frac{vz}{r^{1.5}}\right)^2\right], \tag{2.7}$$

where $\wp = \rho/\rho_0$ is the ratio of the density of the region versus the density at base of the disk, and v is the $V_{\rm Kep}$ over the c_s ratio. These two parameters, along with n are the physical parameters of this model. Isolating z from Equation (2.7) gives the relationship between z and r:

$$z^2 = -\frac{2r^3}{v^2}\ln(\wp r^n), \tag{2.8}$$

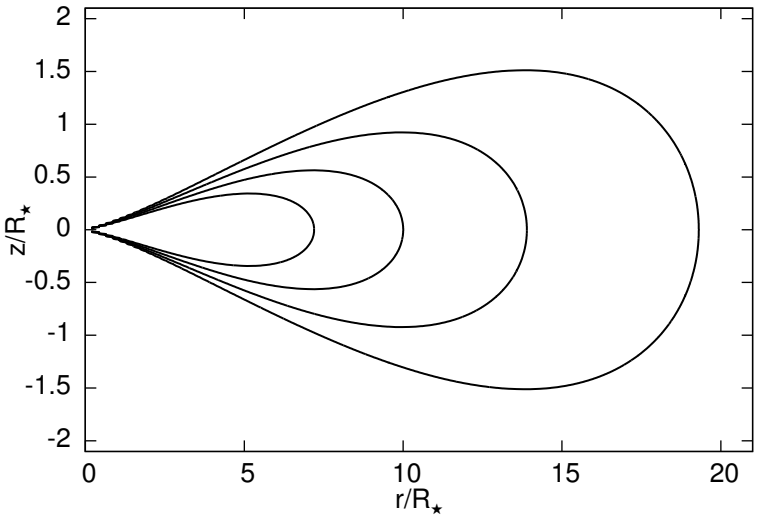

Figure 2.3: Cross-sectional view of the equidensity (ED) disk model for different density ratios ($\wp$). From the smallest shape to the biggest, the $\wp$ values are $10^{-3.0}$, $10^{-3.5}$, $10^{-4.0}$, and $10^{-4.5}$.

or,

$$z(r) = \pm \frac{\sqrt{-2r^3 \ln(\wp r^n)}}{v}. \tag{2.9}$$

Figure 2.3 shows various ED regions for different values of $\wp$, using the same disk parameters as Figure 2.1.

Equation (2.9), however, is a rather complex function, the complexity of which increases dramatically when taking its derivative with respect to r (which, as discussed later, is required to calculate the projected axis ratio). We therefore decided to use a simpler function that can reproduce ED shape given by Equation (2.9). This function is described as follows:

$$z^2 = ar^2(1 - br^2), \tag{2.10}$$

and the resulting shape is called a lemniscate, where a and b are its shape parameters. Equation (2.10) can be rewritten as a function by isolating z:

$$z(r) = \pm r\sqrt{a - abr^2}. \tag{2.11}$$

In order to best reproduce the ED profile with Equation (2.10), the shape

parameters a and b have been associated with the three physical parameters of Equation (2.7), namely $\wp$, n, and v. Let's define $r_{\max}$ and $z_{\max}$ as the maximum radial and vertical extent, respectively, of our shape, and r_z such that $z(r_z) = z_{\max}$, i.e. the radial position where the vertical extent is maximum. The ED and lemniscate shapes are differentiated by the use of the superscripts E and L, respectively. As seen in Figure 2.3, $z = 0$ at $r_{\max}$. Setting z to 0 in Equations (2.9) and (2.11), and solving for r gives a maximum radial position for both shapes [c]:

$$r^E_{\max} = \wp^{-1/n}, \tag{2.12}$$

$$r^L_{\max} = b^{-1/2}. \tag{2.13}$$

Equating $r^E_{\max}$ to $r^L_{\max}$ gives the following expression for b:

$$b = \wp^{2/n}. \tag{2.14}$$

Equation 2.14 shows that the parameter b and by extension $\wp$ and n are the only parameters responsible for the horizontal extent of the disk.

The maximum z extent will occur where the first derivative of z, with respect to r, is 0. Therefore, r_z can be determined by setting $\mathrm{d}z/\mathrm{d}r = 0$ and solving for r. We note here that, as the maxima of z^2 occurs at the same radial position as z, $\mathrm{d}z^2/\mathrm{d}r = 0$ was used instead to simplify the expressions. Applying this procedure to Equations (2.8) (for the ED shape) and (2.10) (for the lemniscate shape) yields

$$\begin{aligned} r^E_z &= \mathrm{e}^{-1/3}\wp^{-1/n} \\ &\approx 0.717 r^E_{\max}, \end{aligned} \tag{2.15}$$

$$\begin{aligned} r^L_z &= 2^{-1/2} b^{-1/2} \\ &\approx 0.707 r^L_{\max}, \end{aligned} \tag{2.16}$$

respectively. We notice that, in both cases, the ratio of r_z over $r_{\max}$ is a con-

[c] Multiple solutions exists for Equation (2.11) but are rejected as only the maximum positive value is sought.

stant value, without any dependence on the shape parameters. The fact that these constants differ for each shape indicates that it is impossible to match both $r_{\max}$ and r_z at the same time. Luckily, these constants differ very little from one another (less than 1.5%), therefore the peaks can be said to be approximately at the same position.

An expression for $z^2_{\max}$ can now be developed for both shapes by inserting Equations (2.15) and (2.16) into Equations (2.8) and (2.10), respectively,

$$\left(z^E_{\max}\right)^2 = \frac{2}{3e}\frac{n}{v^2 P^{3/n}}, \tag{2.17}$$

$$\left(z^L_{\max}\right)^2 = \frac{a}{4b}. \tag{2.18}$$

Finally, the shape parameter a can be determined by setting $(z^E_{\max})^2 = (z^L_{\max})^2$ and substituting the expression for b from Equation (2.14):

$$\begin{aligned} a &= \frac{8}{3e}\frac{n}{v^2 P^{1/n}} \\ &\approx \frac{n}{v^2 P^{1/n}}. \end{aligned} \tag{2.19}$$

Figure 2.4 shows the ED curve as defined by the viscous disk model (solid line) and the lemniscate curve (dashed line), both using the same physical parameters (n, $\wp$, and v). We see that the lemniscate curve reproduces the ED curve well at the outer edge, that is for $r \geq r_z$, but not so well for $r < r_z$. This, however, is unimportant for the purposes of this work as only the outer region is needed to calculate the projected axis ratio, as will be demonstrated below.

To calculate the projected axis ratio, we must first determine the length of the major and minor axes for any i. To simplify things, we will only consider the "half-length" instead of the full length, as the disk model is assumed to be axisymmetric. We will also only consider i values between 0° and 90°, again because of the symmetry of the disk. Figure 2.5 shows a cross-section of our model disk. The dashed lines represent the lines of sight of an observer viewing the disk at an inclination angle i.

When projected onto the plane of the sky, from the point of view of the ob-

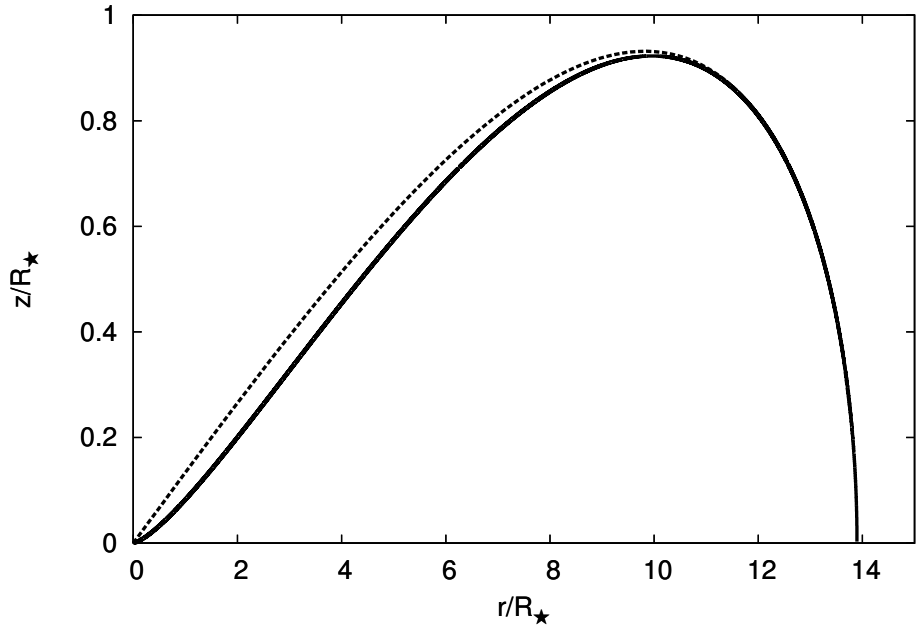

Figure 2.4: Comparison of the equidensity shapes from the density equation (solid line) and the lemniscate equation (dashed line).

server, the extent of the major axis is equal to the dimension of the disk perpendicular to the inclination plane (perpendicular to the page in Figure 2.5), which in our case is the radius of the disk. This radius can easily be obtained from Equation (2.10) by setting $z = 0$:

$$\begin{aligned} L_{\text{major}} = r_{\max} &= b^{-1/2} \\ &= \wp^{-1/n}. \end{aligned} \tag{2.20}$$

The extent of the minor axis is the projected dimension of the component of the disk in the inclination plane (plane of the page in Figure 2.5). Therefore, the dimension of the minor axis is the projection of the line segment $\overline{OT}$ (point T being the point at which the line of sight intersects the disk tangentially) on the plane of the sky, which corresponds to $\left|\overline{OL}\right|$ in Figure 2.5. It is easy to show that $\left|\overline{OL}\right|$ can be obtained from $\left|\overline{OX}\right|$ or $\left|\overline{OY}\right|$ by simple trigonometry. To obtain these points, we must first determine the position of point T.

As mentioned earlier, T is the point on the curve whose slope corresponds to

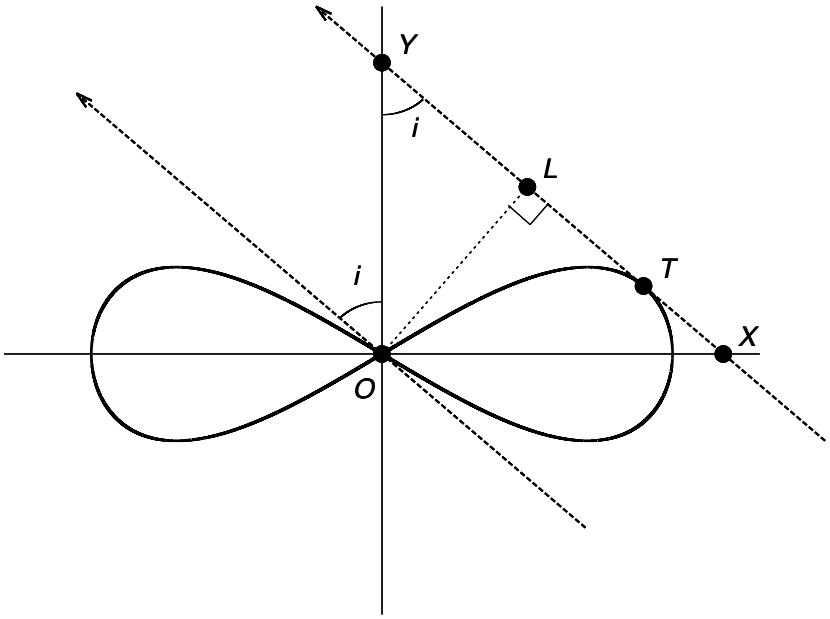

Figure 2.5: Cross-sectional view of the equidensity disk model. The dashed arrows point toward the line of sight of the observer while the dotted line represents the projected size of the minor axis.

the line of sight, in other words where $\frac{dz(r)}{dr} = \cot(i)$. The radial and vertical coordinates at point T will be referred to as r_T and z_T, respectively. Setting the derivative of Equation (2.11) to $\cot(i)$ and solving for r gives us the r_T coordinate:

$$r_T = \sqrt{\frac{4a - \cot^2(i) + \sqrt{8a\cot^2(i) + \cot^4(i)}}{8ab}}. \tag{2.21}$$

We can then obtain z_T by substituting Equation (2.21) back into Equation (2.11):

$$z_T = r_T\sqrt{a - abr_T^2}. \tag{2.22}$$

Either $\left|\overline{OX}\right|$ or $\left|\overline{OY}\right|$ can now be obtained from the linear equation using r_T and z_T as coordinates and $-\cot(i)$ as the slope:

$$\begin{aligned} \left|\overline{OX}\right| &= r_T + z_T\tan(i), \\ \left|\overline{OY}\right| &= r_T\cot(i) + z_T. \end{aligned} \tag{2.23}$$

The minor axis can now be calculated using simple trigonometry and either of the above equations:

$$\begin{aligned} L_{\text{minor}} &= \left|\overline{OL}\right| \\ &= r_T\ \cos(i) + z_T\ \sin(i). \end{aligned} \tag{2.24}$$

Finally, the projected axis ratio can be calculated by taking the ratio $L_{\text{minor}}/L_{\text{major}}$:

$$\begin{aligned} \frac{L_{\text{minor}}}{L_{\text{major}}} &= \frac{r_T\ \cos(i) + z_T\ \sin(i)}{\wp^{-1/n}} \\ &= \frac{r_T\ \cos(i) + z_T\ \sin(i)}{b^{-1/2}}. \end{aligned} \tag{2.25}$$

Although this last equation appears to depend on both parameters a and b, it in fact only depends on the former. This can easily be shown by considering that both r_T and z_T are proportional to $b^{-1/2}$. In other words the projected axis ratio does not depend on the actual size of the disk, leaving a as the fundamental shape parameter. For this model we chose to use χ, defined as the

ratio z_{max}/r_{max}, as the shape parameter of this model. By combining Equations (2.16) and (2.18) it can easily be shown that the ratio z_{max}/r_{max} depends only on a and that it can therefore be used as a fundamental shape parameter. For simplicity, we shall call this parameter χ:

$$\begin{aligned} \chi &\equiv \frac{z_{max}}{r_{max}} = \frac{1}{2}\sqrt{a} \\ &= \frac{1}{2v}\sqrt{\frac{n}{\wp^{1/n}}}. \end{aligned} \tag{2.26}$$

The advantage of this model is that the shape used is closely related to the viscous disk model, which as already discussed is widely accepted as the mechanism responsible for disk growth and therefore dictates the shape of the density distribution of Be disks.

2.3.3 Distribution of Shape Parameters

As discussed above, each model has a set of parameters that define the shape of the disk. Our goal is to find which shape parameter value, or range of values, best reproduces the observed axis ratios.

The inclination parameter i is present in both models. Assuming no preferred inclination in our population of stars, we distribute our angles using $i = \cos^{-1}(u)$, where u is selected from a uniform distribution such as $u \in [0, 1]$, as was done by Cranmer (2005). As we assume the disk is symmetric in both models, the range of i is limited to $[0,\pi/2]$.

A β-distribution function was used to study the distribution of shape parameters. This distribution was chosen because it is well defined and well constrained within a finite interval. Its functional form is:

$$\Psi_\beta(x; A, B) = \frac{x^{A-1}(1-x)^{B-1}}{\beta(A, B)}, \tag{2.27}$$

where x is a continuous variable between 0 and 1, A and B are the shape pa-

rameters and $\beta(A, B)$ is the Beta function:

$$\beta(A, B) = \int_0^1 t^{A-1}(1-t)^{B-1}\mathrm{d}t. \tag{2.28}$$

The shape parameters, A and B, affect the width of the distribution and their relative values affect the position of the peak. The greater B is compared to A, the closer the peak will be to the lower x values, and vice-versa. The distribution will be centred if $A = B$. Higher values of either parameter results in a smaller deviation (thinner distribution). The β-distribution can also be parametrized in terms of the parameters μ and ν by using the following relations:

$$\begin{aligned} A &= \mu\nu, \\ B &= (1-\mu)\nu, \end{aligned} \tag{2.29}$$

where $0 \leq \mu \leq 1$ and $\nu > 0$. The parameter μ in this case represents the mean value of the distribution. The variance of the distribution can also be expressed as a function of these parameters:

$$\Psi_{var} = \frac{\mu(1-\mu)}{1+\nu}. \tag{2.30}$$

2.3.4 Ratio Simulations and Comparison with Observations

Sets of simulated axis ratios are generated using Monte Carlo techniques. Each set consists of 10^6 simulated projected axis ratios using a specific model (Section 2.3.2) whose shape parameters are chosen randomly for a specific distribution (Section 2.3.3). The parameters of the chosen distributions are varied systematically from set to set, allowing us to assess which distribution best reproduces the observations.

The observed ratios were grouped into sets according to the wavelength regime at which they were measured. The first set includes all measurements in the K-band, which includes 18 ratio measurements of 16 distinct stars. In an attempt to increase the amount of data points, all measurements taken in either the K-,

H-, or N-band (from now on referred to as KHN-band) were also grouped together. The reason for this grouping is that emission in these three bands are likely formed within similar volumes of the disk (Carciofi, 2011) and therefore α should be similar for all three bands. Adding the observations in the H- and N-band adds five measurements and one new star, for a total of 24 ratios for 17 stars. The third and final set consists of observations acquired over the Hα emission line (656.3 nm). This set contains 20 measurements, which includes seven distinct stars.

As seen in Table 2.1 of Section 2.2 some stars have multiple ratio measurements and in some cases in the same wavelength regime. For this reason, a weighted average is used to reduce each of these multiple measurements to a single value. First, an inverse-variance weighting is applied to the measurements:

$$w'_j = \frac{1}{\sigma_j^2}, \tag{2.31}$$

where σ_j is the uncertainty of the measurement. The weights for each individual star are then normalized in such a way that their sums equal 1.

The degree of agreement between the observed and simulated projected axis ratios is determined using the two-sample Kolmogorov-Smirnov (K-S) test. This test compares the cumulative distribution function of our samples, both observed and simulated, and determines whether the null hypothesis (i.e. that both samples come from the same distribution) can be rejected or not. It can also be used as a "goodness-of-fit" test to determine which distribution of simulated ratios best fit the observed distribution. The K-S statistic D is defined as the largest difference between the cumulative distribution functions (CDFs) of the two samples being compared, $F_1(x)$ and $F_2(x)$ (see Press, 2007, for further details):

$$D = \sup_x |F_1(x) - F_2(x)|. \tag{2.32}$$

The significance level of D can be estimated by the following function:

$$P_D \approx Q_{\rm KS}(\lambda) = 2\sum_{j=1}^{\infty}(-1)^{j-1}{\rm e}^{-2j^2\lambda^2}, \tag{2.33}$$

where

$$\lambda = D\left(\sqrt{N} + 0.12 + 0.11/\sqrt{N}\right), \tag{2.34}$$

and N is the effective number of data points, derived from the number of data points in each sample (n_1 and n_2),

$$N = \frac{n_1 n_2}{n_1 + n_2}. \tag{2.35}$$

The null hypothesis can be rejected (i.e. the samples do not come from the same distribution) if P_D is below the significance level α. For this work, we used a significance level of 10% ($\alpha = 0.1$).

2.4 Results

2.4.1 Wedge Model

We first compared the observed ratios with the simulated ratios obtained using single values of α, that is no distribution was used. Figure 2.6 shows the results of the K-S test between the observed and simulated ratios as a function of α, for all three observational sets; K-band (solid), KHN-band (dash), and Hα line (dot). The grey line represents the 90% confidence limit for this test.

For the K- and KHN-band, the model best reproduces the observations when small α values are used, that is for α of 0.15° and 0.32°, respectively. After these maxima, the probability goes down exponentially, reaching the confidence limit at 9.21° for the K-band and 7.94° for the KHN-band. For Hα observations, the model best matches the observations at $\alpha = 3.7°$, a value higher than the α found for the other two sets of observations. We also have a greater range of α within the confidence limit, which is reached at 28°.

Although these single-α simulations give us a good idea of the opening angle of our disks based on this simple assumed geometry, it is more probable that the opening angle of these disks are not all the same, but rather distributed over a certain range of angles. In order to take this into account, we repeated our simulations with α values randomly picked following a β-distribution (see Section 2.3.3) with different pairs of distribution parameters, μ and ν, for each set

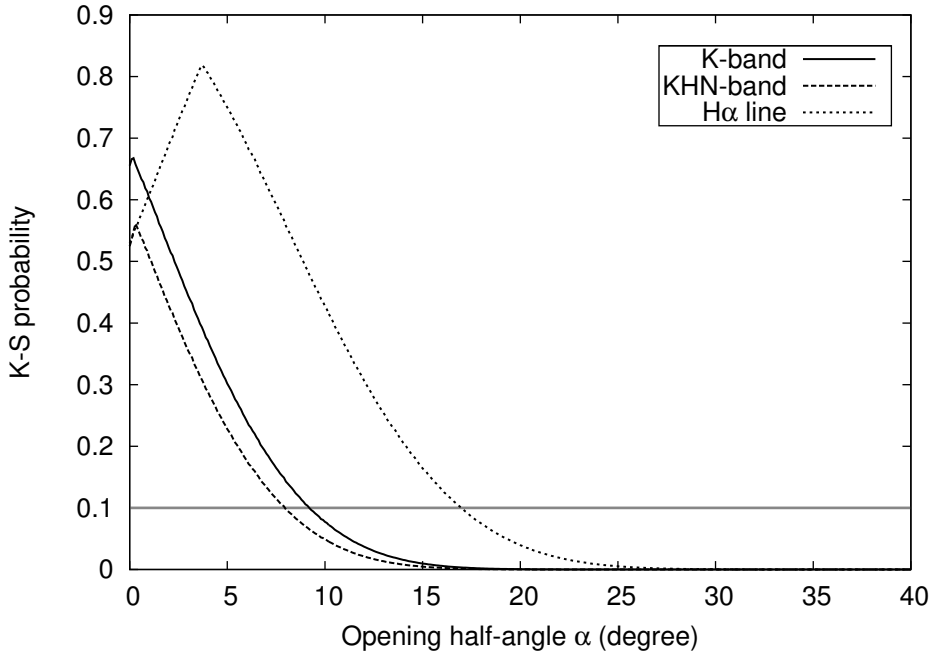

Figure 2.6: K-S test results for simulated data with single α values for measurements in the K-band (solid line), the KHN-band (dashed line), and the Hα line (dotted line). The grey line represents the 90% confidence limit of the test.

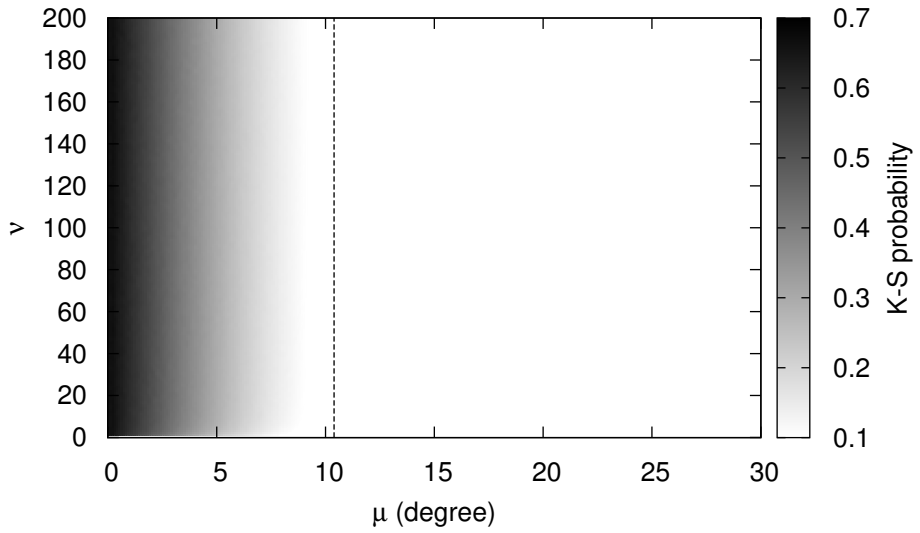

Figure 2.7: Results of the K-S comparison test between the K-band set and the β-distributed simulation, using the wedge model, as a function of the μ and ν parameters. The dashed line shows the contour of the 90% confidence limit.

of simulated ratios. The domain of the β-distribution, which is typically [0,1], was extended to match the range of α. Once again, these simulated sets were compared with the observed ratios.

Figures 2.7, 2.8, and 2.9 show results of the K-S test for the K-band, KHN-band, and Hα sets, respectively, as a function of the beta distribution parameters μ and ν. The dash line shows the contour of the 90% confidence limit.

All three figures show a similar trend. The results of the K-S test seems to vary with μ but not, or at least not significantly, with ν. This would indicate that the goodness of the fit depends almost entirely on the mean value of distribution of α but not its variance. For both the K- and KHN-band, the highest values of the K-S test results are located at low μ values, corresponding to β-distributions greatly skewed toward low α values and therefore thinner disks. For the Hα set, the best fits appear at somewhat higher μ values, which correspond to a larger α (thicker disk). Interestingly, the highest K-S test results for all three sets occur at same mean α (μ) values as the results of the previous test; 0.15° for the K-band set, 0.32° for the KHN-band set, and 3.7° of the Hα set.

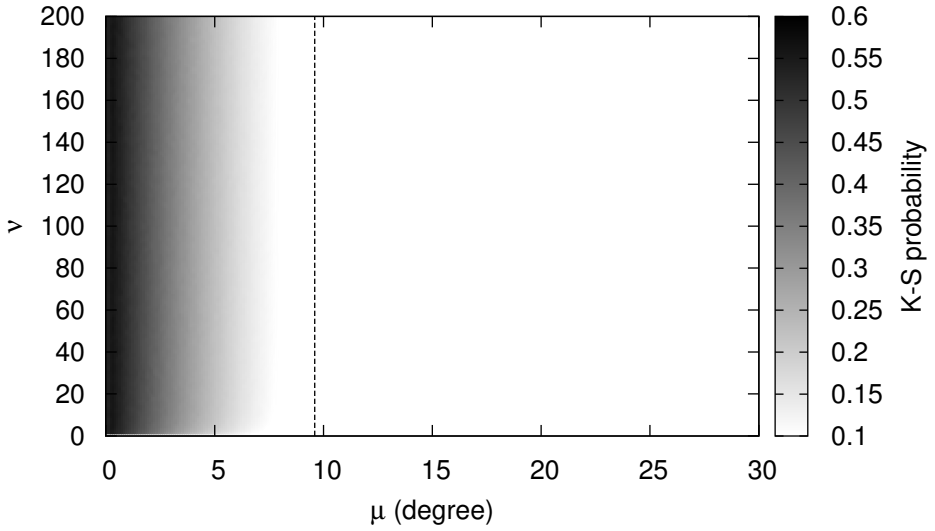

Figure 2.8: Same as Figure 2.7 except for the KHN-band set.

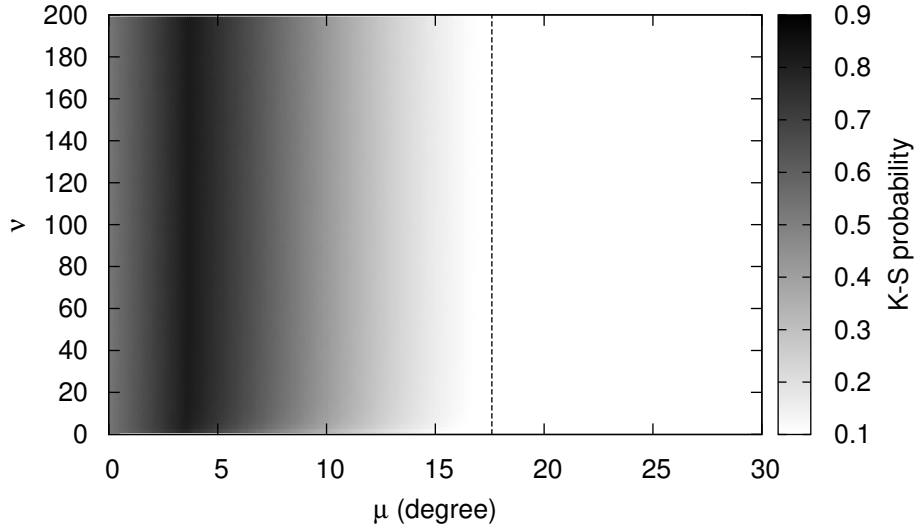

Figure 2.9: Same as Figure 2.7 except for the Hα set.

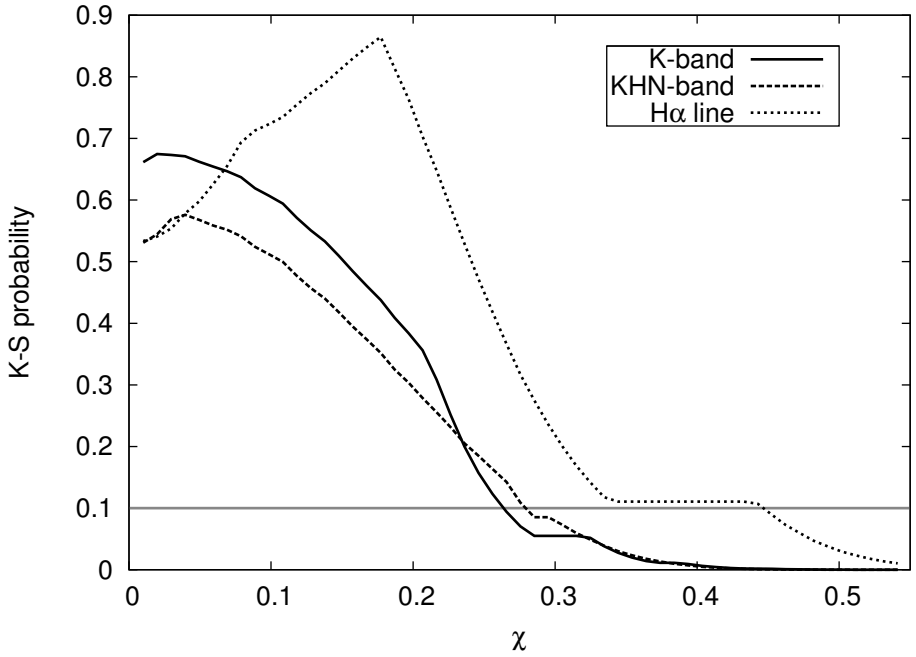

Figure 2.10: K-S test results for simulated data with single χ values distribution for measurements in the K-band (solid line), the KHN-band (dashed line), and the Hα line (dotted line). The grey line represents the 90% confidence limit of the test.

The difference in the distributions of α from the K- and KHN-band sets, and the Hα set is expected. Carciofi (2011), have estimated that emission in the K-band, as well as in the H- and N-band, are formed in a much smaller volume of the disk near the star than the Hα emission. Moreover, as discussed in Section 2.3.1, the viscous disk model predicts a flaring of the disk, meaning that we expect the effective opening angle to be greater farther away from the star.

2.4.2 Equidensity Model

Like the previous model, we start by comparing the observed ratios with simulated ratios obtained using single values for our shape parameters, which for this model is χ. Figure 2.10 shows the results of the K-S test between the observed and simulated ratios as a function of χ. Once again, the K-band, KHN-band, and Hα line sets are represented by the solid, dashed, and dotted lines, respectively, while the grey line represents the 90% confidence limit.

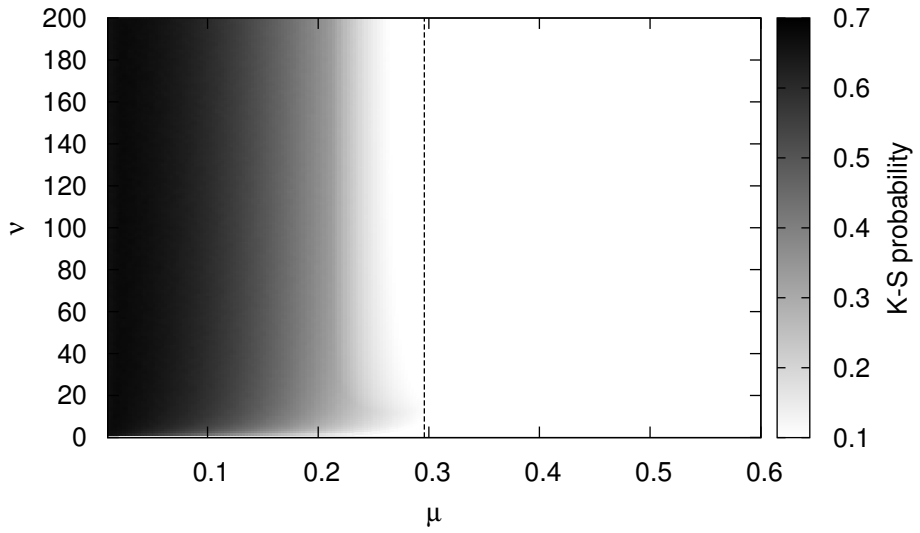

Figure 2.11: Results of the K-S comparison test between the K-band set and the β-distributed simulation, using the ED model, as a function of the μ and ν parameters. The dashed line shows the contour of the 90% confidence limit.

For the K- and KHN-band, the best fit occurs at small values of χ, that is 0.024 and 0.037, respectively, while the best fit for the Hα set occurs for $\chi = 0.18$, a value higher than the previous two. The range of χ including the confidence limit is also smaller for the K- and KHN-band (from 0 to 0.26 and 0 to 0.28, respectively) than Hα (from 0 to 0.45). One notable feature is the small plateaus found near the end of each curve. These features are a result of the absence, in our samples, of observed axis ratio ranging somewhere between 0.25 and 0.45 depending on the observation set, which causes the maximum deviation between the observed and simulated CDFs to take similar values for a certain range of χ values.

For the next step χ was varied over a β-distribution. The results of the K-S test using the equidensity model are presented in Figures 2.11, 2.12, and 2.13 for the K-band, KHN-band, and Hα sets, respectively, in the same fashion as Figures 2.7, 2.8, and 2.9 in the previous section.

Similarly to the results presented in the previous section for the wedge model, the K-S test results vary primarily with μ and are mostly independent of ν. An exception to this can however be seen in the lower part of Figure 2.9 for

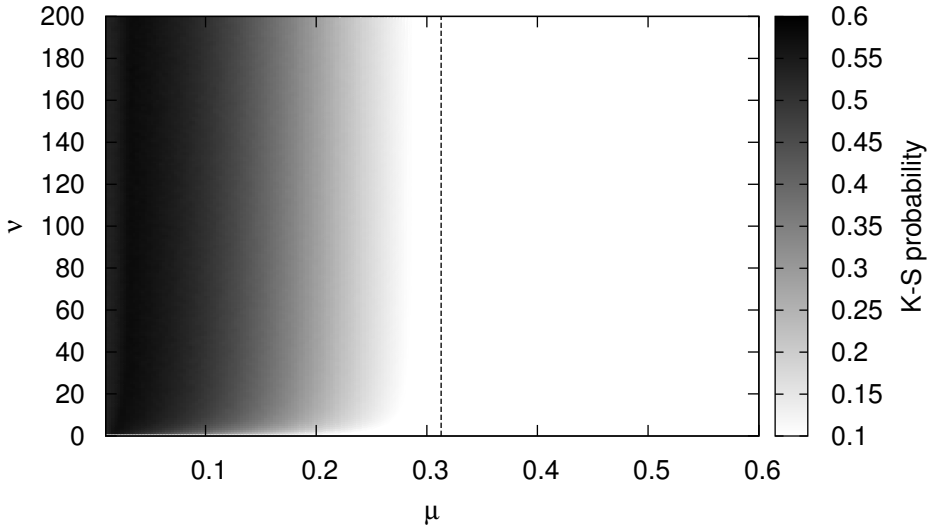

Figure 2.12: Same as Figure 2.11 but for KHN-band set.

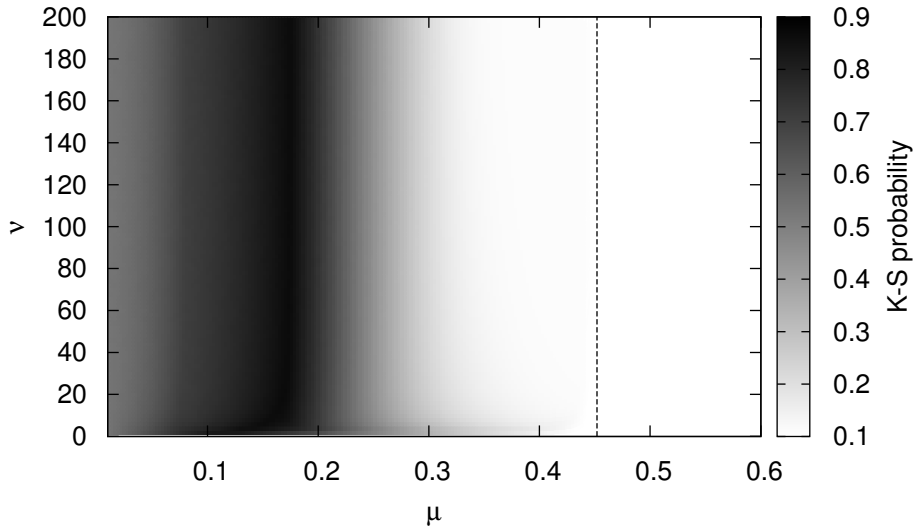

Figure 2.13: Same as Figure 2.11 but for Hα set.

$\nu < 10$. Once again we see that the model better fits the K- and KHN-band observations when lower χ are used, while the Hα line observations are best fit with a higher χ. These results, as well as the results of the single χ simulation, agree with the results of the previous model. Assuming constant n and v values, Equation (2.26) shows that lower χ's corresponds to a higher density ratio ($\wp$). As we can see from the density structure of the viscous disk (Figure 2.3), ED regions with lower densities extend further away from the star and appear more "puffed up" vertically than regions of higher density. This means that these low density ED regions have a higher effective opening angle. Therefore, according to the equidensity model results, Hα line comes from regions with a greater vertical extent, and therefore greater effective opening angles, than the KHN-band emitting regions.

To better compare the results of both models, we expressed the results of the ED model in terms of the effective opening half-angle, α_{eff}. We define α_{eff} to be the angle between the base of the disk and the line going from the origin to the highest vertical point. The coordinates of this point are r_{z} and z_{max}, as defined in Equations (2.16) and (2.18), respectively. The values of α_{eff} can then be obtained using simple trigonometry;

$$\alpha_{\text{eff}} = \arctan\left(\frac{z_{\text{max}}}{r_{\text{z}}}\right). \tag{2.36}$$

Furthermore, Equation (2.16) tells us that we can express r_z as a function of r_{max}, allowing us to rewrite Equation (2.36) in terms of χ;

$$\begin{aligned} \alpha_{\text{eff}} &= \arctan\left(\frac{z_{\text{max}}}{2^{-1/2} r_{\text{max}}}\right) \\ &= \arctan\left(\sqrt{2}\chi\right). \end{aligned} \tag{2.37}$$

Using Equation (2.37) and the results for the ED model presented above, the α_{eff} for the K-band, KHN-band, and Hα line set are estimated ata 1.9°, 3.0°, and 14°, respectively, with a confidence interval ranging from 0° to 20° from the K-band, 0° to 22° for the KHN-band, and 0° to 32° for Hα. As we can see

the ED model predicts larger opening angles than the wedge model; four times greater for Hα and up to an order of magnitude greater for the K- and KHN-band sets.

Using the results of the ED model, the radial extent of each emitting region can also be estimated. By combining Equations (2.20) and (2.26), we can express the radial extent (r_{max}) as a function of χ:

$$r_{\max} = \frac{4\chi^2 v^2}{n}. \tag{2.38}$$

We see that the maximum extent of any region defined by χ is dependent on the parameter n and v, meaning r_{max} is also dependent of the stellar and disk parameters as well as its rotational velocity. To compare with previous work in the literature, we decided to adopt a value of 3.5 for n (see Section 2.3) and the stellar parameters of a B1V star (obtained from Cox, 2000) rotating at 92% of critical angular velocity, the same parameters used by Carciofi (2011). Using these parameters, v is calculated to be 50.4.

For the K-band and KHN-band set, the maximum extent is estimated to be about 2 to 4 stellar radii. This result closely matches the results of Carciofi (2011), who found the K-band emission is contained within 6 stellar radii[d]. For the Hα line set, the estimated extent is between 80 and 90 stellar radii, which is slightly larger than the 50 to 60 stellar radii determined by Carciofi (2011). One possible cause for these differences could be attributed to a change in the power law n. Although the viscous disk model presented above assumes that density structure of the disk is controlled by a constant power law of n, some authors have suggested that n might not be constant throughout the disk, but could vary with radius (Carciofi et al., 2008; Zorec et al., 2007). We note, for example, that increasing the value of n will result in a smaller extent closer to that determined by Carciofi (2011).

[d]See figure 1 of Carciofi (2011).

2.5 Discussion and conclusion

For the first time, the geometry of Be star disks were inferred from the deprojection of axis ratio measurements. A total of 49 ratio measurements from 20 distinct stellar sources collected from the literature were used. These ratios were measured with interferometry in either the K-, H- or N-band, or over the Hα emission line. These observations were compared to simulated axis ratios calculated from two disk models; the wedge model, a simple model characterised by an opening half-angle similar to the one proposed by Waters (1986), and the equidensity model, whose shape is derived from the viscous disk model. A Monte Carlo technique was employed to generate a large number of simulated ratios, which were compared to the observation by applying Bayesian statistics in order to infer which model best reproduces these observations.

For the emission regions in the KHN-band, we found that our models can best reproduce the observations with opening half-angles of 0.15° to 0.32° (wedge model) and 1.9° to 3.0° (equidensity model) with a confidence interval ranging up to 9.2° and 22°, respectively. Angles of 3.7° to 14° were found to best reproduce the observation in Hα with confidence interval ranging up to 28° for the wedge model and 32° for the equidensity model. We note that the best fit results are in close agreement with the the opening angles of 2.5°, 5°, and 13° found by Porter (1996), Wood et al. (1997), and Hanuschik et al. (1996), respectively, and are below the upper limit of 20° determined by Quirrenbach et al., 1997.

Opening half-angles were also found to be systematically smaller for the KHN-band emission region than the Hα region. This also agree with predictions, as the viscous disk model predicts that the scale height of Be star disk increases with distance from the star (Bjorkman, 1997). The greater opening angle for Hα therefore suggests that its emission region extends to greater distances than the emission region of the KHN-band, which is consistent with the findings of Gies et al. (2007) and Carciofi (2011).

The extent of the emitting regions for a model star were also estimated, from the results of the ED model, and compared with the results of Carciofi (2011).

The extent of the KHN-band regions were found to be constrained to a small area close to the star, within 2 to 4 stellar radii. The Hα emitting region on the other hand was found to have a much greater area, ranging from 80 to 95 stellar radii. Again, these results agree well with the findings of Carciofi (2011), who estimated the emitting regions of the K-band and Hα line to be $\sim$5 to 6 and $\sim$50 to 60 stellar radii, respectively.

In this study, a standard distribution of inclination angles (as described in Section 2.3.3) was assumed, without accounting for observational limitations. Due to the limits in resolution power of interferometric measurements, the minor axis of stars seen at high inclination angles (close to equator-on) are less likely to be resolved. This implies that stars with small axis ratios (seen at high inclination) are expected to be under-represented compared to other stars in the sample and that the number of high-inclination stars, and consequently the number of small ratios, in our simulations may be systematically overestimated.

Our results could also be affected by the visibility models applied to the interferometric observations. As mentioned in Section 2.2, theoretical models of the visibility of Be star/disk systems are applied to observations in order to obtain axis ratios. This means that assumptions have already been made on the general shape of the disk and therefore, the results of this study depend on the interferometric models used.

Finally we note that our models do not take into account the optical thickness of the disk and its effects on the projected axis ratios. Since photons emitted at different locations in the disk have to go through different amounts of material before escaping, light coming from the same equidensity region may not have the same intensity once it reaches us. This could have an effect on our results. To test the significance of this effect, we calculated the optical depth of a disk based on simple isothermal models. For inclinations of 70° or lower, we found that the ratios calculated with optical depth effects differed by no more then 0.02 from the ratios calculated by ignoring optical depth effects, a difference smaller than the uncertainty of the majority of the observations (see Table 2.1). The effect is more significant for the equator-on case, where we found differences of up to 0.1 between ratios calculated with and without op-

tical depths. Although this difference is larger than seen for lower inclinations, it is still within the order of magnitude of most of the uncertainties in the observed axis ratios.

In conclusion, we found that the results of our deprojections are consistent with the current understanding of Be star disks. The opening angles were found to be small, supporting the findings of Porter (1996), Wood et al. (1997), and Hanuschik et al. (1996). We were also able to confirm that Hα line emission is formed in a much larger volume of the disk than emission from the KHN-band, as predicted by Carciofi (2011). We can therefore conclude that the deprojection method presented in this work can be a very useful tool to obtain information about the size and geometry of Be star disk based on measured axis ratios.

References

Behr, A. (1959). *Veroeffentlichungen der Universitaets-Sternwarte zu Goettingen* 7, pp. 175–180.

Bjorkman, J. E. (1997). *Stellar Atmospheres: Theory and Observations*. Ed. by J. P. De Greve, R. Blomme, and H. Hensberge. Vol. 497. Lecture Notes in Physics, Berlin Springer Verlag, p. 239. DOI: 10.1007/BFb0113487.

Carciofi, A. C. (2011). *IAU Symposium*. Ed. by C. Neiner, G. Wade, G. Meynet, et al. Vol. 272. IAU Symposium, pp. 325–336. DOI: 10.1017/S1743921311010738.

Carciofi, A. C. and Bjorkman, J. E. (2008). ApJ 684, pp. 1374–1383. DOI: 10.1086/589875.

Cox, A. N. (2000).

Cranmer, S. R. (2005). ApJ 634, pp. 585–601. DOI: 10.1086/491696.

Delaa, O., Stee, P., Meilland, A., et al. (2011). A&A 529, A87, A87. DOI: 10.1051/0004-6361/201015639.

Dougherty, S. M. and Taylor, A. R. (1992). Nature 359, pp. 808–810. DOI: 10.1038/359808a0.

Fall, S. M. and Frenk, C. S. (1983). AJ 88, pp. 1626–1632. DOI: 10.1086/113452.

Gies, D. R., Bagnuolo Jr., W. G., Baines, E. K., et al. (2007). ApJ 654, pp. 527–543. DOI: 10.1086/509144.

Grzenia, B. J., Tycner, C., Jones, C. E., et al. (2013). AJ 145, 141, p. 141. DOI: 10.1088/0004-6256/145/5/141.

Hanuschik, R. W., Hummel, W., Sutorius, E., et al. (1996). A&AS 116, pp. 309–358.

Haubois, X., Carciofi, A. C., Okazaki, A. T., et al. (2011). *IAU Symposium*. Ed. by C. Neiner, G. Wade, G. Meynet, et al. Vol. 272. IAU Symposium, pp. 396–397. DOI: 10.1017/S1743921311010891.

Jones, C. E., Basu, S., and Dubinski, J. (2001). ApJ 551, pp. 387–393. DOI: 10.1086/320093.

Jones, C. E. and Basu, S. (2002). ApJ 569, pp. 280–287. DOI: 10.1086/339230.

Jones, C. E., Tycner, C., Sigut, T. A. A., et al. (2008). ApJ 687, pp. 598–607. DOI: 10.1086/591726.

Kraus, S., Monnier, J. D., Che, X., et al. (2012). ApJ 744, 19, p. 19. DOI: 10.1088/0004-637X/744/1/19.

Lambas, D. G., Maddox, S. J., and Loveday, J. (1992). MNRAS 258, pp. 404–414.

Lee, U., Osaki, Y., and Saio, H. (1991). MNRAS 250, pp. 432–437.

Meilland, A., Stee, P., Chesneau, O., et al. (2009). A&A 505, pp. 687–693. DOI: 10.1051/0004-6361/200911960.

Millan-Gabet, R., Monnier, J. D., Touhami, Y., et al. (2010). ApJ 723, pp. 544–549. DOI: 10.1088/0004-637X/723/1/544.

Okazaki, A. T. (2001). PASJ 53, pp. 119–125.

– (2007). *Active OB-Stars: Laboratories for Stellare and Circumstellar Physics*. Ed. by A. T. Okazaki, S. P. Owocki, and S. Stefl. Vol. 361. Astronomical Society of the Pacific Conference Series, p. 230.

Porter, J. M. (1996). MNRAS 280, pp. L31–L35.

– (1999). A&A 348, pp. 512–518.

Press, W.H. (2007). Cambridge University Press. ISBN: 9780521880688.

Quirrenbach, A. (1994). *Pulsation; Rotation; and Mass Loss in Early-Type Stars*. Ed. by L. A. Balona, H. F. Henrichs, and J. M. Le Contel. Vol. 162. IAU Symposium, p. 450.

Quirrenbach, A., Buscher, D. F., Mozurkewich, D., et al. (1994). A&A 283, pp. L13–L16.

Quirrenbach, A., Bjorkman, K. S., Bjorkman, J. E., et al. (1997). ApJ 479, p. 477. DOI: 10.1086/303854.

Ryden, B. S. (1996). ApJ 471, p. 822. DOI: 10.1086/178010.

Sandage, A., Freeman, K. C., and Stokes, N. R. (1970). ApJ 160, p. 831. DOI: 10.1086/150475.

Schaefer, G. H., Gies, D. R., Monnier, J. D., et al. (2010). AJ 140, pp. 1838–1849. DOI: 10.1088/0004-6256/140/6/1838.

Shakura, N. I. and Sunyaev, R. A. (1973). A&A 24, pp. 337–355.

Silaj, J., Jones, C. E., Tycner, C., et al. (2010). ApJS 187, pp. 228–250. DOI: 10.1088/0067-0049/187/1/228.

Smith, M. A., Lopes de Oliveira, R., Motch, C., et al. (2012). A&A 540, A53, A53. DOI: 10.1051/0004-6361/201118342.

Stee, P. (1995). Ap&SS 224, pp. 561–562. DOI: 10.1007/BF00667955.

Stee, P., Delaa, O., Monnier, J. D., et al. (2012). A&A 545, A59, A59. DOI: 10.1051/0004-6361/201219234.

Stee, P., Meilland, A., Bendjoya, P., et al. (2013). A&A 550, A65, A65. DOI: 10.1051/0004-6361/201220302.

Touhami, Y., Gies, D. R., Schaefer, G. H., et al. (2013). ApJ 768, 128, p. 128. DOI: 10.1088/0004-637X/768/2/128.

Tycner, C. (2011). *IAU Symposium*. Ed. by C. Neiner, G. Wade, G. Meynet, et al. Vol. 272. IAU Symposium, pp. 337–341. DOI: 10.1017/S174392131101074X.

Tycner, C., Hajian, A. R., Armstrong, J. T., et al. (2004). AJ 127, pp. 1194–1203. DOI: 10.1086/381068.

Tycner, C., Lester, J. B., Hajian, A. R., et al. (2005). ApJ 624, pp. 359–371. DOI: 10.1086/429126.

Tycner, C., Gilbreath, G. C., Zavala, R. T., et al. (2006). AJ 131, pp. 2710–2721. DOI: 10.1086/502679.

Tycner, C., Jones, C. E., Sigut, T. A. A., et al. (2008). ApJ 689, pp. 461–470. DOI: 10.1086/592097.

Waters, L. B. F. M. (1986). A&A 162, pp. 121–139.

Waters, L. B. F. M., Cote, J., and Lamers, H. J. G. L. M. (1987). A&A 185, pp. 206–224.

Wood, K., Bjorkman, K. S., and Bjorkman, J. E. (1997). ApJ 477, p. 926. DOI: 10.1086/303747.

Zorec, J., Arias, M. L., Cidale, L., et al. (2007). A&A 470, pp. 239–247. DOI: 10.1051/0004-6361:20066615.

3

Be Disks in Misaligned Binary Systems

3.1 Introduction

The B-emission or Be stars are predominantly characterized by emission in the Balmer lines and have been studied since they were first detected by Secchi (1867). In addition to the emission in the hydrogen lines, emission is often observed in singly or doubly ionized metals and is a direct result of radiative recombination in a disk-like distribution of gas. Other defining features include continuum excess in the infrared and visible, linear polarization and variability over a significant range in period. These features originate in a geometrically thin disk of material ejected from the rapidly rotating central star. During the time since Secchi's discovery, our understanding of these star/disk systems has steadily improved but there are a significant number of remaining puzzles. The current status of Be-star research has been recently reviewed by Rivinius et al. (2013).

In a pioneering paper, Shakura et al. (1973) investigated the transfer of angular momentum in disks surrounding black holes and in doing so established a framework for future studies of hydrodynamic disks. The review paper by

Pringle (1981) summarises the major properties of accretion disks including detailed discussion about the role of viscosity and emission processes. Since that time there have been a multitude of investigations that adopt and apply accretion theory to model astrophysical disks that surround a variety of different types of objects.

The same prescription originally developed for viscous accretion disks can be applied to study Be star disks except, in this case, the material is outward flowing. The viscous decretion disk (VDD) scenario for Be stars, originally adopted by Lee et al. (1991) assumes that angular momentum is transferred from the star to the disk via an unknown mechanism. His work was followed up by Okazaki (2001) who found that the outflow in the inner disk is subsonic and rotating in a Keplerian fashion, consistent with current findings about Be stars. The viscosity parameter is given by the usual $\alpha_{\rm SS}$ viscosity parameter and for Be stars is usually assumed to be in the range of 0.1 to 1 (see Lee et al., 1991). The VDD has been the focus of an increasing number of studies. For example, Martin et al. (2011) studied warping and precession of Be star disks and find that in non-coplanar binary systems the disk can become distorted and warped. Fu et al. (2015) studied oscillations, in particular the Kozai-Lidov mechanism, in hydrodynamic disks in binary systems by considering the effect of disk pressure and viscosity. They find that given sufficient time the disk becomes co-planar with the binary companion. Lubow et al. (2015) find that in misaligned systems the disk can be more extended in radial distance than a disk in a co-planar system. Despite the fact the focus of Fu et al. (2015) and Lubow et al. (2015) studies are about accretion disks, their work can help provide insight to the results presented in this investigation.

For the case of an isolated Be star, the central star supplies matter and angular momentum to the disk and is the primary energy input to the disk through its radiation field. The stellar wind potentially could ablate the disk material or help to constrain material to the equatorial regions especially in the inner parts of the disk (Okazaki, 2012). However, in a binary system the situation is more complex. In addition to tidally truncating the disk, the companion interacts with the disk through resonant torques which could cause the disk to warp

and/or precess (Kee et al., 2016; Okazaki, 2012) and these effects may complicate the density structure for the case of both aligned and misaligned disks.

The innermost disk is dominated by viscous torques so that isolated and binary systems may be similar in the inner regions (Okazaki, 2012). However, as explained by Okazaki et al. (2002), with increasing radial distance the resonant torques due to the binary companion begin to play a bigger role. Okazaki et al. (2002) studied the gravitational effects of close companions on the structure of the disks in Be/X-ray binary systems and found that the disk was truncated, at a certain point, called the truncation radius, by the companion. This was first suggested by Reig et al. (1997) who studied Be/X-ray systems and found a relationship between the size of the Hα emitting region and the size of the disk, demonstrating that the companion, in their case a neutron star, halted the flow of material and effectively truncated the disk. In a study of Be disks in coplanar binary systems, Panoglou et al. (2016) found that the position of the truncation radius depends on the parameters of both the disk (kinematic viscosity) and the binary (orbital period, mass ratio, eccentricity).

Just inside the truncation radius, it was found that the disk density decreases at a slightly slower rate with increasing distance from the star than what is observed in disks around isolated Be stars (Okazaki et al., 2002; Panoglou et al., 2016). As a result, the radial density distribution is flatter in binary systems and consequently disks in binary systems may be denser, and therefore more massive, than those in isolated systems. This phenomenon was called the "accumulation effect". Panoglou et al. (2016) found these effect to be stronger the smaller the viscosity and the orbital period and larger the mass ratio. Outside the truncation radius (i.e. the outermost portions of the disk), however, the density falls off at a substantially increasing rate. They, as well as Okazaki et al. (2002), also observed that $\alpha_{\rm SS}$ had an effect on the rate of the density fall-off in the outer part of the disk, with high viscosity disks having slower drop-off rates than low viscosity disks (see figure 11 of Panoglou et al., 2016).

In addition to these changes in density, Okazaki et al. (2002) found that the surface density of the disk revealed the development of a two-armed spiral density wave at periastron (figures 10 and 11 of Okazaki et al., 2002) with one arm

preceding the companion and the other located on the opposite side of the disk. Similar spiral waves were also observed by Panoglou et al. (2016).

In this study we use a numerical hydrodynamics code to expand on the works of Okazaki et al. (2002) and Panoglou et al. (2016) by investigating how these system evolve when the plane of the disk and binary are misaligned. Our goal is to understand how this misalignment, as well as various disk and orbital parameters, affect the density structure and dynamics of the disk. While much of the recent work in the literature is focused on X-ray and γ-ray Be binary systems, in this study we investigate, in a systematic fashion, the effect of a low mass, main sequence binary companion on Be star disks for misaligned orbits over a range of $\alpha_{\rm SS}$ and orbital period. The organization is as follows: Section 2 describes our methodology, results are presented in Section 3, and a discussion and summary is provided in Section 4.

3.2 Methodology

3.2.1 Disk modelling

In order to study the hydrodynamical effects of a misaligned companion on the structure and dynamics of the disk, a three-dimensional (3D) smoothed particle hydrodynamics (SPH) code was used. This type of code solves the fluid equations by dividing the fluid into discrete elements called particles. The properties of each particle are smoothed over a finite spacial distance (smoothing length) using a kernel function in order to simulate a continuous fluid. The SPH code used in this work is based on the code developed by Benz (1990) and Benz et al. (1990). It was later modified by Bate (1995) to include a second-order Runge-Kutta-Fehlberg integrator which uses individual time steps for each of the particles in order to decrease computational time. This code was later refined by Okazaki et al. (2002) for use in simulations of Be-binary systems.

The disk systems constructed and followed in this work are binary systems where the primary is a Be star and the secondary is a low mass main sequence star assumed to be in a circular orbit. Each simulation starts as a disk-less system at the beginning of its disk building phase. The injection of mass into the

disk is accomplished by placing a prescribed number of particles at the injection radius, $r_{\rm inj} = 1.04R_\star$, where $R_\star$ is the radius of the primary star. These mass injection events occur periodically and frequently during the simulation with the same number of particles ($N_{\rm part}$) are created each time. The initial velocity of each particle is set to be Keplerian without any radial momentum. All particles were given the same mass, which remained constant throughout the simulations. These masses, $m_{\rm part}$, are calculated based on the mass injection rate ($\dot{M}_{\rm inj}$) of the system and the number of particles ($N_{\rm part}$) created during each mass injection event, both of which are constant throughout the simulations. For this work these values were set to $\dot{M}_{\rm inj} = 10^{-8}$ M$_\odot$/yr and $N_{\rm part} = 6000$, resulting in $m_{\rm part} \approx 4 \times 10^{-15}$ M$_\odot$.

Once injected into the disk, particles interact with each other through viscosity which transfers angular momentum throughout the disk. Most particles eventually fall back onto the star while the remainder move outward, carrying angular momentum with them away from the central star. The Shakura-Sunyaev viscosity $\alpha_{\rm SS}$-prescription (Shakura et al., 1973) is used to define the viscosity of the system. Details about the implementation of the viscosity into the SPH code can be found in Okazaki et al. (2002). The disk is assumed to be isothermal, therefore the gas particles are all set to the same temperature. The disk temperature ($T_{\rm disk}$) was set to 60% of the effective temperature of the star, which has been found to be a good approximation for the temperature structure of the disk (Carciofi et al., 2006; Millar et al., 1998).

The stars are modelled using sink particles delimited by an accretion radius inside which any particle is assumed to have accreted onto the star and is therefore removed from the simulation. The accretion radius of the primary (Be star) is equal to the radius of the star, which in this work was set to 3.67 $R_\odot$, typical of a main-sequence B5 star. The accretion radius for the secondary is determined using the Eggleton approximation of the Roche lobe $R_{\rm L}$.

$$R_{\rm L} = \frac{0.49q^{2/3}}{0.6q^{2/3} + \ln(1 + q^{1/3})}a, \tag{3.1}$$

where q is the mass ratio of the stars ($q = M_{\rm sec}/M_{\rm prim} < 1$) and a is the

separation distance between them. Note that a changes over time for eccentric systems, however since we focus on circular orbits in this work $R_{\rm L}$ remains fixed throughout each simulation. The masses, radii, and effective temperatures of the stars were based on the parameters of the Pleione binary system (Harmanec, 1988; Hirata, 2007; Nemravová et al., 2010) and can be found in Table 3.1.

In order to investigate the effect of the companion on the disk, we varied three parameters: the misalignment angle θ, defined as the angle between the stellar equator of the primary and the plane of the binary orbit, the viscosity parameter, $\alpha_{\rm SS}$, and the orbital period of the binary. Simulations were run for four misalignment angles ($\theta = 0°$, $30°$, $45°$, $60°$), three values of viscosity ($\alpha_{\rm SS} = 0.1$, 0.5, 1.0), and for binary systems with short (30 days) and long (60 days) orbital periods, corresponding to a semi-major axis of 59.9 $R_\odot$ and 95.1 $R_\odot$, respectively.

Similarly to Panoglou et al. (2016), we define p as the orbital phase of the secondary during a single orbit, with $0 \leq p < 1$. We examine four orbital phases, $p = 0.00$, 0.25, 0.50, and 0.75. Figure 3.1 shows a graphical depiction of this notation scheme. Here the $x - y$ plane is defined as the plane of the stellar equator with the z axis pointing out of the figure. The Be star is represented by the gray circle at the center of the figure while the solid black line shows the path of the secondary*. For each position of the secondary (black circles) we have indicated the corresponding orbital phase p and whether the secondary is above ($z > 0$), below ($z < 0$), or in ($z = 0$) the plane of the disk. Note that in the aligned case ($\theta = 0$) the path of the secondary is circular and the secondary stays in the plane of the disk at all times. A cylindrical coordinate system (r,ϕ,z) is used when describing specific locations or cross-sections inside the disk, with the origin defined at the primary and the (r,ϕ,0)-plane defined as the plane of the stellar equator. The angle ϕ is defined from the positive x-axis moving counter-clockwise. The dashed lines in Figure 3.1 show the directions of the azimuthal angles $\phi = 0°$, $90°$, $180°$, and $270°$.

*Note that this is the orbital path projected onto the plane of the disk, explaining why the orbit appears elliptical.

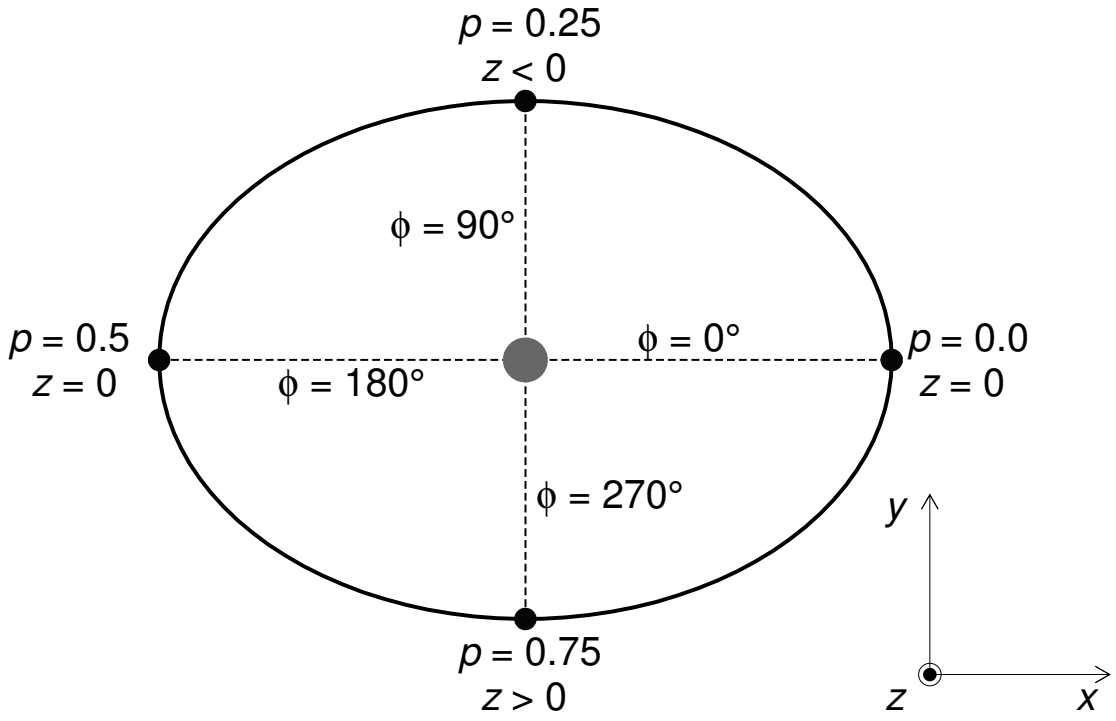

Figure 3.1: Graphical representation of a misaligned system from a top-down view perpendicular to the plane of the disk. The gray circle represents the Be star (primary) while the smaller black circles show the positions of the secondary at various orbital phases, p, along a projection of its orbital path (solid line). Also shown is whether the secondary is above ($z > 0$), below ($z < 0$), or in ($z = 0$) the plane of the disk. The dashed lines show the direction of the four principal azimuthal angles ϕ in relation to the phases of the secondary. The axes are defined such that the *x*-axis points to the right, the *y*-axis upward, and the *z*-axis points out of the page, as indicated at the bottom right of the Figure.

Table 3.1: Adopted parameters of the binary system.

Parameters	Values
Mass of primary	2.9 $M_\odot$
Radius of primary	3.67 $R_\odot$
Effective temperature	12000 K
Mass of secondary	0.31 $M_\odot$
Radius of secondary	0.38 $R_\odot$
Eccentricity	0
Mass injection rate	10^{-8} $M_\odot$/yr
Particles mass	$4\times10^{-15}M_\odot$

3.3 Results

3.3.1 Average Surface Density

It is informative to calculate some of the average features of the disk prior to investigating localized changes or perturbations. We start with an investigation of the average disk density. This is accomplished by transferring the particles to a cylindrical grid centred at the primary. The density is then integrated vertically to obtain the azimuthally averaged surface density ($\langle\Sigma(r)\rangle_\phi$). This same procedure was adopted by Panoglou et al. (2016).

One important aspect we first consider is whether our simulations are sufficiently developed so that the only major variations are those caused by the motion of the secondary. As Haubois et al. (2012) showed,using the one-dimensional time-dependent hydrodynamic code singlebe (Okazaki, 2007; Okazaki et al., 2002), disks around isolated Be stars will continue to grow as long as there is a continuous and constant injection of mass and angular momentum from the star, meaning they will never reach a state of perfect equilibrium. However we also know that the growth of the disk, although fast in the beginning of its

building phase, slows dramatically as the disk expands outward (Haubois et al., 2012). The disks should therefore reach a quasi-steady state (QSS), where the disk growth become insignificantly small within the span of one orbital period. It is also important to note that, since Be star disks are built from the inside out, the inner parts reaches QSS much faster than the outer parts. See section 2.1 of Panoglou et al. (2016) for a more in depth discussion.

Figures 3.2(a) through (f) show log-log plots of the temporal evolution of the azimuthally averaged surface density, $\langle \Sigma(r) \rangle_\phi$, at various times during the disk building phase (see legend). The leftmost and rightmost panels show the results for short and long period systems, respectively, with each row, from top to bottom, for $\alpha_{\rm SS}$ of 0.1, 0.5, and 1.0, respectively. Each simulation was run up to 50 orbital periods (P_{orb}). Note that only the aligned systems ($\theta = 0$) are shown in Figure 3.2, however we have found the QSS time is virtually the same for the corresponding misaligned cases.

We see that all simulations have reached QSS by 50 P_{orb}, although some reach it faster than others. We notice that higher viscosity disks reach their QSS much faster than lower viscosity disks. This result is similar to the temporal evolution of the surface density profile found by Panoglou et al. (2016) for aligned systems and by Haubois et al. (2012) for isolated Be stars; both found that disks with higher viscosity reach their steady-state faster than those with low viscosity. The number of active particles for the short period systems after 50 P_{orb} is presented in Table 3.2.

Figures 3.3(a) through (f) show $\langle \Sigma(r) \rangle_\phi$ after 50 full orbital periods. We see that the $\langle \Sigma_p(r) \rangle_\phi$ profiles in each case are similar in shape as those found in Okazaki et al. (2002) in his study of Be/X-ray binaries, with shallower slopes in the inner part of the disk and steeper slops in the outer parts. As Okazaki et al. (2002) explains this drop in surface density, or truncation, is due to the tidal forces generated by the secondary as it orbits the primary. Furthermore, similar to the findings of Okazaki et al. (2002), we notice that surface density profiles of the outer part of the disk become shallower with increasing $\alpha_{\rm SS}$. This can be attributed to the fact that high viscosity disks have a faster recovery time than low viscosity disks, since viscosity is the primary means with which angular mo-

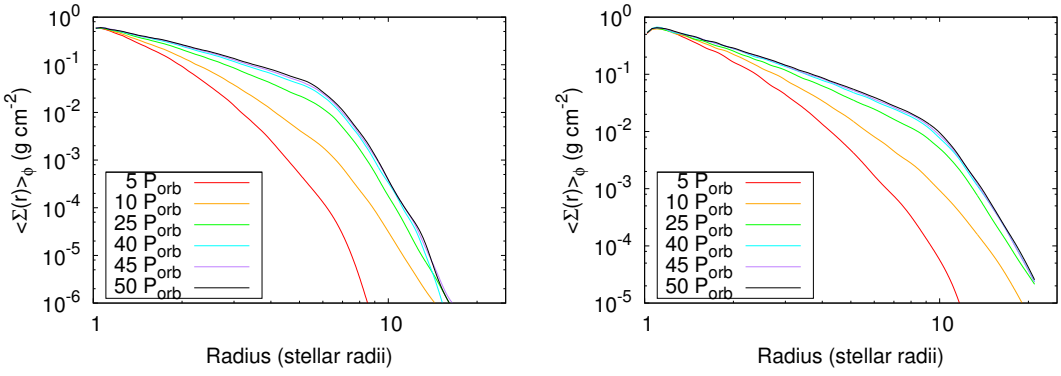

(a) 30 day period, $\alpha_{\rm SS} = 0.1$

(b) 60 day period, $\alpha_{\rm SS} = 0.1$

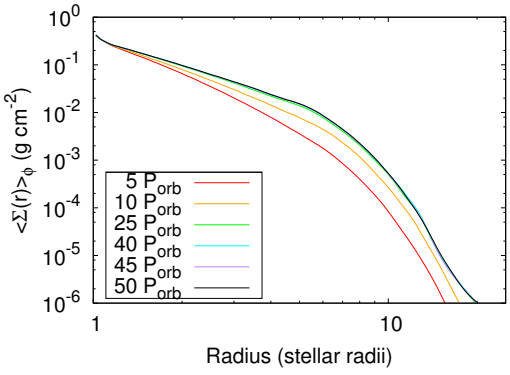

(c) 30 day period, $\alpha_{\rm SS} = 0.5$

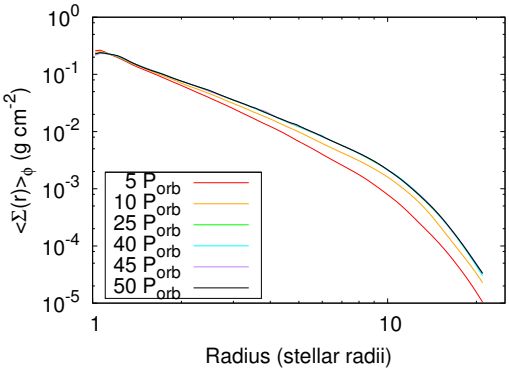

(d) 60 day period, $\alpha_{\rm SS} = 0.5$

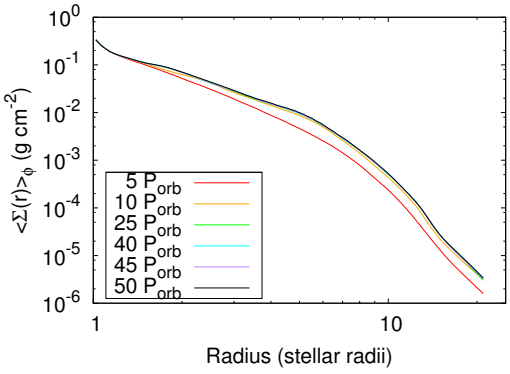

(e) 30 day period, $\alpha_{\rm SS} = 1.0$

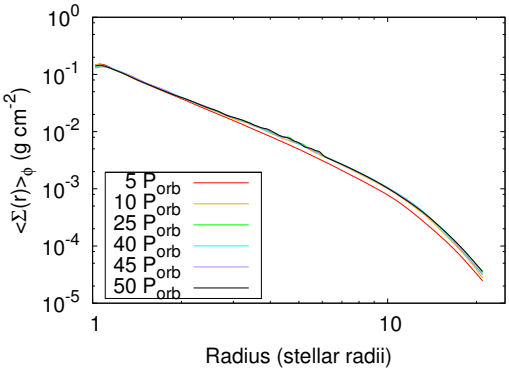

(f) 60 day period, $\alpha_{\rm SS} = 1.0$

Figure 3.2: Temporal evolution of the azimuthally averaged surface density, $\langle \Sigma(r) \rangle_\phi$, as a function of radius for the short (left column) and long (right column) orbital period systems, and for $\alpha_{\rm SS}$ values of 0.1 (top row), 0.5 (middle row), and 1.0 (bottom row).

Table 3.2: Approximate number of active particles after 50 P_{orb} for short period (30 day) systems.

Viscosity parameter	Misalignment angle	Number of active particles
$\alpha_{\rm SS} = 0.1$	0°	100,000
	30°	79,000
	45°	75,000
	60°	18,000
$\alpha_{\rm SS} = 0.5$	0°	37,000
	30°	36,000
	45°	37,000
	60°	39,000
$\alpha_{\rm SS} = 1.0$	0°	25,000
	30°	25,000
	45°	25,000
	60°	26,000

mentum in the disk is transported away from the star.

Now we move onto a systematic investigation of the changes in the disk over the range in parameters described previously. The misalignment angle also affects the surface density profile of the disk as seen in Figure 3.3. In all six panels we see that the greater the misalignment angle, the denser the outermost part of the disk. Conversely, the density in the inner parts appears to be mostly unaffected by the misaligned companion. In order to better investigate this, three properties of these profiles were examined, the truncation radius and the fall-off rate of the surface density in the inner and outer parts of the disk. The inner and outer parts are defined with respect to the truncation radius, the inner disk being the region inside the truncation radius and the outer part exterior to it. For this analysis the azimuthally averaged surface density profiles were fitted using the same function adopted by Okazaki et al. (2002);

$$\langle \Sigma(r) \rangle_{\phi} \propto \frac{(r/R_t)^{-m}}{1 + (r/R_t)^{n-m}}, \tag{3.2}$$

where R_t is the truncation radius, m is the power-law exponent of the inner disk, and n is the power-law exponent of the outer disk. Hereafter we will refer to m and n as the inner and outer exponent, respectively.

Figure 3.4 shows the temporal evolution of the surface density fall-off rate, m, in the inner parts of the disk. We see that the fall-off rate is initially high in most cases, but rapidly decreases until a steady-state value is reached. The estimated steady-state values for m, obtained by an exponential fit, can be found in Tables 3.3 and 3.4 for the short and long period systems, respectively.

However, where Haubois et al. (2012) found that the power law for isolated Be-stars tended toward $m = 2$, we found, in almost all cases, that the power law tended toward values of $m \leq 2$, which indicates the inner part is denser than a typical disk in an isolated Be star system. The same accumulation effect was also observed by Panoglou et al. (2016) for aligned systems. As we see from Figure 3.4 as well as Tables 3.3 and 3.4, the accumulation effect is stronger, overall, in aligned systems compared to misaligned systems, with little variation in the latter. We notice that the difference in accumulation between the aligned

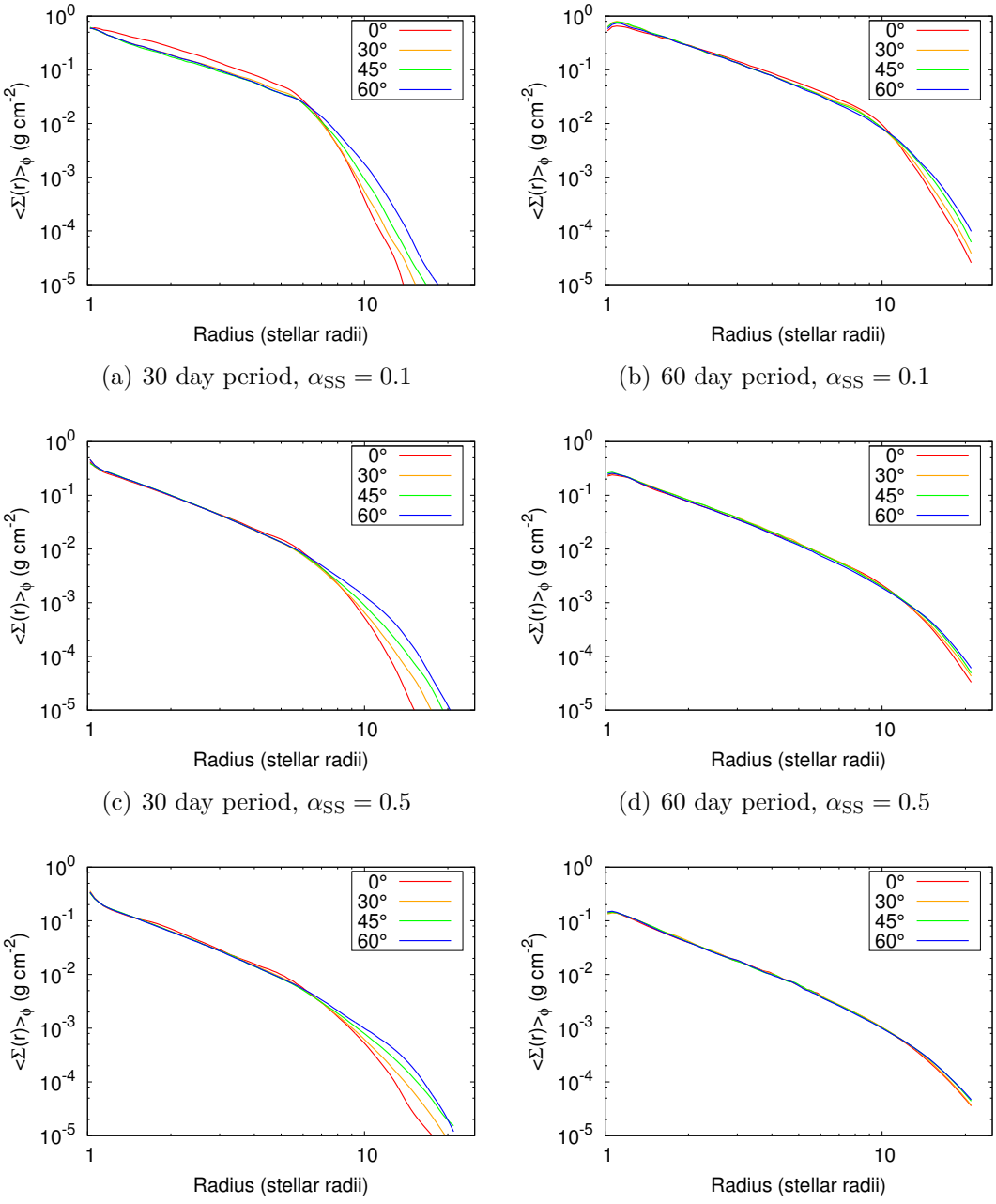

(a) 30 day period, $\alpha_{\rm SS} = 0.1$

(b) 60 day period, $\alpha_{\rm SS} = 0.1$

(c) 30 day period, $\alpha_{\rm SS} = 0.5$

(d) 60 day period, $\alpha_{\rm SS} = 0.5$

(e) 30 day period, $\alpha_{\rm SS} = 1.0$

(f) 60 day period, $\alpha_{\rm SS} = 1.0$

Figure 3.3: Azimuthally averaged surface density, $\langle \Sigma(r) \rangle_\phi$ for the short (left column) and long (right column) orbital period systems, and for $\alpha_{\rm SS}$ values of 0.1 (top row), 0.5 (middle row), and 1.0 (bottom row). The results shown were taken 50 P_{orb} after the start of the disk building phase. Each line represents a different misalignment angle, as indicated in the legend.

and misaligned systems increases substantially with viscosity. We also see that both the viscosity coefficient and orbital period have effects on the steady-state value of m. These dependences are in agreement with the results obtained by Panoglou et al. (2016). The only system where this effect is absent is in the system with both high viscosity and long orbital period (panel f). Here we see that m tends toward values equal or greater than 2. This indicates that the secondary is distant and viscosity is large enough that the torque is too weak to affect the density distribution in the inner disk, which then behaves like an isolated Be disk.

Figure 3.5 shows the temporal evolution of the surface density fall-off rate, n, in the outer parts of the disk. We see here that the slope n reaches a steady state value more quickly than m. However it is important to note that although the outer density slope reaches QSS faster, the density scale still requires a longer time to reach QSS compared to the inner disk. The estimated steady-state values for n are also presented in Tables 3.3 and 3.4. As seen in Figures 3.3 and 3.5 the fall-off rate in the outer disk is dependent on the misalignment angle, i.e. slower fall-off rates for highly misaligned systems.

The results for the truncation radius, obtained from Equation 3.2, are shown in Figure 3.6 with the steady-state values in Tables 3.3 and 3.4. The panel layout is the same as Figures 3.3 and 3.5. We see that the steady-state values of the truncation radius tends to be closer to the star for low misalignment angles and move farther out as the misalignment angle increases. We also notice that the truncation radius is farther away from the star in systems with higher disk viscosity and longer orbital periods. This is similar to the findings of Panoglou et al. (2016) for aligned systems.

The relationship between R_t, m, and n with regards to viscosity, orbital period, and misalignment angle is relatively intuitive. As mentioned earlier, viscosity determines how fast the disk can grow and recover between each interaction with the secondary. We therefore expect high viscosity disks to have more time to relax back to their unperturbed state than less viscous ones, reducing the impact of the accumulation effect (higher m) and allowing more material to flow into the outer disk (lower n and higher R_t). A longer orbital period also

Table 3.3: Steady-state values for the short period (30 day) systems.

Viscosity parameter [α_{SS}]	Misalignment angle [θ]	Inner slope [m]	Outer slope [n]	Truncation radius [R_t] (stellar radii)
0.1	0°	1.49	7.78	6.91
	30°	1.58	6.60	6.97
	45°	1.67	5.42	7.00
	60°	1.65	4.97	7.72
0.5	0°	1.92	5.48	8.03
	30°	1.99	3.95	8.41
	45°	1.99	3.43	9.27
	60°	2	3.81	10.9
1.0	0°	1.93	3.31	7.68
	30°	2.06	2.47	8.62
	45°	2.06	2.22	10.1
	60°	2.06	3.17	12.3

means that the outer disk has more time the rebuild itself between passages, and since the secondary is radially farther away from the disk, it has a smaller impact on the truncation of the disk. Similarly, increasing the misalignment angle also increases the vertical distance between the disk and the secondary when the latter is at its maximum elevation. This increased separation weakens the tidal torque on the disk resulting in a weaker truncation.

3.3.2 Disk Warping

In order to study the warping of the disk, we consider the vertical displacement of the disk above and below the equatorial plane along various radial directions. To accomplish this, we first determine the position of the centre of mass along the vertical axis ($z_{\rm CoM}$) along the r-axis for various values of ϕ (dashed lines in Figure 3.1), using the following equation:

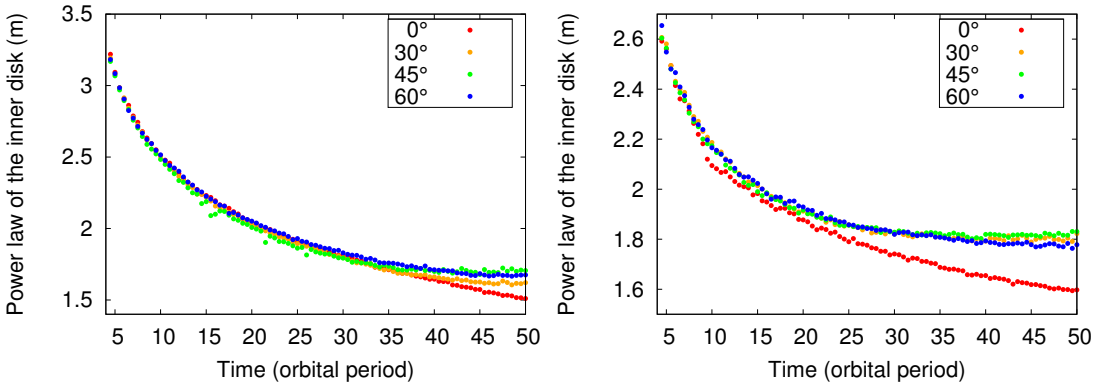

(a) 30 day period, $\alpha_{SS} = 0.1$

(b) 60 day period, $\alpha_{SS} = 0.1$

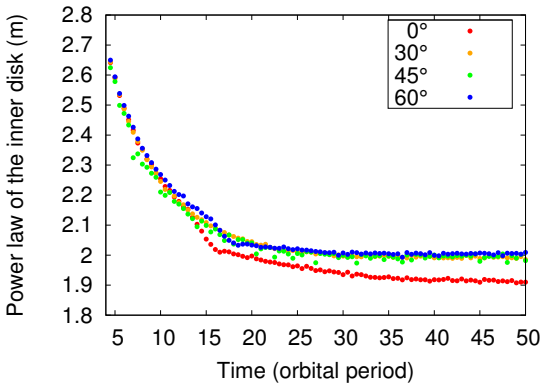

(c) 30 day period, $\alpha_{SS} = 0.5$

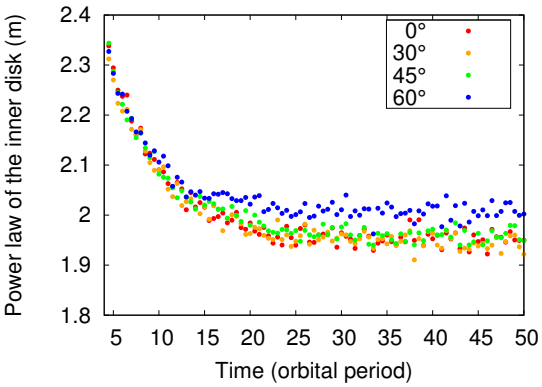

(d) 60 day period, $\alpha_{SS} = 0.5$

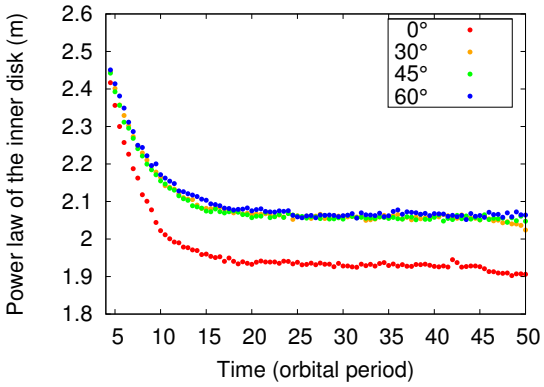

(e) 30 day period, $\alpha_{SS} = 1.0$

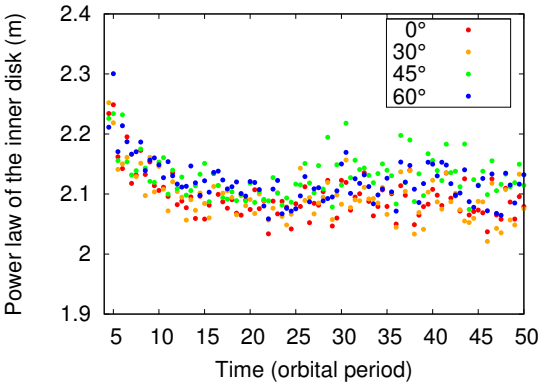

(f) 60 day period, $\alpha_{SS} = 1.0$

Figure 3.4: Temporal evolution of the slope of the inner disk, obtained from Equation 3.2 for the short (left column) and long (right column) orbital period systems, and for α_{SS} values of 0.1 (top row), 0.5 (middle row), and 1.0 (bottom row).

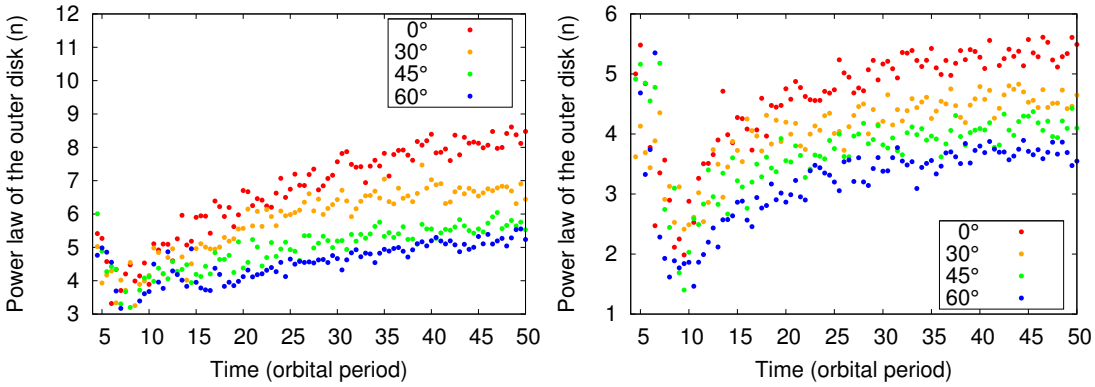

(a) 30 day period, $\alpha_{SS} = 0.1$

(b) 60 day period, $\alpha_{SS} = 0.1$

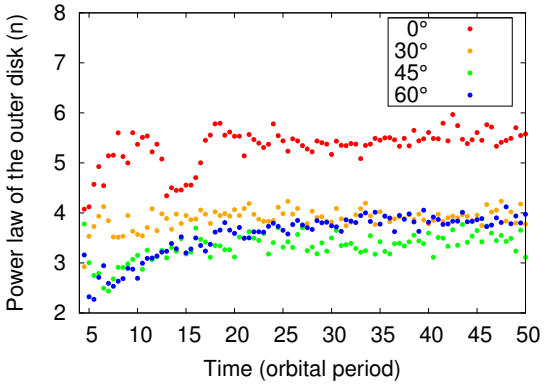

(c) 30 day period, $\alpha_{SS} = 0.5$

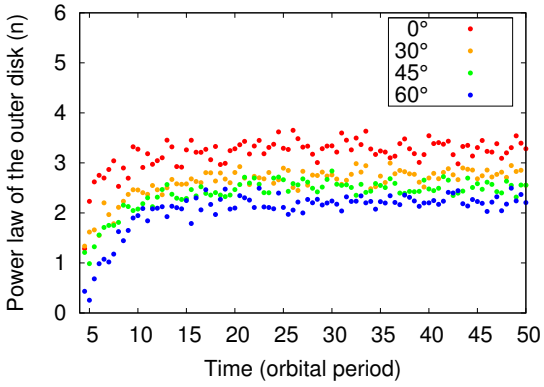

(d) 60 day period, $\alpha_{SS} = 0.5$

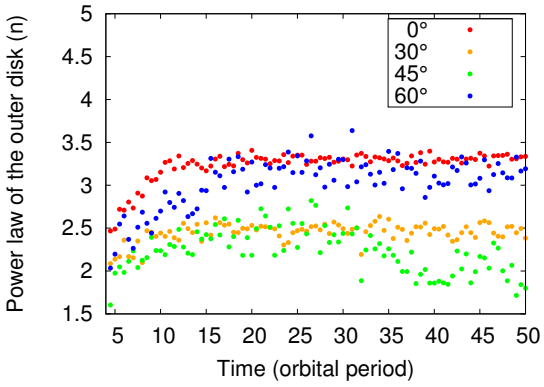

(e) 30 day period, $\alpha_{SS} = 1.0$

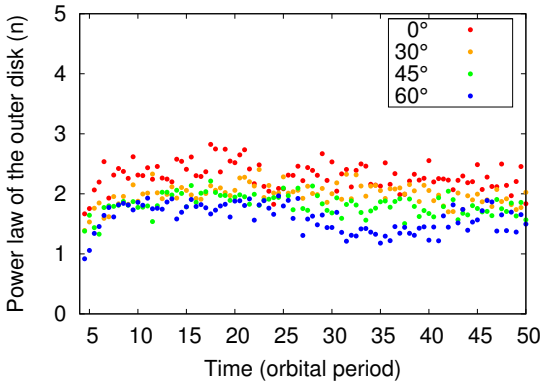

(f) 60 day period, $\alpha_{SS} = 1.0$

Figure 3.5: Same as Figure 3.4 for the slope of the outer disk obtained from Equation 3.2.

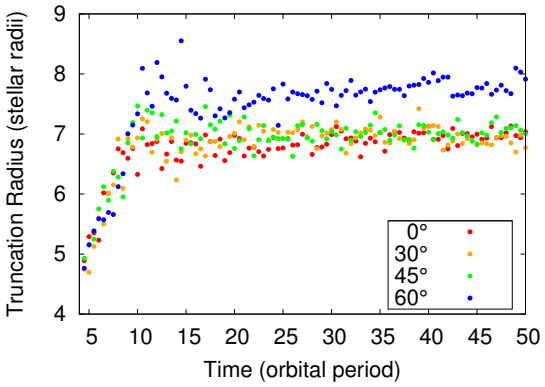

(a) 30 day period, $\alpha_{SS} = 0.1$

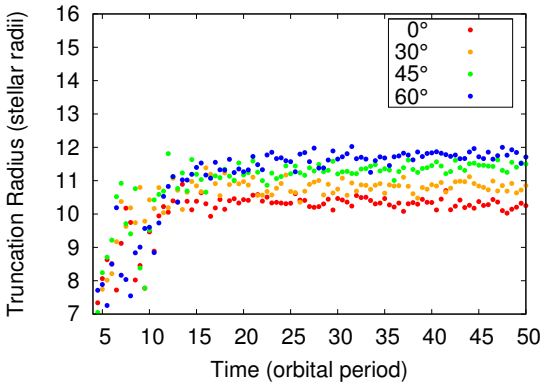

(b) 60 day period, $\alpha_{SS} = 0.1$

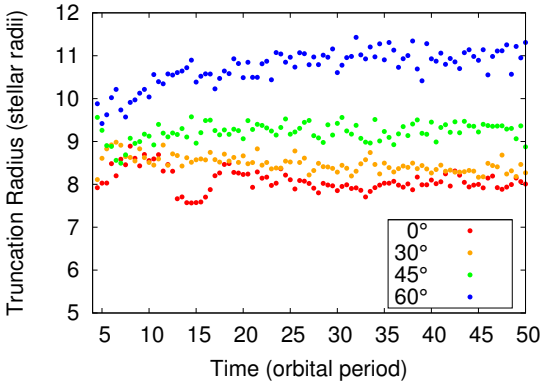

(c) 30 day period, $\alpha_{SS} = 0.5$

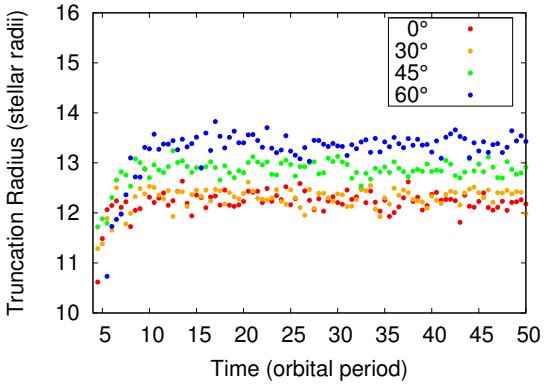

(d) 60 day period, $\alpha_{SS} = 0.5$

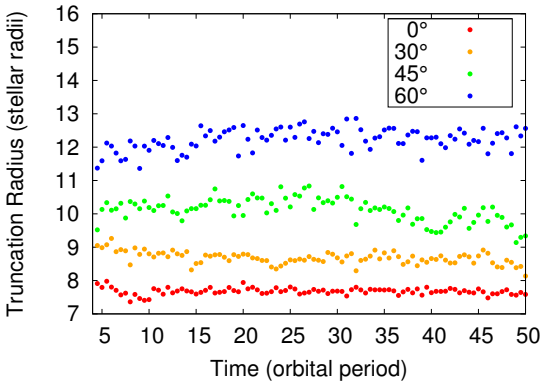

(e) 30 day period, $\alpha_{SS} = 1.0$

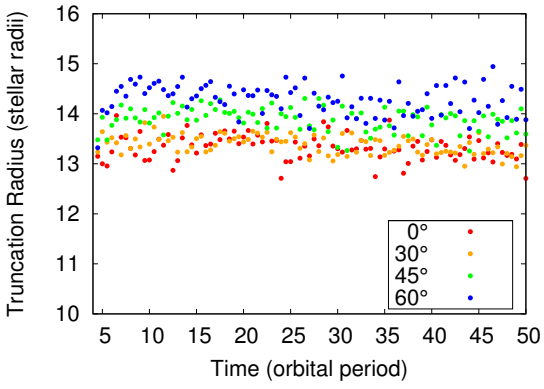

(f) 60 day period, $\alpha_{SS} = 1.0$

Figure 3.6: Same as Figure 3.4 for the truncation radius obtained from Equation 3.2.

Table 3.4: Steady-state values for the short period (60 day) systems.

Viscosity parameter [α_{SS}]	Misalignment angle [θ]	Inner slope [m]	Outer slope [n]	Truncation radius [R_t] (stellar radii)
0.1	0°	1.61	5.23	10.34
	30°	1.8	4.41	10.81
	45°	1.81	3.96	11.34
	60°	1.78	3.55	10.69
0.5	0°	1.95	3.32	12.25
	30°	1.95	2.75	12.32
	45°	1.96	2.54	12.89
	60°	2.01	0.22	13.37
1.0	0°	2.08	2.27	13.30
	30°	2.09	2.01	13.34
	45°	2.12	1.81	13.84
	60°	2.11	1.55	14.23

$$z_{\mathrm{CoM}}(r,\phi) = \frac{\sum_k \rho_k(r,\phi) z_k}{\sum_k \rho_k(r,\phi)}, \tag{3.3}$$

where $\rho_k(r,\phi)$ and z_k are the density and corresponding vertical position of a column density located at (r,ϕ). Next we convert the vertical position z_{CoM} into an warping angle γ by trigonometry:

$$\gamma(r,\phi) = \arctan \frac{z_{\mathrm{CoM}}(r,\phi)}{r}. \tag{3.4}$$

Figures 3.7 through 3.9 show how the warping angle of the disk as a function of radius varies along azimuthal angles ($\phi = 0°$, $90°$, $180°$, $270°$) at various phases of an orbit ($p = 0.0$, 0.25, 0.5, 0.75) for misaligned systems. The warping angle of the aligned model is not shown as it zero everywhere in the disk, as expected. The location of the average truncation radius, as found in Table 3.3, is indicated by the dashed line. The caption under each panel of Figures 3.7 to 3.9 indicates the phase p and the vertical position of the disk relative to the plane of the disk (see Figure 3.1).

As expected we see clear evidence of vertical displacement in the disks as well as other interesting features. First we notice a mirroring effect that seems to happen every half period, when the secondary goes from one side of the primary to the other. Comparing panels together, we see that features present at a particular phase p in a certain direction ϕ will also be present at a phase of $p \pm 0.5$ and in the direction of $\phi \pm 180°$ but on the other side the plane of the disk (above to below and vice versa). This is to be expected due to the symmetrical nature of the system.

Secondly we see that the vertical displacements are not larger in the directions of the maximum elevation, i.e when the secondary passes the farthest above and below the disk ($\phi = 90°$ and $270°$); we see instead much larger deviations in the directions of the line of nodes, i.e. where the orbit intersects with the equatorial plane ($\phi = 0°$ and $180°$). However we do see an increase in warping along the $\phi = 90°$ and $\phi = 270°$ directions when the secondary is at its lower ($p = 0.25$) and highest ($p = 0.27$) elevation, respectively. Furthermore this increase occurs just past the truncation radius for all misalignment angles.

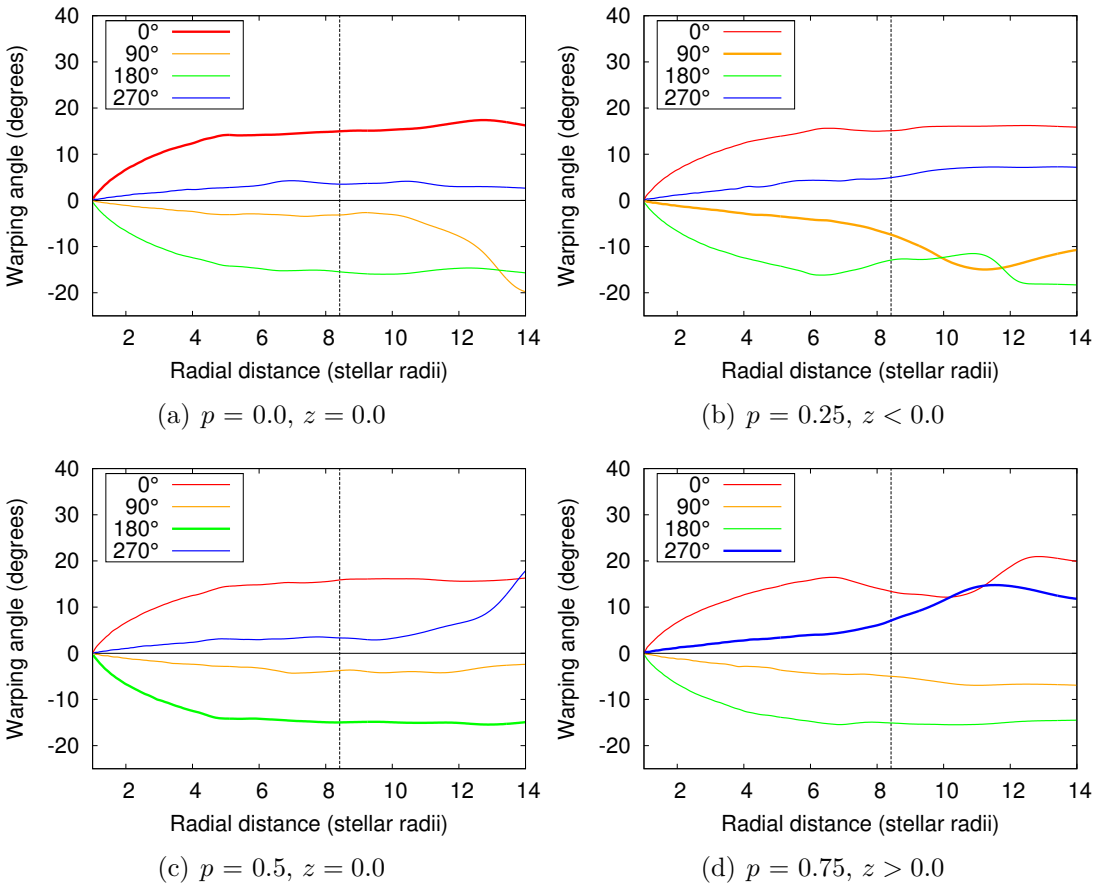

(a) $p = 0.0$, $z = 0.0$

(b) $p = 0.25$, $z < 0.0$

(c) $p = 0.5$, $z = 0.0$

(d) $p = 0.75$, $z > 0.0$

Figure 3.7: Warping angle of the disk as a function of radius in the short period system with $\alpha_{\rm SS} = 0.5$ and a misalignment angle of 30°. The lines represent a different direction along the azimuthal angle ϕ; 0° (red), 90° (orange), 180° (green), 270° (blue). Each panel shows the system at a different phase, p, over one orbital period from 49 P_{orb} to 50 P_{orb}; $p = 0.0$ (a), $p = 0.25$ (b), $p = 0.5$ (c), $p = 0.75$ (d). The dashed line shows the average position of the truncation as shown in Table 3.3.

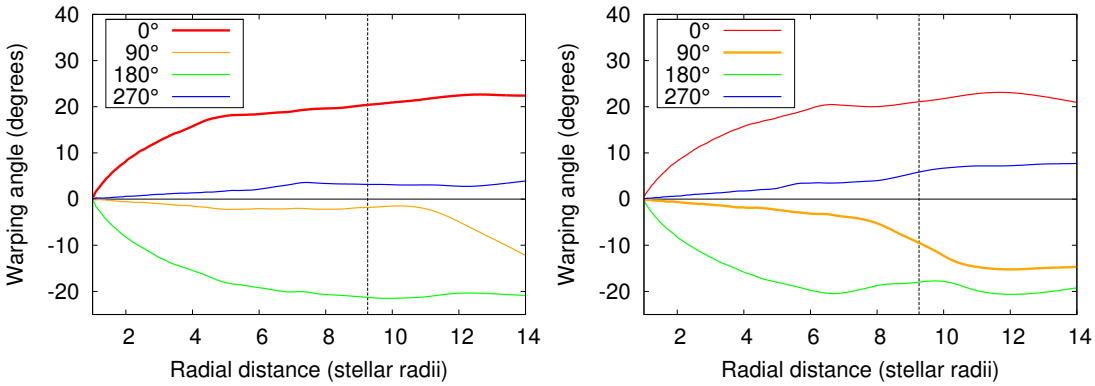

(a) $p = 0.0$, $z = 0.0$ (b) $p = 0.25$, $z < 0.0$

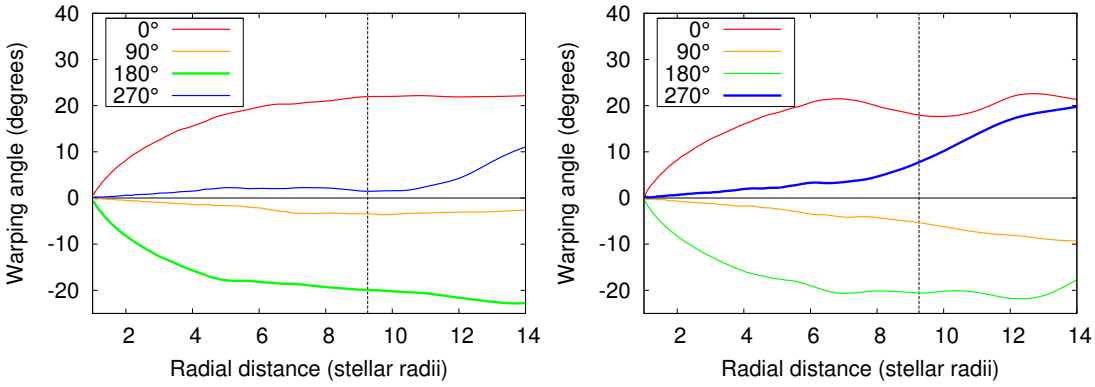

(c) $p = 0.5$, $z = 0.0$ (d) $p = 0.75$, $z > 0.0$

Figure 3.8: Same as Figure 3.7 but for a misalignment angle of 45°.

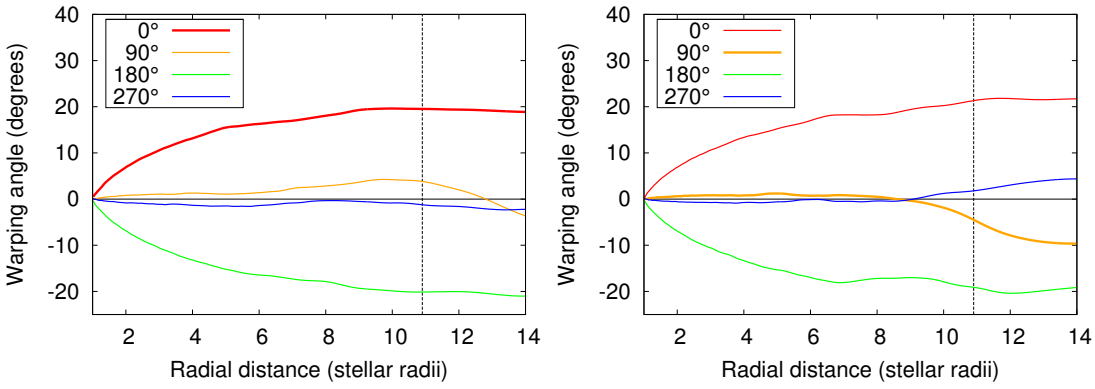

(a) $p = 0.0$, $z = 0.0$ (b) $p = 0.25$, $z < 0.0$

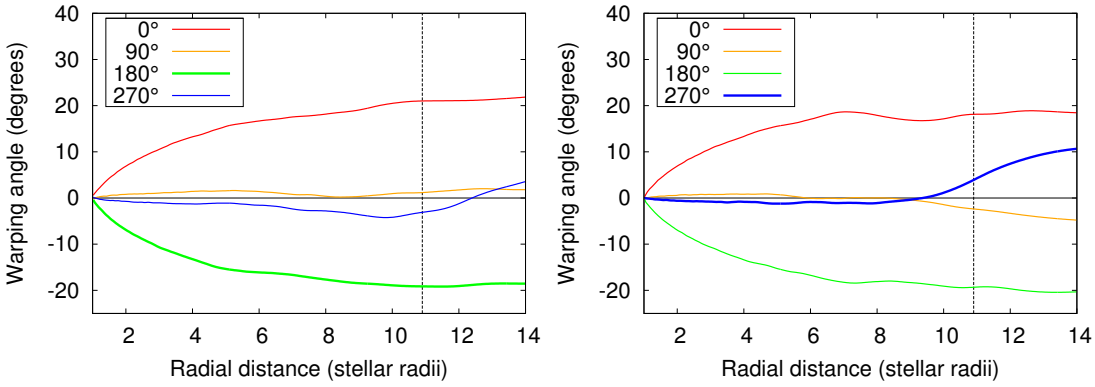

(c) $p = 0.5$, $z = 0.0$ (d) $p = 0.75$, $z > 0.0$

Figure 3.9: Same as Figure 3.7 but for a misalignment angle of 60°.

Thirdly, we notice that the amount of warping varies with misalignment angle in both the direction of the line of nodes and of maximum elevation. In the former, we see that the warping becomes more significant as the misalignment angle increases from 30° to 45°, but then decreases slightly when increased to 60°. As for the latter, the warping steadily decreases as the misalignment increases. We also notice that at 60° the inner disk warps upward along the $\phi = 90°$ line (yellow) and downward along the $\phi = 90°$ line (blue). As the secondary moves to greater distances above or below the equatorial plane, the increased separation between the secondary at its highest position counters the warping effects do to the weakening tidal torque in the vertical direction.

Figure 3.10 compares the temporal evolution over one period of the warping of the disk for different viscosity; $\alpha_{SS} = 0.1$ (left panels), $\alpha_{SS} = 0.5$ (center panels), and $\alpha_{SS} = 1.0$ (right panels), and for a misalignment angle of 45°. Note that the center panels are the same as those presented in Figure 3.8. We see that the mirroring effect is still present for disks with higher and lower viscosities. The only exception, however, is visible in panel (j), where a sharp change in the warping toward $\phi = 180°$ (green line) is evident which is not mirrored in panel (d) for $\phi = 0°$ (red line). However we should keep in mind that low viscosity disks have a sharper drop in density in the outer region where this break in symmetry occurs. This could have affected the results of our analysis for this specific simulation. We also notice that the warping is weaker for the low viscosity disks but with little variation between $\alpha_{SS} = 0.5$ and 1.0. This could be due to the fact that low viscosity disks have a much smaller truncation radius than high viscosity disks, which would dampen the warping of the inner disk.

3.3.3 Scale Height

The scale height (or effective thickness) of the disk is an important quantity sometimes assumed or estimated for modelling disks. Variations in scale heights can have a significant effect on the density structure and the temperature distribution of the disk, which, in turn, will have an effect on the estimation of observables such as emission line profiles and IR continuum levels (Carciofi et al., 2008). Therefore we investigate the disk scale height in this work. The standard

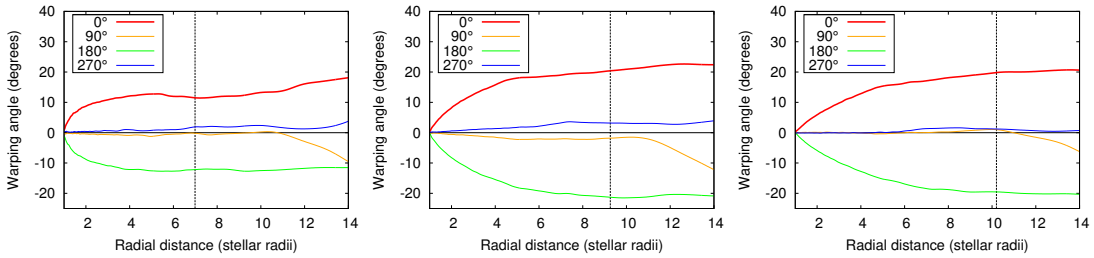

(a) $p = 0.0$, $\alpha_{\rm SS} = 0.1$ (b) $p = 0.0$, $\alpha_{\rm SS} = 0.5$ (c) $p = 0.0$, $\alpha_{\rm SS} = 1.0$

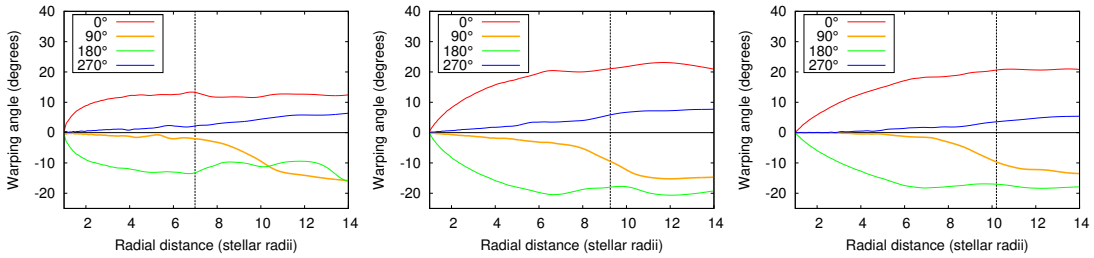

(d) $p = 0.25$, $\alpha_{\rm SS} = 0.1$ (e) $p = 0.25$, $\alpha_{\rm SS} = 0.5$ (f) $p = 0.25$, $\alpha_{\rm SS} = 1.0$

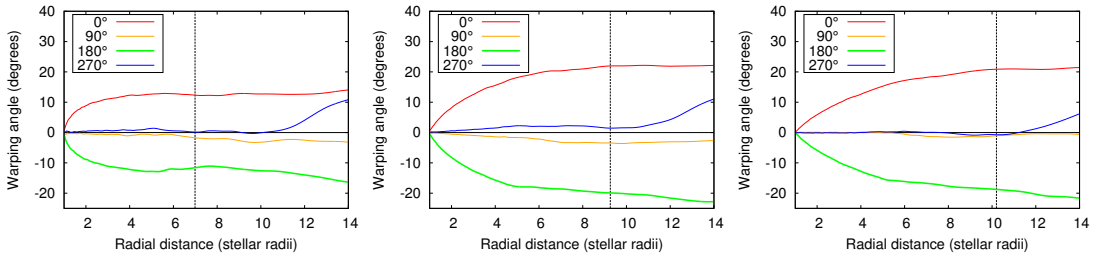

(g) $p = 0.5$, $\alpha_{\rm SS} = 0.1$ (h) $p = 0.5$, $\alpha_{\rm SS} = 0.5$ (i) $p = 0.5$, $\alpha_{\rm SS} = 1.0$

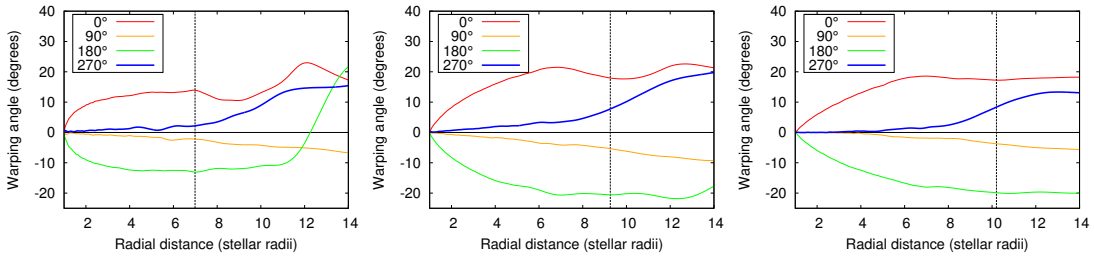

(j) $p = 0.75$, $\alpha_{\rm SS} = 0.1$ (k) $p = 0.75$, $\alpha_{\rm SS} = 0.5$ (l) $p = 0.75$, $\alpha_{\rm SS} = 1.0$

Figure 3.10: Warping angle of the disk as a function of radius for short period systems with misalignment angle of 45° viewed at different phases, p, and viscosities, $\alpha_{\rm SS}$. From top to bottom, $p = 0.0$, 0.25, 0.5, and 0.75 (from 49 P_{orb} to 50 P_{orb}) and from left to right $\alpha_{\rm SS} = 0.1$, 0.5, and 1.0. The dashed line shows the average position of the truncation as shown in Table 3.3.

equation for the scale height of an isolated Be star is;

$$H(r) = c_s/\Omega(r), \tag{3.5}$$

where Ω is the Keplerian angular velocity at a distance r from the star. This relationship is obtained by assuming that the disk is in vertical hydrostatic equilibrium. A derivation of this equation can be found in Carciofi et al. (2008). Equation 3.5 assumes the presence of a single source of gravitational potential, the Be star. It is therefore important to determine whether or not Equation 3.5 is appropriate to estimate the scale height in Be binary systems that are aligned and misaligned.

In order to extract the scale height throughout the disk, we computed the vertical density structure of the gas at various points in the disk. The vertical density structure of the disk can be described using a Gaussian function;

$$\rho(z) \propto e^{-z^2/2H^2}, \tag{3.6}$$

where H is the scale height of the disk (Carciofi et al., 2008). Equation 3.6, however, assumes a Gaussian centred at $z = 0$, which is a good assumption for isolated Be star systems or aligned systems but not for misaligned systems where we have a warped disk. We therefore modified Equation 3.6 to include a second fitting parameter, λ, which represents how shifted the Gaussian is in z:

$$\rho(z) \propto e^{-(z-\lambda)^2/2H^2}. \tag{3.7}$$

Figure 3.11 shows the ratio between the scale height obtained through simulations ($H_{\rm sim}$) and the theoretical scale height ($H_{\rm th}$) computed from Equation 3.5, for short period systems, $\alpha_{\rm SS} = 0.5$, and with misalignment angles of (a) 0°, (b) 30°, (c) 45°, and (d) 60°.

We see that our simulated disks have scale heights which are around twice as large as what is expected from Equation 3.5 for both aligned and misaligned systems. Furthermore we see bigger deviations between our simulations and the theory in the outer disk. Interestingly these deviations are more pronounced

for higher misalignment angles and appear in the shape of a double spiral arm, very similar to the shape density waves typically seen in aligned Be-binary systems[†]. This might indicate that Equation 3.5 does not adequately describe the scale height in these types of systems, but it is also possible that the smoothing length adopted by the code may not have been small enough, resulting in inaccurate scale height calculations.

3.4 Discussion and Conclusion

In this investigation we use numerical simulations to study the behaviour of Be star disks in aligned and misaligned binary systems. Simulations were obtained using a smoothed-particle hydrodynamics (SPH) code following previous methods developed and described in the literature (Benz, 1990; Benz et al., 1990; Okazaki et al., 2002). In our simulations, we varied the degree of misalignment between the plane of the orbit and the plane of the disk, the viscosity parameter, $\alpha_{\rm SS}$, and the orbital period of the system, P_{orb}.

First we studied the azimuthally averaged surface density, $\langle\Sigma(r)\rangle_{\phi}$, by investigating the density fall-off rate in the inner and outer parts of the disk (m and n respectively), and the truncation radius (R_t). We find, as reported by Panoglou et al. (2016) for coplanar orbits,that material tends to build up in the innermost part of the disk, called the accumulation effect, for our misaligned systems with the density fall-off values of m reaching values below 2 for most systems. Furthermore we find that the degree of misalignment does have an effect on the magnitude of the accumulation, with a greater accumulation (lower m) in aligned systems and with less accumulation in misaligned systems. This difference between aligned and misaligned systems is found to also increase with viscosity. Only for disks with the highest viscosity ($\alpha_{\rm SS} = 1.0$) and the longest orbital period ($P_{orb} = 60$ days) do we find little evidence of accumulation. As reported by Panoglou et al. (2016), both $\alpha_{\rm SS}$ and P_{orb} also have an influence on the accumulation found in the inner disk. Similarly we find that R_t also has a dependence on the misalignment angle. disks in aligned systems are found to be

[†]See figure 4 of Panoglou et al. (2016) and figures 10 and 11 of Okazaki et al. (2002).

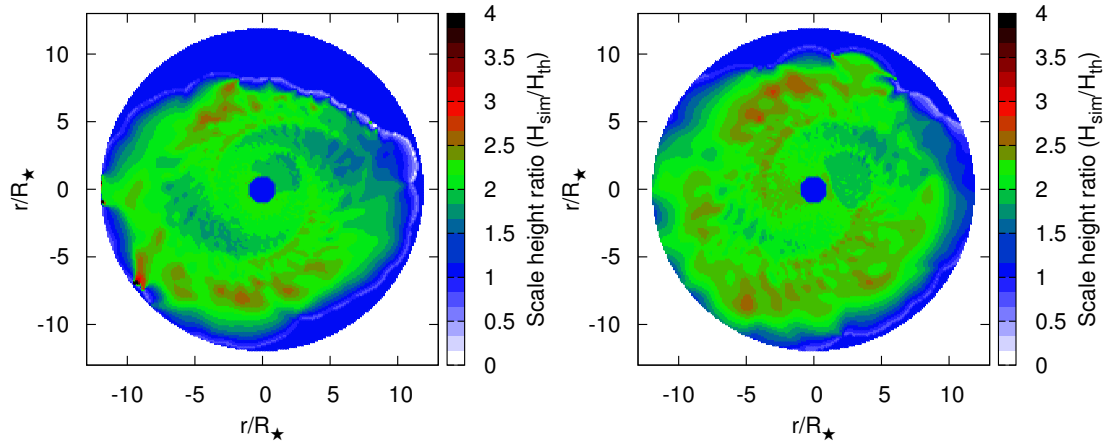

(a) Misalignment angle = 0°

(b) Misalignment angle = 30°

(c) Misalignment angle = 45°

(d) Misalignment angle = 60°

Figure 3.11: Ratio between the scale height obtained from simulations ($H_{\rm sim}$) and theoretical scale height ($H_{\rm th}$) computed from Equation 3.5 for short period systems with $\alpha_{\rm SS} = 0.5$ and misalignment angles of (a) 0°, (b) 30°, (c) 45°, (d) 60°. The disk is truncated at 12 stellar radii in this Figure.

truncated closer to the star compared to disks in misaligned systems, with the truncation farther from the primary as the misalignment increases. This is in agreement with the findings Lubow et al. (2015) that disks in misaligned systems have a greater radial extent than their counterparts in aligned systems. We also find that $\alpha_{\rm SS}$ and P_{orb} have similar effects on the truncation, that is, the truncation is farther from the primary as both $\alpha_{\rm SS}$ and P_{orb} increase. This is also in agreement with the results of Panoglou et al. (2016). Finally, n is found to vary with the misalignment of the system as well. Larger misalignment angles result in denser outer disks, i.e. smaller n.

We also studied the warping of the disk by computing the centre of mass throughout the disk with respect to the plane of the stellar equator. We find the warping to be symmetric over 0.5 P_{orb}, mirroring the symmetry in the path of the secondary. We also find that the disk warps less in the directions where the secondary passes the farthest above or below the disk ($\phi = 90°$ and $270°$, Figure 3.1) compared to the directions where the secondary passes in the plane of the disk (($\phi = 0°$ and $180°$, Figure 3.1). Finally we find that the amplitude of the warping depends on both the misalignment of the system and the viscosity of the disk. The disk is found to be more warped for misalignments of $45°$ and for $\alpha_{\rm SS}$ of 0.5 for the stellar and binary parameters adopted in this study.

Finally we compared the scale heights of our disks with the theoretical scale heights calculated using the standard equation for the case of an isolated Be star (Carciofi et al., 2008). We find that overall this approximation systematically underestimates the scale height by a factor of 2 for all misalignment angles. We note that this discrepancy could be caused by insufficiently small smoothing length. In the future, we wish to compare the variations of the scale height with the smoothing length to insure we have adequate resolution.

Martin et al. (2014) studied Kozai-Lidov oscillations in hydrodynamic disks and showed that for highly misaligned systems this mechanism could be set up. Figure 1 in Fu et al. (2015) shows that conspicuous disk oscillations can occur for orbital warpings that are large (i.e. 60 and $70°$). During these oscillations the disk can become quite eccentric over time as disk tilting and eccentricity are interchanged. Martin et al. (2014) suggest that these oscillations may be im-

portant for transient disks in Be/Xray systems. Using equation 3 in Fu et al. (2015) we find that Kozai oscillations would not be expected for our simulations computed to 50 P_{orb}. According to our calculations the simulations would need to be followed for approximately 80 P_{orb} in order to see evidence of Kozai oscillations in the inner disk. Nevertheless, in a future study we plan to study binaries in eccentric orbits and we plan to closely examine the disk shape and variations in inclination to search for the presence of Kozai oscillations.

Given we find that the disk density distribution and the geometry of the disk is altered in misaligned systems, it follows that observational features originating from altered portions of the disk will differ from isolated systems. Changes in disk density in the inner disk would be seen in observables such as polarization, UBV photometric colours, and spectroscopy, while interferometry, infrared and radio measurements could be used to predict the overall size and density in the disk. Changes in shape and strength of spectral lines could occur, depending on where they are formed in the disk, especially if portions of the disk or central star become obscured along the observers line of sight due to warping or tilting of the disk. The truncation of the outer disk suggest a reduction in infra-red excess, although the increase in density in the inner part could cause an increase of emission in the infra-red. Furthermore, the warping of the disk will expose outer materials to a larger amount of radiation which could lead to an increase in emission line. We therefore plan to add an radiative transfer code to our analysis in order to compute observables directly from our simulations. We also plan to extend this work to investigate the effects on the disk for non-circular binary systems.

References

Bate, M. (1995). PhD thesis. PhD thesis, Univ. Cambridge, (1995).

Benz, W. (1990). *Numerical Modelling of Nonlinear Stellar Pulsations Problems and Prospects*. Ed. by J. R. Buchler, p. 269.

Benz, W., Cameron, A. G. W., Press, W. H., et al. (1990). ApJ 348, pp. 647–667. DOI: 10.1086/168273.

Carciofi, A. C. and Bjorkman, J. E. (2006). ApJ 639, pp. 1081–1094. DOI: 10.1086/499483.
– (2008). ApJ 684, pp. 1374–1383. DOI: 10.1086/589875.
Fu, W., Lubow, S. H., and Martin, R. G. (2015). ApJ 807, 75, p. 75. DOI: 10.1088/0004-637X/807/1/75.
Harmanec, P. (1988). *Bulletin of the Astronomical Institutes of Czechoslovakia* 39, pp. 329–345.
Haubois, X., Carciofi, A. C., Rivinius, T., et al. (2012). ApJ 756, 156, p. 156. DOI: 10.1088/0004-637X/756/2/156.
Hirata, R. (2007). *Active OB-Stars: Laboratories for Stellare and Circumstellar Physics*. Ed. by A. T. Okazaki, S. P. Owocki, and S. Stefl. Vol. 361. Astronomical Society of the Pacific Conference Series, p. 267.
Kee, N. D., Owocki, S., and Sundqvist, J. O. (2016). MNRAS 458, pp. 2323–2335. DOI: 10.1093/mnras/stw471.
Lee, U., Osaki, Y., and Saio, H. (1991). MNRAS 250, pp. 432–437.
Lubow, S. H., Martin, R. G., and Nixon, C. (2015). ApJ 800, 96, p. 96. DOI: 10.1088/0004-637X/800/2/96.
Martin, R. G., Pringle, J. E., Tout, C. A., et al. (2011). MNRAS 416, pp. 2827–2839. DOI: 10.1111/j.1365-2966.2011.19231.x.
Martin, R. G., Nixon, C., Lubow, S. H., et al. (2014). ApJ 792, L33, p. L33. DOI: 10.1088/2041-8205/792/2/L33.
Millar, C. E. and Marlborough, J. M. (1998). ApJ 494, p. 715. DOI: 10.1086/305229.
Nemravová, J., Harmanec, P., Kubát, J., et al. (2010). A&A 516, A80, A80. DOI: 10.1051/0004-6361/200913885.
Okazaki, A. T. (2007). *Active OB-Stars: Laboratories for Stellare and Circumstellar Physics*. Ed. by A. T. Okazaki, S. P. Owocki, and S. Stefl. Vol. 361. Astronomical Society of the Pacific Conference Series, p. 230.
– (2012). *Circumstellar Dynamics at High Resolution*. Ed. by A. C. Carciofi and T. Rivinius. Vol. 464. Astronomical Society of the Pacific Conference Series, p. 177.

Okazaki, A. T., Bate, M. R., Ogilvie, G. I., et al. (2002). MNRAS 337, pp. 967–980. DOI: 10.1046/j.1365-8711.2002.05960.x.

Panoglou, D., Carciofi, A. C., Vieira, R. G., et al. (2016). MNRAS 461, pp. 2616–2629. DOI: 10.1093/mnras/stw1508.

Pringle, J. E. (1981). ARA&A 19, pp. 137–162. DOI: 10.1146/annurev.aa.19.090181.001033.

Reig, P., Fabregat, J., and Coe, M. J. (1997). A&A 322, pp. 193–196.

Rivinius, T., Carciofi, A. C., and Martayan, C. (2013). A&A Rev. 21, 69, p. 69. DOI: 10.1007/s00159-013-0069-0.

Secchi, A. (1867). *Astronomische Nachrichten* 68, p. 63.

Shakura, N. I. and Sunyaev, R. A. (1973). A&A 24, pp. 337–355.

4

Spiral Arms in Be Binary Systems

4.1 Introduction

The formal definition of a Be star, developed in its current form by Collins (1987), is "A non- supergiant B star whose spectrum has, or had at some time, one or more Balmer lines in emission." Other important properties of these stars include, for example, infrared and radio excess, as well as intrinsic linear polarization due to scattering processes within the disk.

From the formal definition it is clear that variability is an inherent property of these stars. The observed variability occurs on a variety of time scales from short term spectral variations on periods of seconds to hours, thought to be due to stellar pulsations, to periods of time scales on order of decades associated with the complete loss or renewal of the disk.

Intermediate periods of order of years are associated with the variations in the ratio of the violet to red peaks (V/R ratios) of doubly peaked emission lines. It has long been suggested that the origin of the V/R variations is due to rotating density enhancements within the disk. Given that V/R variations occur in approximately 2/3 of Be stars, dynamic models that follow disk structure with

time will have to be able to account for these features. However, the detailed structure of these rotating enhancements have not been thoroughly investigated and this is the motivation for this study.

Historically, Struve (1931) proposed an elegant, axisymmetric disk model that explained the formation of the disk by ejected stellar material due to rapid rotation of the central star with the variety in shape of spectral lines explained by viewing angle. However, observations of these V/R variations revealed that this model was too simplistic. In an early paper by Hirata et al. (1984), it states that researchers in this field believed that the variations were due to some sort of pulsation or precession of an elongated envelope. Kato (1983) was first to suggest the development of a one armed spiral structure as the source of the V/R variation in Be star disks. One can imagine that if the portion of the disk where there is a density enhancement is moving toward the observers line of sight that an increase in the violet side of the line may be observed and vice versa. Later, Okazaki (1991) studied long term V/R variations due to global one armed oscillations within the disk. Okazaki (1991) concludes by suggesting that detailed line profile variations analyses will be required to constrain models in order to understand the V/R variations. See section 5.3.2 in the review paper by Rivinius et al. (2013) for more details of their model as well as a summary of the observed characteristics of V/R variations are presented.

In our case, however, the analysis is more complicated. Sana et al. (2012) reports that 75% of massive stars with masses, $M > 8\ M_\circ$ are binaries or were part of a binary system at some time. This means that many, if not all, Be stars could be members of a binary system. In binary systems, tidal interactions, radiative interactions and in the case of Be/Xray systems high energy interactions, must all be taken into account. Not only do tidal interactions truncate the disk but a build-up of density at radial distances less than the truncation radius, called the watershed effect, is predicted (Cyr et al., 2016; Okazaki et al., 2002; Panoglou et al., 2016).

Okazaki et al. (2002) studied the effects on coplanar decretion disks and neutron stars in Be/Xray binaries and found that in binary systems a pattern of double spiral arms is set up which may indeed become phase-locked with the

companion. It is not completely clear how having two rotating arms would affect the shape and variation of doubly peaked emission lines. For example, if one arm of the spiral was bigger and/or denser, it may contribute more significantly to the line profile. Although, the Be/Xray systems have been increasingly well studied, the literature reveals much fewer detailed studies on normal Be star binary systems and a thorough investigation is long over-due.

The recent periastron passage of an early type Be star, δ Sco, in an eccentric binary system in 2011 provided an opportunity to study the effects on the disk during the passage. Che et al. (2012) studied this system with interferometry. Their work revealed apparent asymmetries in the inner disk, but due to limited resolution they were not able to conclusively determine any pattern. The same system was monitored with polarization observations by Bednarski et al. (2012) and they claim that there are significant changes occurring in the surface density of the disk during the passage. It is clear that detailed models that can follow disk density with time will be required to interpret observations.

In this work, we investigate the size and shape of these density structures for a Be binary system. We also examine how these features change with variations in viscosity, orbital phase, and misalignment angle. This work is organized as follows; details about our simulations are provided in Section 4.2. Our results are presented in Section 4.3 and a summary and discussion can be found in Section 4.4.

4.2 Methodology

The same simulations described in Chapter 3 were used in this work in order to study the structure of the spiral arms. Similar to the previous chapter, we investigated the effects of three parameters have on the structure of the arms; the viscosity of the disk ($\alpha_{\rm SS}$ = 0.1, 0.5, 1.0) the misalignment angle ($\theta = 0°$, 30°, 45°, 60°), and the orbital phase (p = 0.25, 0.50, 0.75, 1.00). Here we define p = 0.00 and 1.00 to be the the beginning of 49^{th} and 50^{th} orbital period (P_{orb}), respectively (see Figure 3.1 for more details). Stellar and orbital parameters of our simulated systems can be found in Table 3.1. Note that we restricted our

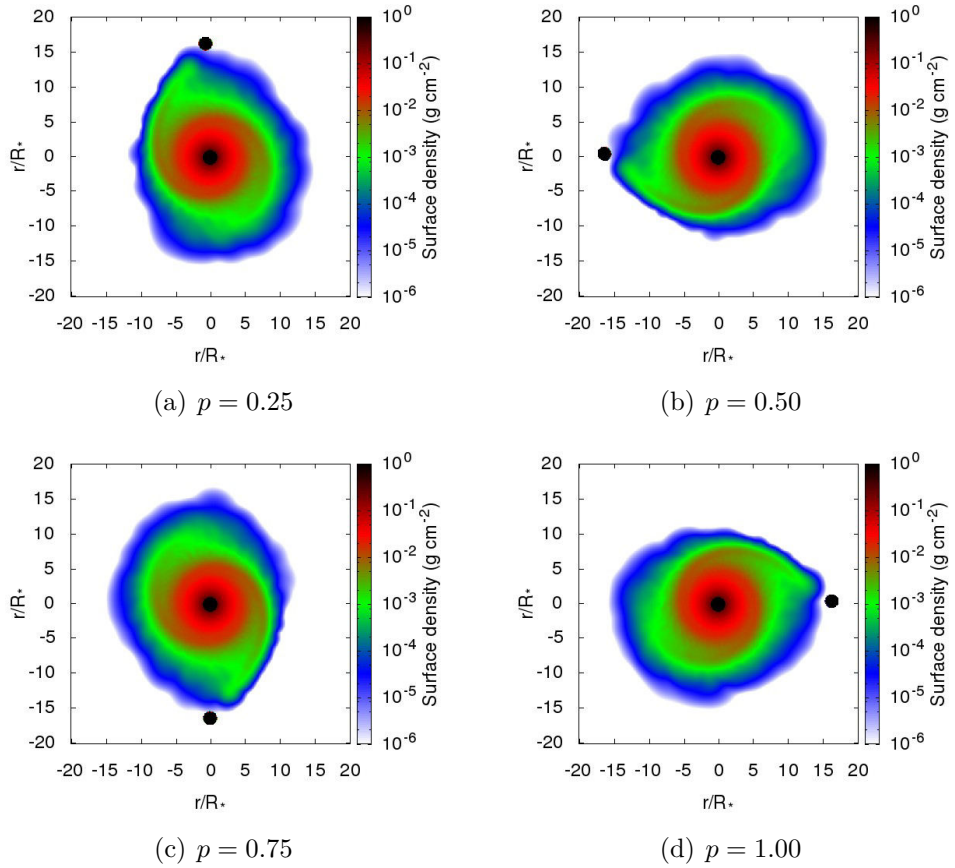

(a) $p = 0.25$ (b) $p = 0.50$

(c) $p = 0.75$ (d) $p = 1.00$

Figure 4.1: Map of the surface density, $\Sigma(r, \phi)$, of an aligned disk ($\theta = 0°$) at orbital phases of (a) $p = 0.25$, (b) $p = 0.50$, (c) $p = 0.75$, and (d) $p = 1.00$. Viscosity is set to $\alpha_{\rm SS} = 0.5$.

study to simulations with an orbital period of 30 days, corresponding to a semi-major axis of 59.9 $R_\odot$.

4.3 Results

Figure 4.1 shows a top-down view of the surface density, $\Sigma(r, \phi)$, for one of our simulations ($\alpha_{\rm SS} = 0.5$, $\theta = 0°$) seen at various orbital phases ($p = 0.25$, 0.5, 0.75, and 1.0). The primary and secondary stars are represented by the black circles.

In order to better study these density enhancements, we investigated the sur-

face density, $\Sigma_r(\phi)$, as a function of the azimuthal angle ϕ at different radial distances r. The azimuthal position (ϕ_o), maximum surface density enhancements ($\Delta\Sigma$), and width (σ) of these density enhancements are described using a series of Gaussian functions;

$$\Sigma_r(\phi) = \Delta\Sigma e^{-(\phi-\phi_o)^2/\sigma^2} + \Sigma_o, \tag{4.1}$$

where Σ_o is the base surface density of the disk at r. Note that $\Delta\Sigma$ denotes the difference in surface density between the arm and base of the disk (Σ_o). The surface density of the arms can be written as:

$$\Sigma_{arm} = \Sigma_o + \Delta\Sigma. \tag{4.2}$$

Figure 4.2 shows the azimuthal position, ϕ_o, of the leading (a) and trailing (b) arms as a function of radial distance obtained from Equation 4.1 (solid lines). We notice that, as the phase of the orbit increases, the azimuthal position of each arm shifts by 90°, which is expected since the motion of the arms is locked with the motion of the secondary. We also notice a shift of approximately 180° between leading and trailing arms, which is also expected since the arms are roughly on opposite sides of the primary.

Through experimentation we found that the shape of these spiral (solid lines) are best fitted an exponential function (dashed lines),

$$\phi(r) = Ae^{-\gamma r} + B, \tag{4.3}$$

where A and B are fitting constants, and γ is a parameter related to the winding of the spiral arms. Smaller values of γ indicate tighter winding of the spiral arm. The values of these parameters for each model are shown in Tables 4.1 and 4.2.

Figure 4.3 shows the values of γ for all 96 models as a function of orbital phase. In panel a), data points are colour coded according to whether they came from a leading arm (red) or a trailing arm (blue), while in panel b) they are colour coded based on their misalignment angle; 0° (red), 30° (orange), 45°

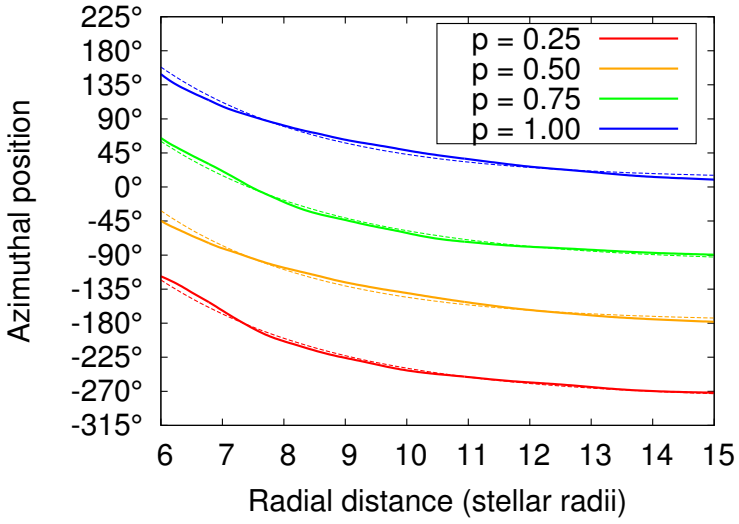

(a) Leading arm

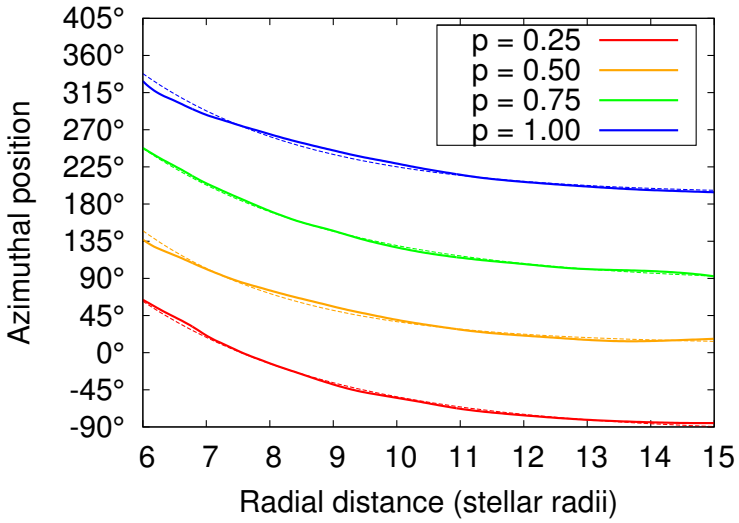

(b) Trailing arm

Figure 4.2: Azimuthal position of the leading (a) and trailing (b) spiral arm as a function of radial distance, at orbital phases of $p = 0.25$ (red), 0.50 (orange), 0.75 (green), and 1.00 (blue). Results obtained from our simulations are shown as solid lines while the results of the exponential fit, described in Equation 4.4, are represented by the dashed lines.

Table 4.1: Winding parameter γ of the leading arms.

Viscosity parameter [α_{SS}]	Misalignmen angle [θ]	Orbital phase [p] 0.25	0.50	0.75	1.0
0.1	0°	0.493176	0.494111	0.486924	0.488959
	30°	0.426395	0.469424	0.44951	0.465335
	45°	0.377009	0.448331	0.370139	0.443064
	60°	0.336403	0.415079	0.351661	0.413257
0.5	0°	0.400298	0.385405	0.38784	0.378331
	30°	0.334257	0.37655	0.329885	0.377847
	45°	0.294021	0.370111	0.278089	0.362351
	60°	0.28077	0.366964	0.281018	0.356908
1.0	0°	0.339782	0.341447	0.368328	0.392726
	30°	0.318748	0.360155	0.269648	0.327735
	45°	0.270067	0.361914	0.268502	0.273992
	60°	0.248668	0.318104	0.239352	0.332447

Table 4.2: Winding parameter γ of the trailing arms.

Viscosity parameter [α_{SS}]	Misalignmen angle [θ]	Orbital phase [p] 0.25	0.50	0.75	1.0
0.1	0°	0.502666	0.456249	0.439399	0.449011
	30°	0.389446	0.504825	0.403125	0.48496
	45°	0.390895	0.405715	0.388981	0.432895
	60°	0.342426	0.387705	0.334303	0.382575
0.5	0°	0.390918	0.366363	0.354666	0.387224
	30°	0.316252	0.401846	0.314714	0.366311
	45°	0.283082	0.35842	0.268752	0.384042
	60°	0.285157	0.300244	0.27752	0.295789
1.0	0°	0.441609	0.342035	0.358378	0.350046
	30°	0.307852	0.293523	0.28033	0.326302
	45°	0.252613	0.314685	0.272222	0.323129
	60°	0.280809	0.225935	0.280771	0.275237

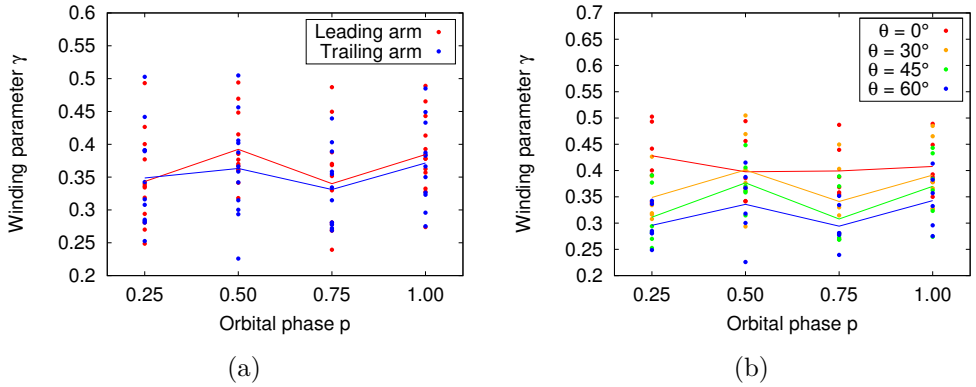

Figure 4.3: Winding parameter, γ, of spiral arms as a function of orbital phase p. In panel (a), values are grouped into leading arms (red) and trailing arms (blue) while panel (b) the values are grouped by misalignment angle, 0° (red), 30° (orange), 45° (green), and 60° (blue). The average of each of these groups as a function of p is represented by the solid lines.

(green), and 60° (blue). In both panels the solid lines show the variation of the average value of each grouping with orbital phase.

Figure 4.4 shows the same γ values plotted as a function of the viscosity parameter $\alpha_{\rm SS}$. For this Figure, the data points were divided based on their misalignment angle in the same way as in Figure 4.3b. Again the solid lines show the average values of each set of misalignment angles.

Figure 4.5 is similar to Figures 4.3 and 4.4 but with γ plotted as a function of misalignment angle with different colours representing different $\alpha_{\rm SS}$ values; 0.1 (red), 0.5 (green) and 1.0 (blue).

In Figure 4.3, we notice that the spread of γ values is nearly the same for all four orbital phases, which suggests that the orbital phase plays a minor role in the winding of the disk. However small variations can be seen in the average γ values (solid lines). In panel a) we see that the winding of both arms are very similar, with trailing arms being slightly more wound compared to the leading arms. Interestingly, panel (b) shows that these small variations seen in panel (a) originate mainly from misaligned systems ($\theta = 30°$, 45°, and 60°), while the aligned systems show almost no dependence on p. Furthermore, these variations seem to oscillate, having smaller γ values (more tightly wound arms) at $p =$

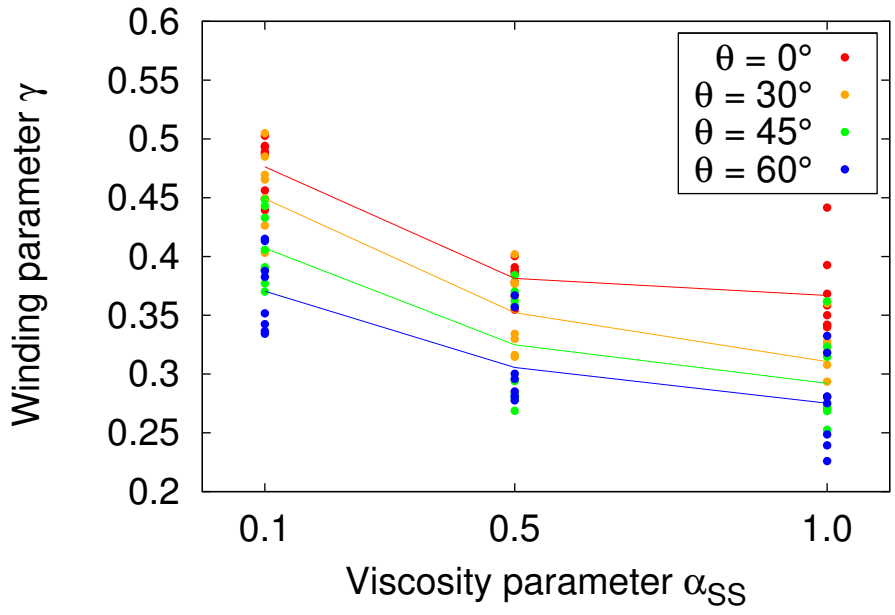

Figure 4.4: Same as Figure 4.3(b) except plotted as a function of disk viscosity $\alpha_{\rm SS}$.

0.25 and 0.75 than at $p = 0.50$ and 1.00. These features all point toward the fact that the degree of elevation of the secondary above or below to the equatorial plane has an impact on the winding of the disk.

Figure 4.4 shows that the winding of the arms has a clear dependence on the viscosity of the disk, with smaller values of γ for larger $\alpha_{\rm SS}$, i.e. the more viscous the disk, the tighter the spiral arms. This holds true for all four misalignment angles. Finally, we notice that the winding of the arms is also dependent on the misalignment angle, with larger θ resulting in more tightly wound arms (lower γ). Both of these dependences can also be seen in Figure 4.5. Interestingly, we see that the dependence on $\alpha_{\rm SS}$ does not appear to be linear. In contrast, we see a much more linear dependence with θ.

$$\phi(r) = Ae^{-Br)} + C, \tag{4.4}$$

where B is related to the winding of the disc. Equation 4.1 allows us to study

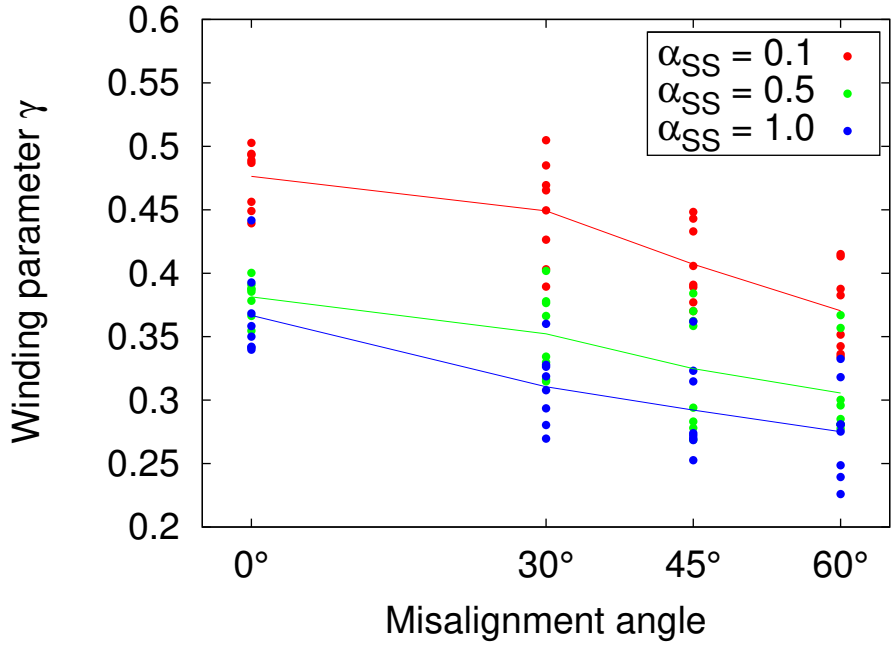

Figure 4.5: Same as Figures 4.3 and 4.4 except values are plotted as a function of the misalignment angle θ. The colours represent different disk viscosity values; $\alpha_{\rm SS} = 0.1$ (red), 0.5 (green) and 1.0 (blue).

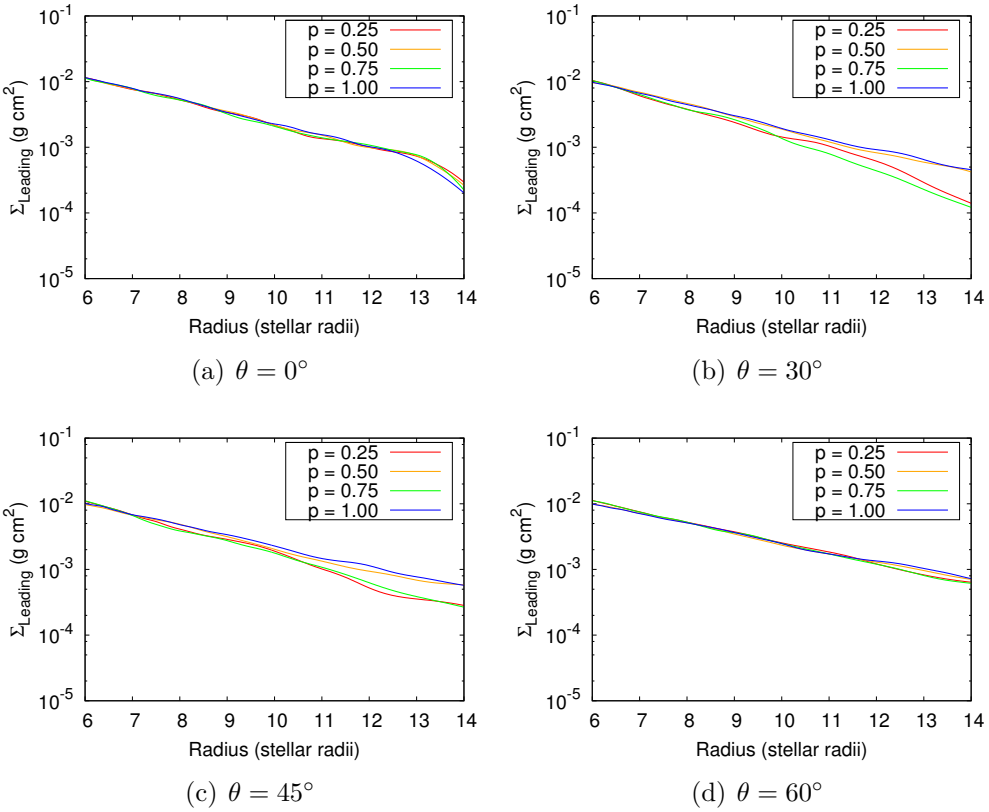

(a) $\theta = 0°$ (b) $\theta = 30°$

(c) $\theta = 45°$ (d) $\theta = 60°$

Figure 4.6: Comparison of the surface density of the leading arms as a function of radial distance, r, at different orbital phases; $p = 0.25$ (red), 0.50 (orange), 0.75 (green), and 1.00 (blue). From top to bottom, the panels show the results for misalignment angles of $\theta = 0°$, 30°, 45°, and 60°, respectively. The viscosity of all models presented is $\alpha_{\rm SS} = 0.5$.

the density of the spiral arms in detail. Figures 4.6 and 4.7 compare the surface density, Σ_{arm}, value of the leading and trailing arms, respectively as a function of r at different phases of the binary orbit, $p = 0.25$ (red), $p = 0.50$ (orange), $p = 0.75$ (green), $p = 1.00$ (blue), for $\alpha_{\rm SS} = 0.5$. Each panel corresponds to a different misalignment angles.

We see the that phase has very little effect on surface density of the leading arm in both the $\theta = 0°$ (aligned) and $\theta = 60°$ systems. However, we do see variation in the outer disk of the $\theta = 30°$ and $\theta = 45°$ systems. In both instances the surface density of the arm is greater at phases of $p = 0.5$ and 1.0. In all four

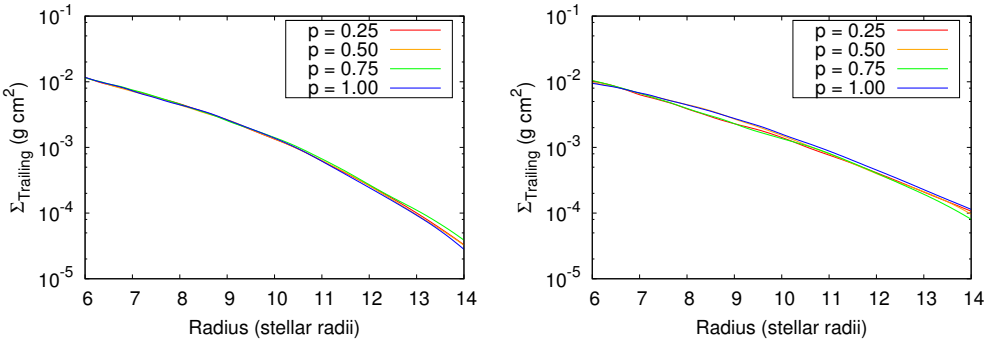

(a) $\theta = 0°$ (b) $\theta = 30°$

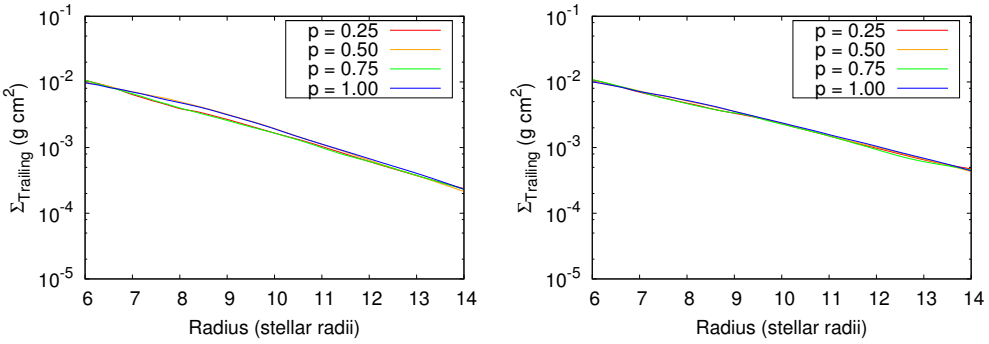

(c) $\theta = 45°$ (d) $\theta = 60°$

Figure 4.7: Same as Figure 4.6 for the trailing arms.

cases, the surface density of the trailing arm is independent of phase.

Similarly to Figures 4.6 and 4.7, Figures 4.8 and 4.9 show a comparison of the surface density of each arm for all three viscosity parameters, $\alpha_{\rm SS} = 0.1$ (red), $\alpha_{\rm SS} = 0.5$ (green), and $\alpha_{\rm SS} = 1.0$ (blue). As Bjorkman et al. (2005) have shown, the surface density of the disk is expected to scale with $\alpha_{\rm SS}^{-1}$, therefore we multiplied each profile by $\alpha_{\rm SS}$ in order to have a proper comparison. As in the previous Figures, each row represents a different misalignment angle. All Figures are at a phase of $p = 1.00$ (or 50 P_{orb}). Here we see that viscosity has a visible effect on the fall-off rate of the surface density profiles, showing a steeper drop in density for smaller $\alpha_{\rm SS}$ values. Additionally we see that trailing arms have a steeper fall-off rate than leading arms.

Figure 4.10 compares the surface density variations of each arm for all four misalignment angles, $\theta = 0°$ (red), 30° (orange), 45° (green), and 60° (blue), in a similar fashion as Figures 4.6-4.9. This time, the rows, from top to bottom, represent viscosity parameters of $\alpha_{\rm SS} = 0.1$, 0.5, and 1.0, respectively. Once again, the phase in all six panels is $p = 1.00$. Here we see that variations are very small close to the star but increase with radial distance where the surface density of the arms becomes greater with misalignment angle. We notice that the point of divergence (where the curves starts diverging) increases with the angle of misalignment. We also notice that the location of the divergence of the trailing arms are always closer to the star than for the leading arm.

4.4 Discussion and Conclusion

The density structure and geometry of the spiral arms formed inside a Be-binary system were studied in detail for the first time. Using the results of the simulations used in Chapter 3, we examined the azimuthal dependence of the surface densities of the disk for multiple radial distances. Gaussian functions were used to fit these surface density profiles in order to extract the azimuthal location and surface densities of both arms.

We investigated the effects of orbital phase, p, disk viscosity, $\alpha_{\rm SS}$, and the misalignment angle, θ, on the winding parameter, γ, of the spiral arms. We find

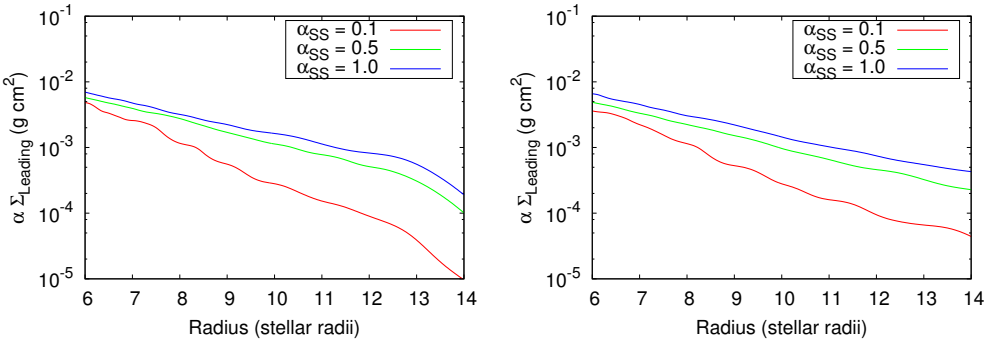

(a) $\theta = 0°$ (b) $\theta = 30°$

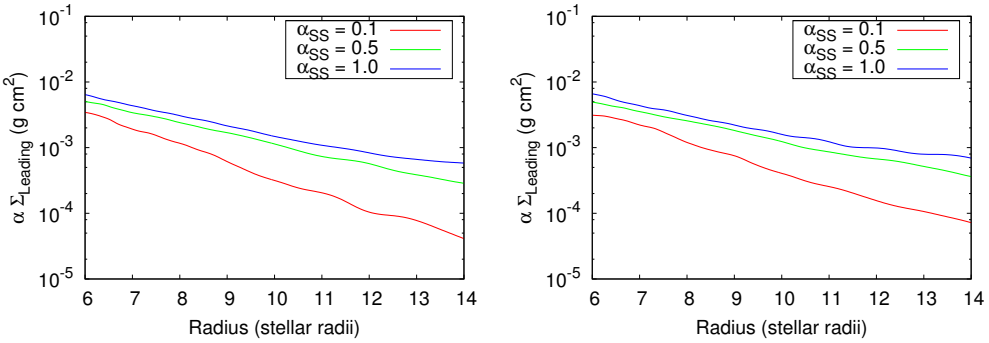

(c) $\theta = 45°$ (d) $\theta = 60°$

Figure 4.8: Same as Figure 4.6 for different viscosity values; $\alpha_{\rm SS} = 0.1$ (red), 0.5 (green), and 1.0 (blue). The orbital phase of all models presented is $p = 1.00$.

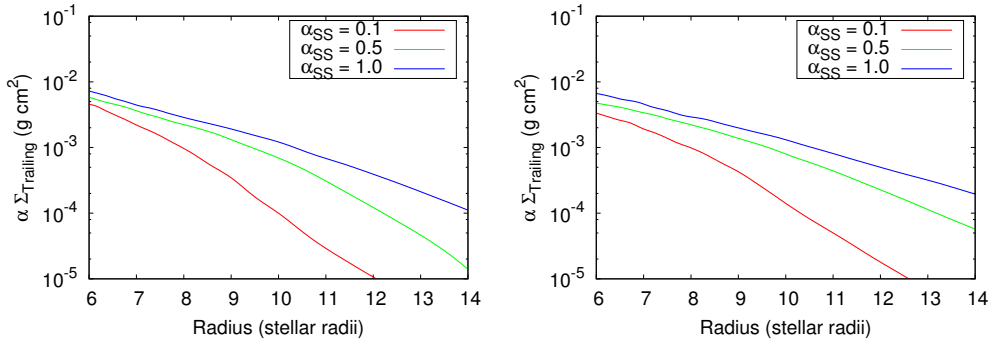

(a) $\theta = 0°$ (b) $\theta = 30°$

(c) $\theta = 45°$ (d) $\theta = 60°$

Figure 4.9: Same as Figure 4.7 for different viscosity values; $\alpha_{\rm SS} = 0.1$ (red), 0.5 (green), and 1.0 (blue). The orbital phase of all models presented is $p = 1.00$.

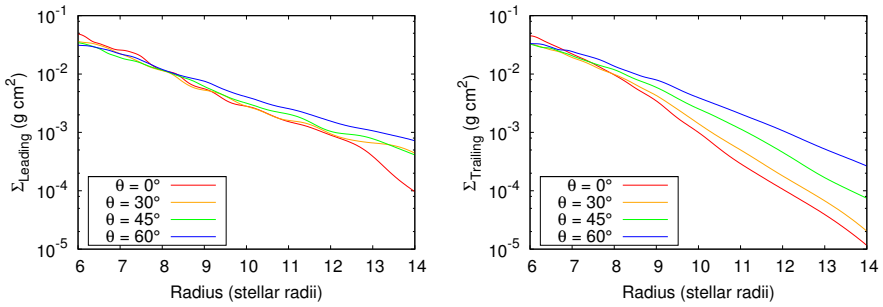

(a) $\alpha_{\rm SS} = 0.1$, leading-arm (b) $\alpha_{\rm SS} = 0.1$, trailing-arm

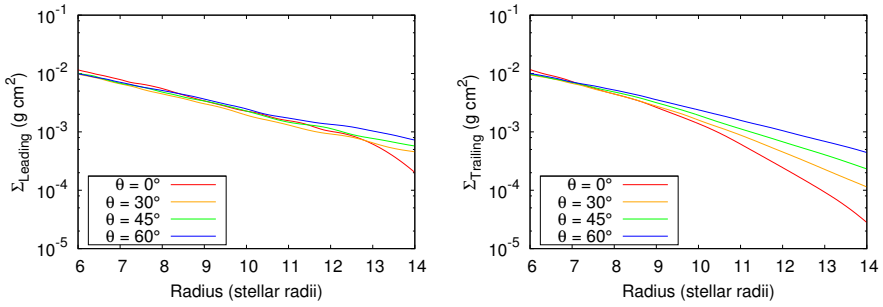

(c) $\alpha_{\rm SS} = 0.5$, leading-arm (d) $\alpha_{\rm SS} = 0.5$, trailing-arm

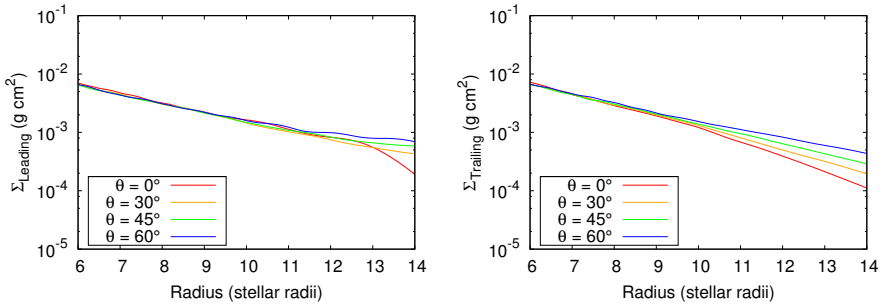

(e) $\alpha_{\rm SS} = 1.0$, leading-arm (f) $\alpha_{\rm SS} = 1.0$, trailing-arm

Figure 4.10: Comparison of the surface density of the leading (left panels) and trailing arms (right panels) as a function of radial distance, r, for different misalignment angles; $\theta = 0°$ (red), 30° (orange), 45° (green), and 60° (blue). From top to bottom, the panels show the results for viscosity values of $\alpha_{\rm SS} = 0.1$, 0.5, and 1.0, respectively. The orbital phase of all models presented is $p = 1.00$.

that γ has only a small dependence on p, which is only present in misaligned systems. This is a good indication that the location of the secondary above and below the disk in misaligned systems can also affect the structure of the spiral arms. We also find an inverse relationship between γ and the $\alpha_{\rm SS}$ and θ parameters, i.e., an increase in either the viscosity of the disk or the misalignment angle of the orbit will result in more tightly wound spiral arms.

We also investigated how the surface density of the arms is affected by phase, viscosity, and misalignment angle. We find that the trailing arm has little to no dependence on the orbital phase of the binary. Slight differences in the outer parts of the arms were seen for misalignment angles of $\theta = 30°$ and $45°$ which can be attributed to the elevations of the secondary above or below the equatorial plain. The viscosity of the disk is found to affect the density structure of the arms, more specifically the surface density fall-off rate, which is found to be steeper for smaller $\alpha_{\rm SS}$ values. Finally, we find that the misalignment of the orbit affects mostly the outer parts of the spiral arms, where the arms become denser with increasing θ. The radial distances at which these effects starts to appear increases with viscosity. This distance is also consistently closer to the primary for trailing arms compared to the leading arms.

Understanding the behaviour of these spiral arms is crucial to make sense of observations and to have a better grasp of the formation, evolution, and dissipation of Be star disks in both isolated and binary systems.

The spiral arms in the inner disk region should be indirectly observable in both the shape and variability in the spectral lines. As well, with further improvement in observational technologies, such as interferometry, with increasing resolution we will soon be able to resolve details in the variation of disk density. This would mean that the spiral arms could be directly resolved and compared with predictions. An other possible example is the presence of triple-peaked emission lines observed in the spectra of some Be stars. One such star, γ Cas, is a well-studied early-type Be binary system that undergoes V/R variations and has been observed to display triply peaked H$\alpha_{\rm SS}$ profiles. Nemravová et al. (2012) suggest that changes within the density and extent of the disk may be responsible for these observed variations. Escolano et al. (2015) also noted the

presences of triple-peaked emission phases in the Be star ζ Tau. They speculate that these features occur within the outermost portions of the Hα_{SS} emitting region of the disk and may be due to the presence of a binary companion.

In future works, we plan to investigate the evolution of these arms with time during the disk building phase. We also plan to use non-LTE radiative transfer codes in order to directly compute observables expected from such systems, and therefore bring more insight to the study of Be star disk.

References

Bednarski, D. and Carciofi, A. C. (2012). *Circumstellar Dynamics at High Resolution*. Ed. by A. C. Carciofi and T. Rivinius. Vol. 464. Astronomical Society of the Pacific Conference Series, p. 239.

Bjorkman, J. E. and Carciofi, A. C. (2005). *The Nature and Evolution of Disks Around Hot Stars*. Ed. by R. Ignace and K. G. Gayley. Vol. 337. Astronomical Society of the Pacific Conference Series, p. 75.

Che, X., Monnier, J. D., Tycner, C., et al. (2012). ApJ 757, 29, p. 29. DOI: 10.1088/0004-637X/757/1/29.

Collins II, G. W. (1987). *IAU Colloq. 92: Physics of Be Stars*. Ed. by A. Slettebak and T. P. Snow, pp. 3–19.

Cyr, I. H., Jones, C. E., Panoglou, D., et al. (2016). MNRAS.

Escolano, C., Carciofi, A. C., Okazaki, A. T., et al. (2015). A&A 576, A112, A112. DOI: 10.1051/0004-6361/201425446.

Hirata, R. and Kogure, T. (1984). *Bulletin of the Astronomical Society of India* 12, pp. 109–151.

Kato, S. (1983). PASJ 35, pp. 249–261.

Nemravová, J., Harmanec, P., Koubský, P., et al. (2012). A&A 537, A59, A59. DOI: 10.1051/0004-6361/201117922.

Okazaki, A. T. (1991). PASJ 43, pp. 75–94.

Okazaki, A. T., Bate, M. R., Ogilvie, G. I., et al. (2002). MNRAS 337, pp. 967–980. DOI: 10.1046/j.1365-8711.2002.05960.x.

Panoglou, D., Carciofi, A. C., Vieira, R. G., et al. (2016). MNRAS 461, pp. 2616–2629. DOI: 10.1093/mnras/stw1508.

Rivinius, T., Carciofi, A. C., and Martayan, C. (2013). A&A Rev. 21, 69, p. 69. DOI: 10.1007/s00159-013-0069-0.

Sana, H., de Mink, S. E., de Koter, A., et al. (2012). *Science* 337, p. 444. DOI: 10.1126/science.1223344.

Struve, O. (1931). ApJ 73, p. 94. DOI: 10.1086/143298.

5
Conclusion

In Chapter 2, we developed a novel approach to infer the geometry of Be star disks using interferometric measurements of axis ratio collected from the literature. Using Monte Carlo techniques and Bayesian statistics, these measurements were compared with axis ratios calculated using two different disk models; a wedge model, similar to the one proposed by Waters (1986), and an equidensity model, based on the viscous disk model. Axis ratio measurements were divided into two groups; the first includes all measurements in the K-, H- or N-band (KHN-band) while the second group includes measurements near or at the Hα emission line. The opening angles and extent of the emitting regions were found to be systematically smaller for the KHN-band emission region than the Hα region, which agrees with the findings of Gies et al. (2007) and Carciofi (2011), as well of the predictions of the viscous disk model (Bjorkman, 1997). We find values of opening half-angles ranging from 0.15° to 3.0° for the KHN-band emitting regions and from 3.7° to 14° for the Hα emitting region, in agreement with values reported by Porter (1996), Wood et al. (1997), and Hanuschik et al. (1996) of 2.5°, 5°, and 13°, receptively. The emitting regions for the KHN-band are found to be within 2 to 4 stellar radii and within 80 to 95 stellar radii for the Hα region. These values are consistent with the overall results predicted by the

viscous decretion theory, see figure 1 of Carciofi (2011).

In Chapter 3, we study the structure and evolution of Be star disks formed within misaligned binary systems using numerical simulations generated from a smoothed particle hydrodynamics (SPH) code. We examined the effects of three parameters, the viscosity of the disk, the degree of misalignment between the plane of the orbit and the plane of the stellar equator, and the distance between the primary and secondary stars, on the overall structure of the disk. In this study, we first investigate the azimuthally averaged surface density of the disk. As previously reported, we find that the presence of the secondary causes the disk to truncate, resulting in shallower surface density profiles (denser disks) in the inner regions (before the truncation radius) and a much steeper fall-off rate in the outer parts of the disk (after the truncation radius). The steepness of density fall-off rates of the inner disk and the radial position of the truncation were both found to increase with viscosity, misalignment angle, and separation distance, while the opposite trend was found for the outer region, where the fall-off rates are steeper for systems with less viscous disks, smaller misalignment angles, and closer companions. The disk was also found to be more warped for mid-range misalignment angles and viscosity, suggesting that a more complex relationship exists between these parameters and the warping of the disk. Finally, the scale heights of our disks were compared with theoretical values expected for isolated Be stars. We find that the two are in good agreement in the inner-most parts of the disk but differ in the outer parts, especially in regions where density enhancements are present. This is expected since these enhancements are produced by perturbations that affect the vertical hydrostatic equilibrium of the disk.

In Chapter 4, we expand on the work in Chapter 3 by studying the detailed structure of density enhancements, or spiral arms, and how these structures are affected by changes in viscosity, misalignment angle, and orbital phase. We find that the spiral arms are more tightly wound in systems with larger viscosity and greater degrees of misalignment. A dependence on spiral structure with orbital phase was found only in misaligned systems which suggests that the winding is also influenced by the elevation of the secondary. Similarly, the surface density

profiles of the leading arms were also found to vary with phase in misaligned systems in the outer part of the disk, while no variations with phase were observed in the trailing arms. Overall, the density of the spiral arms were found to increase with viscosity, while density fall-off rates decreased with increasing viscosity.

The results presented in this work bring new insights about the Be star phenomena. We have developed a novel technique to study the geometry of Be star disks and have done unique research into their dynamics and structure, such as opening angle, extent of the disk, density structure and have also followed changes in the disk with time using our SPH simulations.

The knowledge gained from studying Be stars and their disks may have far reaching benefits for this field of study as well as for other research areas in astrophysics. Research into the structure in dynamics of the disk can bring new insights to better understand other disk phenomena, such as accretion disks around black holes, Herbig Ae/Be star, Algol systems, and protoplanetary systems. Studying the effects of a close binary companion on the disk could potentially help us help us to develop new and better techniques to detect binary systems whose secondary cannot be detected by traditional means. Be disk systems can also help us understand the interplay between stellar evolution and stellar rotation. For massive stars, this interplay is still not well understood and these systems offer a unique laboratory for study. In future work, we plan to combine the hydrodynamical solving properties of the SPH code with the observational prediction capability of a non-LTE radiative transfer codes, such as HDUST, which will allow us to make predictions about our models that can be compared to observables, such as spectral lines, polarization signature, and interferometric measurements. This new work, tightly constrained by observations, will provide testable dynamic models with unprecedented realism which will drastically increase our understanding of these systems.

References

Bjorkman, J. E. (1997). *Stellar Atmospheres: Theory and Observations*. Ed. by J. P. De Greve, R. Blomme, and H. Hensberge. Vol. 497. Lecture Notes in Physics, Berlin Springer Verlag, p. 239. DOI: 10.1007/BFb0113487.

Carciofi, A. C. (2011). *IAU Symposium*. Ed. by C. Neiner, G. Wade, G. Meynet, et al. Vol. 272. IAU Symposium, pp. 325–336. DOI: 10.1017/S1743921311010738.

Gies, D. R., Bagnuolo Jr., W. G., Baines, E. K., et al. (2007). ApJ 654, pp. 527–543. DOI: 10.1086/509144.

Hanuschik, R. W., Hummel, W., Sutorius, E., et al. (1996). A&AS 116, pp. 309–358.

Porter, J. M. (1996). MNRAS 280, pp. L31–L35.

Waters, L. B. F. M. (1986). A&A 162, pp. 121–139.

Wood, K., Bjorkman, K. S., and Bjorkman, J. E. (1997). ApJ 477, p. 926. DOI: 10.1086/303747.

Isabelle Hélène Cyr – Résumé

Research Interests

Be stars, circumstellar disks, hydrodynamical modeling,

Education

2011-2016 PhD in Astrophysics - Western University, London, ON

Supervisor: Carol E. Jones, Ph.D
Expected: Fall 2016

2006-2011 M.S., Physics - Universite de Moncton, Moncton, NB

Supervisor: Normand Beaudoin, Ph.D and Serge Gauvin, Ph.D
Topic: *Investigation de la Deformation Spectrale d'un Appareil Optique a Irradiation Polychromatique*

Employment History

Sep 2014-Present Physics and Astronomy Department,Western University, London, ON
Lead TA - Phys 1301A/1401A & Phys 1302B/1402B

Duties included:

- Supervising TAs
- Double checking quizzes and exams
- Organizing tutorials
- Proctoring and marking exams
- Entering marks

Sept 2011-April 2014 Physics and Astronomy Department,Western University, London, ON
Teaching assistant

Duties included:

- Running tutorials
- Running labs
- Marking assignment, quizzes, and exams
- Answering student questions online
- Proctoring exams

Refereed Journal Publications

1. Cyr, I. H., Jones, C. E., Panoglou, D., Carciofi A. C. 2016 (*In progress.*)

2. Cyr, I. H., Jones, C. E., Panoglou, D., Carciofi A. C., Okazaki A. T. 2016 (*submitted second version with referee's comments addressed.*)

3. Panoglou, D., Carciofi A. C., Vieira1, R. G., Cyr, I. H., Jones, C. E., Okazaki A. T., Rivinius T. 2016, MNRAS, 337, 967

4. Cyr, R. P., Jones, C. E., Tycner, C. 2015, ApJ, 799, 33C

5. Cyr, R. P., Panoglou, D., Jones, C. E., Carciofi A. C. 2014 (*Conference proceeding, awaiting publication.*)

6. Jones, C. E., Wiegert, P. A., Tycner, C., Henry, G. W., Cyr, R. P., Halonen, R. J., Muterspaugh, M. W. 2013, AJ, 145, 142J